

POLITECNICO DI MILANO
DEPARTMENT OF AEROSPACE SCIENCE AND TECHNOLOGY
DOCTORAL PROGRAMME IN AERONAUTICAL ENGINEERING

AERO-SERVO-ELASTIC OPTIMIZATION IN CONCEPTUAL AND PRELIMINARY DESIGN

Doctoral Dissertation of:
Francesco Toffol

Supervisor:
Prof. Sergio Ricci

Tutor:
Prof. Lorenzo Dozio

The Chair of the Doctoral Program:
Prof. Pierangelo Masarati

2021 – XXXIII Cycle

Abstract

The effects of air pollution are there for all to see, aviation plays its role in this and its emission share is increasing outpacing the prediction. The expanding aviation market together with more and more challenging emission reduction plans ask for breakthrough solutions.
Composite materials and more reliable control systems open new design spaces for the investigation of new aircraft configurations exploiting the latest technology, the current design tools must adapt to consider these aspects since the conceptual design phases.
In this work a meta-model of the wingbox is developed and provides an analytical representation of the structural components, which is used to manage multiple models and analysis results. Active control's impact on the structural weight is accounted in the sizing procedure since the conceptual design phase by the implementation of an automatic controller tuning in the optimization loop. Improved models and control technologies are encompassed in an aero-servo-elastic optimization framework (NeOPT) for the conceptual design, which sizes an aircraft with aeroelastic constraints obtained with different simulation (trim, gust and flutter).
NeOPT is exploited to size a family of twin aisle long haul (TAHL) aircraft focusing on the sensitivity of the fuel burn with respect to the aspect ratio. The result is a trade-off study which shows the balance between induced drag reduction and structural penalty mass achieved by increasing the wing aspect ratio.

Acknowledgements

This work is the result of a three years journey during which I had the privilege of meeting and collaborating with fantastic people.
At first, I want to thank is my supervisor Prof. Sergio Ricci, I'm grateful for the trust he put in me, mentoring my research path and smoothing my character.
I wish to express my gratitude to Prof. Paolo Mantegazza for transmitting to everyone his enthusiastic approach to aeroservoelasticity and for sharing his encyclopedic knowledge with me. A special thanks goes to Prof. Gianluca Ghiringhelli for the help in the implementation of NeoANBA.
I would like to thank all the DAER technicians who made possible the testing of all our experimental project.
A special mention goes to Fede, who left me the burden of the active control, all kidding aside I wish to thank you for the fantastic experience shared during the years, both technical and human.
I have to thanks all the colleagues of the GVPM first floor: Dega, Dona, Luca1, Luca2, Zaga, Teo, Monta, Nicola, Vittorio: you made the workplace a wonderful environment.
Mauro, thanks for all the Italian trash shared in Arpesani 3.
I wish to thanks Mavi for her true friendship, you were there when I needed it.
Martin, life put us on different paths but you truly are my brother since the day that Buratti put us at the same desk. We do not need words to describe it just let's make a toast with some Teroldego.
I need to thanks my uncles Paola and Graziano, you taught me so much about life in these years.

I want to say thank you to my family, my parents Germano and Giovanna and my brother Giovanni, you literally gave a meaning to what being a family truly is.
Now it's time for the most classical *last but not least*: Bea, you know more than everyone what did it take to get there. It was a roller-coaster of emotion, a struggle against my uncertainty that I would never win without you by my side.
Thank you all.

Contents

1 Introduction **1**
- 1.1 Background context 1
- 1.2 Research motivation, objective and thesis structure 8

2 Wingbox description through semi-analytical model **11**
- 2.1 NeoCASS enviroment 11
- 2.2 Wingbox meta-model 16
- 2.3 Geometry module 18
- 2.4 NeoANBA 25
  - 2.4.1 NeoANBA mathematical model 26
  - 2.4.2 NeoANBA Validation 37
  - 2.4.3 Concluding remarks on the wingbox description 45

3 Active controls for load alleviation and flutter suppression **47**
- 3.1 Controller design 48
- 3.2 Gust Load Alleviation 51
  - 3.2.1 Project introduction 51
  - 3.2.2 Gust Load Alleviation strategy development and validation 53
  - 3.2.3 Numerical Results 55
  - 3.2.4 Experimental validation 62
- 3.3 Active Flutter Suppression 66
  - 3.3.1 Project overview 66
  - 3.3.2 Control Law Design 69

3.3.3 Wind tunnel test 73
3.4 Concluding remarks on active control 76

4 NeOPT: the optimization framework 79
4.1 Short introduction to the optimization in aeronautical engineering 79
4.2 Overview on NeOPT 81
4.2.1 Design variables 82
4.2.2 Aeroelastic solvers 84
4.2.3 Objective and constraints 85
4.2.4 Aerodynamics 87
4.2.5 Material and properties 88
4.2.6 Load transfer module 90
4.2.7 Procedure summary 91

5 Application of NeOPT for a trade-off study of a long haul aircraft 95
5.1 TALH family design with trim loads and flutter constraints . . 98
5.2 TALH including gust loads and GLA 108

6 Conclusions 117

Bibliography 121

CHAPTER 1

Introduction

1.1 Background context

Air transportation is a resilient and expanding market with a constant +5% increment per year (pre COVID-19 era). Despite economic-financial crises, acts of terror and epidemics, it proved to quickly recover from these events. Fig. 1.1 reports on the same plot the last 15 years seasonally adjusted RPK[1] trend, main global events and act of terrors. Despite all these adverse situations, the air traffic volume increased constantly. The only stop in this trend was the 2008 financial crisis which lasted for 2 years, but in 2010 the RPK recovered 2008 values and continued its increasing trend.

The seats demand increased constantly in the last two decades and this trend appears to be constant for the next years. In a similar way, freighter market is expanding too. To satisfy the increasing payload demand (passengers and goods), airliners are enlarging their fleets and this will increase the air traffic. The world's aircraft fleet is expected to increase from 25900 to 48400 aircraft between 2019 and 2039 [1], with a +134% for the Pacific Asia

[1] Revenue Passenger Kilometers (RPK) is an airline industry metric that shows the number of kilometres travelled by paying passengers. It is calculated as the number of revenue passengers multiplied by the total distance travelled. Since it measures the actual demand for air transport, it is often referred as airline traffic indicator. https://airlinegeeks.com/2016/01/17/airline-metrics-revenue-passenger-kilometers/

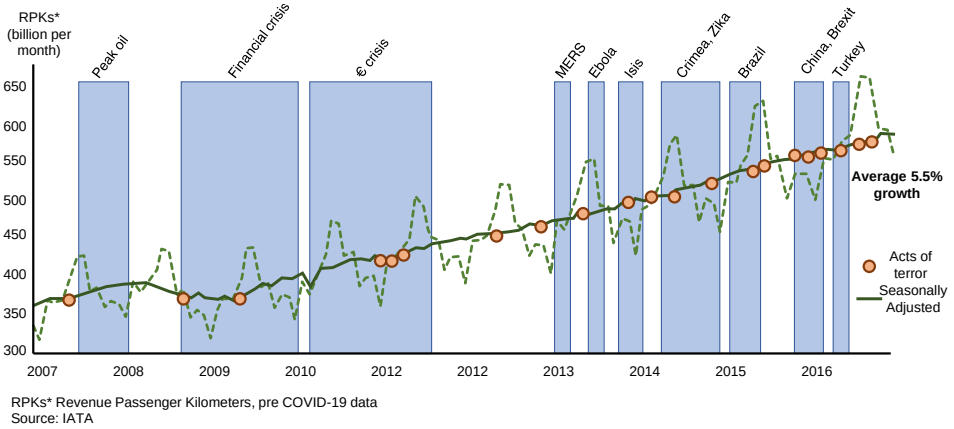

Figure 1.1: *Revenue Passenger Kilometers of the last two decades, IATA.*

segment. In the next years the skies will be more and more crowded and the aircraft related emission will increase with the same ratio if no action will be taken.

In the last years the interest in climate changes, pollution reduction and greener means of transport strongly increased and it deeply affects the aeronautical industry: air travel emissions are outpacing the prediction [2]. At the moment air transportation is responsible for the 2% of CO_2 global emission, but the next years scenario suggests a share increment.

The combination of these factors creates a challenging perspective: on one hand the air transportation is increasing and it is becoming accessible to more traveller. On the other hand, the emissions are not reducing and the effects are under everyone's eyes: desertification, extreme weather phenomena, destroyed ecosystem, species on the verge of extinction and many other dramatic situations.

Aircraft manufacturers and airliners are asked to do their best in this tough situation: they must not only limit but reduce the pollution of their airplanes in a growing market.

To support the Air Transportation Action Group (ATAG)[2] target, the European Union declared its vision for the next 30 years aviation, named Fligthpath 2050 [4]. Among the ambitious objective stated in Flightpath 2050 there is a reduction of 75% in CO_2 and 90% in NO_x emissions, qualitatively shown in Fig. 1.2.

The exploitation of current technologies (materials, new engine options, flight path optimization,...) will reduce the CO_2, but they are not sufficient to

[2] https://www.atag.org/

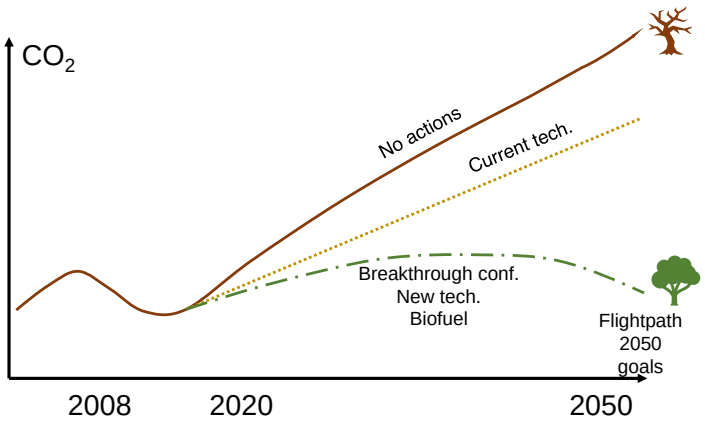

Figure 1.2: *CO2 emission and IATA 2050 goal [3].*

invert the growing trend. To obtain a significant emissions reduction, breakthrough configuration and game changer technology need to be adopted.
The emissions are directly related to the fuel burnt by an aircraft on a given route, it is possible to see an improvement of the aircraft global efficiency as a range extension with a fixed amount of fuel which means flying the original route consuming less fuel.
A simple but effective evaluation of an aircraft range is provided by the Breguet's range equation:

$$R = \frac{V_{TAS}}{g}\left(\frac{L}{D}\right)\frac{1}{SFC}ln\left(\frac{W_{MTOW}}{W_{MTOW}-W_{fuel}}\right) \tag{1.1}$$

This simplified formulation highlights three different areas which impact on the aircraft efficiency: an aerodynamic efficiency term $\frac{L}{D}$, a propulsive efficiency term given by the specific fuel consumption (SFC) and a structural efficiency term given by $ln\left(\frac{W_{initial}}{W_{initial}-W_{fuel}}\right)$.

Fig. 1.3 is taken from the study of Kharina [5] and shows the relative variation of the fuel burnt by an aircraft with respect to the 1960. This graph helps to understand the historical evolution of the efficiency process: the first significant improvement was achieved in the late '60 with the adoption of the first high by-pass ratio (HBPR) engines on the Boeing 747. In the '80 the adoption of new technologies and efficient computer aided design process, for example in the CFD field [6], led to a new season of fuel efficiency improvement. Most recently, the extending use of high-strength composites promise to increase the weight efficiency. An example of the new materials spreading is represented by the latest civil transportation air-

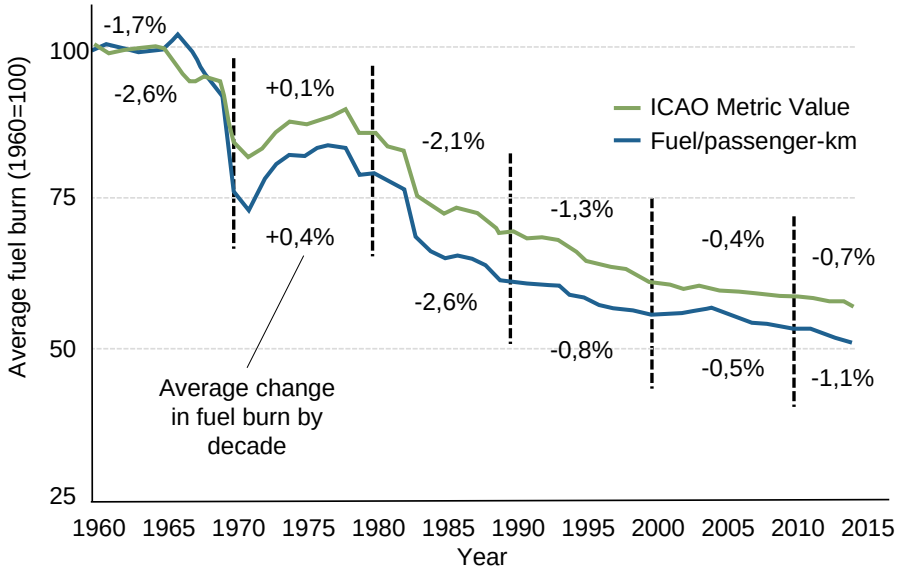

Figure 1.3: *Average fuel burn in the last 60 years [5].*

craft model rolled out by Boeing and Airbus (B787 and A350). The adoption of the composite materials in Boeing's civil airplanes was 1% for the first B747 ('70) and 3% for B757/B767, it raised to 11% for the B777 reaching >50% for the B787 [7]. In the last years tremendous improvement have been reached by STEM sciences, developing powerful hardware, materials, methodologies and discovering new concepts. High performance computers, innovative materials and their application (e.g. fibre placing), powerful actuators and more accurate design tools allow the engineers to explore new design spaces, studying unconventional solution and fully exploiting the newest technologies.

Examples of new configurations studies are the blended wing body (BWB) [8–10], truss braced wing (TBW) like Nasa's SUGAR [11], TU Delft Flying V [12], Prandtlplane [13, 14] and many other exotic configurations.

However, it must be pointed out that integrated nature of the aircraft design means that few substantive configuration changes can be made without incurring some multidisciplinary trade-offs. Just an example, increasing the wingspan also increases the wing weight. The aircraft design is a complex and multidisciplinary process, perfectly described by Joe Sutter: *The "whole" of airplane design is more than the sum of its parts. It isn't just aerodynamics, structures or propulsion, you have to make them all work together.* As C.W. Miller represented in his very famous *Dream airplanes* sketch, each

design office has its own requirements, which have to be harmonized in the best product.

It is clear that the aircraft design is an holistic process, where many dis-

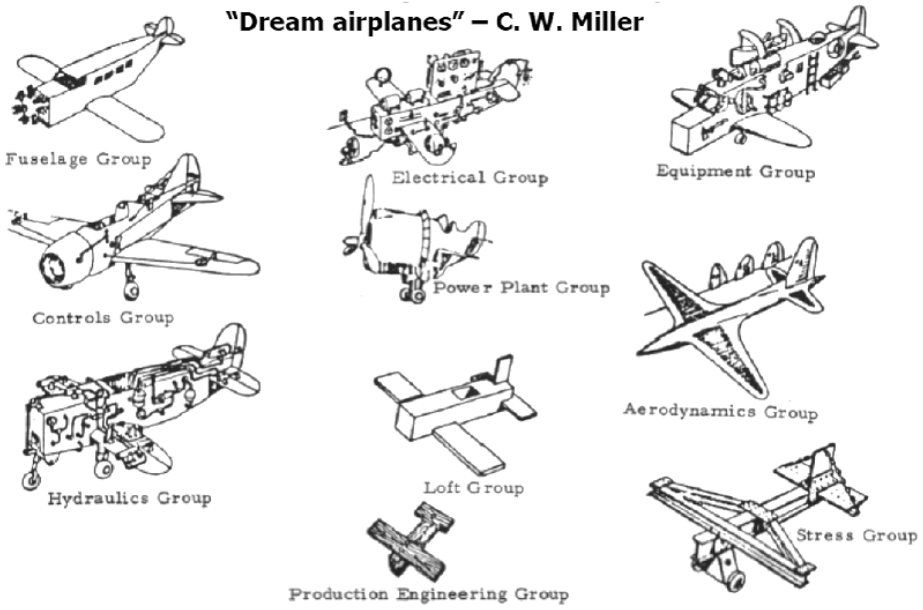

Figure 1.4: *C.W. Miller. Optimal airplane design from the perspective of engineers of different specialities.*

ciplines are involved and must be considered together. The interaction between the different engineering branches must be taken into account as soon as possible to facilitate their integration and to pursue the optimum of the whole aircraft instead of the optimal solution of each area.

The design of an innovative and brand new aircraft is a long and complex process and the experience based on common practice for conventional aluminium tube-wing configuration assumes a less relevant role, both for the usage of new materials and configurations. For this reason, new design methodologies that manage exotic configurations and new materials must be developed and employed in early design stages.

Many definitions of project are available in literature, the most complete and synthetic is the one from Rodney Turner: *"A project is an endeavour in which human, financial and material resources are organized in a novel way to undertake a unique scope of work, of given specification, within the constraints of cost and time, so as to achieve beneficial change defined by quantitative and qualitative objectives"*. In a competitive environment like aeronautic in-

dustry, time to market and development cost are key performance indexes (KPIs) for the success of a brand new program. The correct execution of feasibility and bidding phases are mandatory for a realistic evaluation of time and costs. The main problem in this phases of the project is the uncertainty, for this reason the design tools must be developed to de-risk the activities since the early design phases.
Typically, a new aircraft project is divided in three design phases where different detail levels and simulation models are used. It is a stage and gate process where a large population of configurations is reduced to the final product.

1. **Conceptual**: This is the very beginning of the project where many configurations (between 100 and 1000) are investigated with low fidelity tools, the designers have to achieve a design which satisfies the requirement in terms of performances, handling qualities, propulsion, structure and aerodynamics. The most promising configurations are further investigated in the next phases.

2. **Preliminary**: in this phase the number of configurations considered is reduced (<100) and the design is refined using higher fidelity simulation models and experiments. A further selection identifies the best solutions (5-10) among which the final aircraft configuration is chosen, leading to the so called *configuration freeze* milestone.

3. **Detailed**: the selected configuration is designed and engineered in all its aspect, defining the aircraft which will be manufactured.

Left plot of Fig. 1.5 shows the evolution of the model's accuracy used during the design process and the uncertainty level. It is important to increase the fidelity level of the tool adopted in the early design phases to reduce the uncertainty and investigate if any problem arise. Discovering design issues in the early design phases is crucial for the success of the project, in this phases (opportunity window of Fig. 1.5 right) it is possible to implement mitigation or correction actions with low cost and wide room for manoeuvre.
The aviation history is full of wrong design due to mistakes at conceptual level:

- DC-9: unexpected pitch-up and deep stall of T-tail lead to a fatal accident [15].

- DC-9-50 and MD-80: inadequate directional stiffness at high angles of attack in sideslip. Adoption of low-set nose strakes

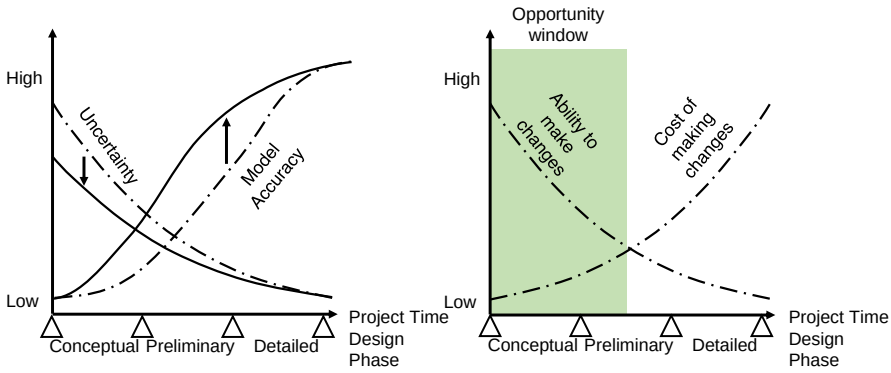

Figure 1.5: *Left: Uncertainty and model accuracy during project. Right: Cost and ability of making changes*

- SAAB2000: larger than expected wheel forces caused delay in certification. Costly redesign of elevator control system
- Boeing 777: missed horizontal tail effectiveness led to larger than needed horizontal tail [16].
- Boeing 787-10: fuselage oscillation induced by a Manoeuvre Load Control system and additional damping controller for stable but low damped wing-nacelle-fuselage mode [17].

The solution of these problems implied extra-cost for the project and a non-optimal design of the aircraft, making it performances worse. The above list shows a limited example of the problems which could emerge when designing a new aircraft, many other issues could arise especially when unconventional configurations are considered. The difference between good and bad execution of the project is when the issue emerges and how much does it cost to fix it. All the projects at their beginning are affected by an high uncertainty and low model accuracy. An enormous advantage for the designer would be the reduction of the uncertainty and a higher fidelity of the models used, because it will help them to discover potential problems in the early design phase. It is important to face, solve and mitigate the problems as soon as possible because the more time passes the harder is to correct them.
In aeronautical industry, despite the evolution of computer science, the methodologies for the first aircraft sizing are still based on statistical or experience based approaches. Two pillars of the conceptual design are the works

of D.P. Raymer [18] and E. Torenbeek [19], where the weight of structural components is based on statistic and analytical approaches. New configurations, materials and technologies makes these methods not suitable for the next generation green aircraft, simply because it is not available a sufficient statistic sample or experience to draw any conclusion.
Moreover, aeroelasticity and active control are not accounted in the early design phases, this could lead to wrong technical evaluations which translate in delay and extra cost or to a solution which is not optimal because it do not fully exploits the interaction among the involved disciplines. A classical example is the aeroelastic tailoring, where the composite materials directional stiffness is exploited to create a passive load alleviation system [20].

1.2 Research motivation, objective and thesis structure

Thesis objectives

The aim of this thesis is the development of a framework for the aero-servo-elastic optimization in the conceptual and preliminary design phases, it will help the engineers in the sizing and optimization process of the wing during the early design phases of the new green aircraft. This objective is divided in three requirements:

1. to increase the fidelity of the models adopted to describe the aircraft structure, considering composite materials as well as isotropic.

2. to evaluate the impact of active control technologies in the optimization loop and the development of a control design methodology suitable to be used in preliminary design phases.

3. to develop of an aero-servo-elastic optimization framework which exploits the enhanced structural models as well as the active control methodologies.

Finally, a validation example of the whole aero-servo-elastic optimization framework have to asses the performances of a family of possible configuration for a future civil aircraft. This exercise has to exploit the results achieved, showing the potentiality of the tool and how it could help the engineer in preliminary design phases.

Thesis structure

First of all a name is needed to avoid the repetition of "procedure", "framework" and other synonyms: in the following we will refer to it with the name

of **NeOPT**, which stands for **Neo**CASS **OPT**imizer.

Chapter 2 presents the NeoCASS aeroelastic simulation tool, providing an overview of the suite, its weaknesses and how them are filled up by the improvement of the structural model. The focus is on the three dimensional analytical description of the wingbox through a meta-model, which is generated by a geometry module. The information of the meta-model are used by several sub-module: a dedicated cross section modeller computes the beam stiffness properties and recover the stresses as well, a CAD-translator generates the detailed CAD of the wingbox in IGES or CATIA format and a meshing module creates the detailed 3D FEM mesh of the wingbox.

Chapter 3 focus is on the active control integration inside the design loop. The objective of this chapter is to illustrate a possible approach to the gust load alleviation and flutter suppression and their implementation in the optimization loop. The approach proposed does not look for the best performance achievable with the active control but it designs a simple and intuitive controller, suitable to be implemented in the sizing procedure and needed to evaluate its impact on the structural sizing.
The first part of the chapter describes the methodology and the numerical model used to design the controller while the second part shows two applications used to validated the methodology. In the first case a Gust Load Alleviation (GLA) system is designed and tested on the Simulink aero-servo-elastic simulator of the aircraft and validated on a scaled wind tunnel model. The second case considered is the design of an Active Flutter Suppression (AFS) controller which was tested numerically and experimentally in wind tunnel.

Chapter 4 describes the optimization framework, named NeOPT. The optimization loop is presented in all its components like: objective and constraints functions, design variables, variable linking, available solvers, active control design during the optimization and how all the components are harmonized in the framework.

Chapter 5 shows an application of NeOPT exploiting the improved beam model, active and passive load alleviation systems and the optimization framework described in Chapter 4. The object of the study is a twin aisle long haul (TALH) aircraft, which wing is stretched to produce a variation in the aspect ratio without increasing the wing surface. The aircraft family is sized following the NeoCASS+NeOPT procedure, using different cross sec-

tion descriptions, materials and constraints. The results show how the structural mass varies with the aspect ratio, the load condition and the active control. The outcome of this procedure is an evaluation of the fuel burn-aspect ratio trend that shows how much the emissions can be reduced modifying the wing planar shape.

Chapter 6 draws the conclusions on the PhD research and proposes the future works to further develop the approach proposed.

CHAPTER 2

Wingbox description through semi-analytical model

2.1 NeoCASS enviroment

NeoCASS is a conceptual design environment suitable for the creation of low order, medium fidelity models for structural sizing, aero-servo-elastic analysis and optimization [21] [22] [23] [24]. It is not the only product available on the market for this purpose, TU-Delft developed an in house tool named PROTEUS [25], the procedure used by Bombardier is described in [26] and the one used by Gulfstream (ATLASS) is described in [27]. An approach similar to the sizing and weight estimation implemented in NeoCASS is EMWET [28], a quasi-analytical weight estimator for lifting surface where the aerodynamic and inertial loads are used to size the structural components.
All the sizing tools start from a geometrical, possibly parametric, representation of the aircraft which is used to generate the analysis model, which can be different and with increasing level of detail.
The distinctive feature of NeoCASS with respect to the others conceptual design tool and methodologies is the fact that it sizes and works directly

on an aeroelastic stick-model: the structural beams properties are obtained through analytical computation of the sized skins thickness and stringers areas. The sizing loads are computed performing aeroelastic analysis with the same model. Some industrial approaches, like the aforementioned ATLASS, creates a global FEM model (GFEM) starting from the parametric geometrical representation of the aircraft. In this case the problem is the computation of the loads for the sizing, which is done reducing the GFEM into a stick-model for aeroelastic simulations that is used for the evaluation of the load envelope. It is a sequential optimization process where the GFEM is sized using the loads obtained with the stick model which is not sensitive to the variation of the design variables: after each sizing, the GFEM is reduced again and the loads computed once more until a convergence criterium is satisfied.
Both the path lead to a sized stick model which can be used for the aeroelastic simulation, fig. 2.1 shows a diagram with the key features of NeoCASS vs. industrial approach at conceptual design level.
Each philosophy has it own pro and cons: for example NeoCASS is not able

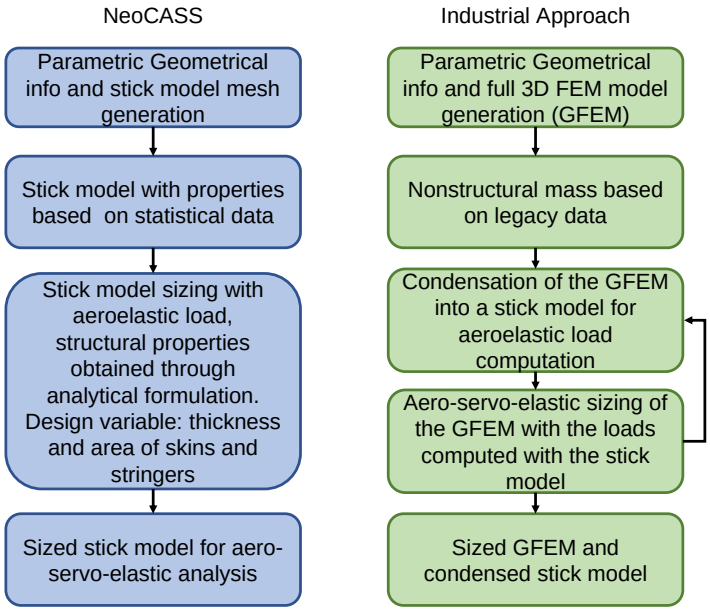

Figure 2.1: *Schematic comparison between NeoCASS and industrial approach used in conceptual design*

to consider three-dimensional effect like coupling terms introduced with the

composite materials and the realization of detailed 3D FEM and CAD models of the structural components. This chapter highlights the shortcomings of the current NeoCASS version and propose a way to partially bridge the gap with higher fidelity tools.
Fig. 2.2 shows the work-flow behind NeoCASS, which can be divided in three macro-sections.

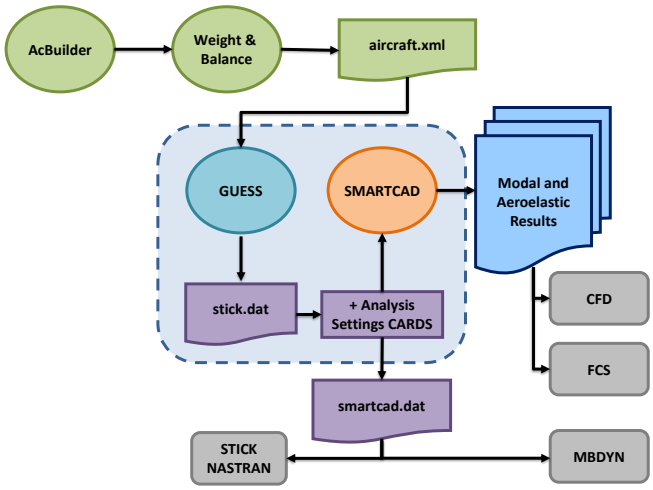

Figure 2.2: *NeoCASS framework*

1. **ACBuilder** is the parametric geometrical environment where the aircraft is graphically represented. Here the user provides the information about the layout of the aircraft like external dimensions, lifting surfaces geometry, control surfaces dimensions, landing gears, engines. The distribution of the payload along the fuselage and the fuel tank layout (wing, central fuselage, horizontal tail plane) are defined as well. In this module the materials are assigned to the different structural components, the structural stick (FEM) and aerodynamic (VLM/DLM) mesh discretization can be modified. The designer can add additional concentrated masses e.g. external storage. The Weight & Balance module provides a mass estimation of primary and secondary masses. In both cases, it is not performed a structural sizing, but a regression on bibliographical data.
   The result of this step is an *.xml* file with all the information concerning the aircraft.
2. **GUESS** module sizes the structural components of the aircraft, the

loads come from a set of trim manoeuvres compliant with EASA/CS regulation or defined by the user. The sizing process is sequential: the loads are computed with an elastic trim solution and the structure is sized to withstand them, the operation is iterated until the structural mass converges. The design variables are skins and webs thicknesses and the area of the stringers, which are used to compute the beam stiffness and mass matrices with an analytical formulation. The outcome of this module is a full-stress designed stick model with a DLM/VLM aerodynamic suitable for aero-servo-elastic analysis.

3. **SMARTCAD** is the analysis kernel which performs the simulation required. The model is described with a syntax similar to Nastran's bulk data [29] [30], this choice was made to be compatible with both the software and to use a language familiar to the aeroelastician which already uses this industrial product. The solutions available are:

   - Static analysis (like Nastran 101)
   - Normal eigenvalue analysis (like Nastran 103)
   - Rigid aerodynamic solution with a VLM solver developed from Tornado [31] which accounts for airfoil curvature and twist.
   - Elastic trim solution (like Nastran 144) with the aforementioned VLM solver.
   - Flutter analysis with P-K method (like Nastran 145) or continuation method described in [32].
   - Aeroelastic dynamic response in frequency domain (like Nastran 146)
   - State-Space solver with quasi-static approximation or identification of aerodynamic transfer function [33].

What is missing?

NeoCASS computes the stiffness and mass matrices with classical mechanics formulation, i.e. the stiffness terms are obtained multiplying the cross section inertial properties by the elastic modulus: $EJ_{xx} = E \times J_{xx}$. The beam formulation implemented in NeoCASS [34] allows to use the full 6x6 stiffness matrix of the beam element, hence all the coupling can be modelled. The current analytical method for stiffness evaluation provides only the diagonal terms of the matrix (EA, EJyy, EJzz, GJt ,GAy, GAz) and the out of diagonal terms due to the neutral axis and shear centre offsets, as

shown in Eq. (2.1).

$$\mathbf{K} = \begin{bmatrix} G \times A_x & & & & & G \times A \times X_{SC} \\ & G \times A_y & & & & -G \times A \times Y_{SC} \\ & & E \times A & -E \times A \times X_{NA} & E \times A \times Y_{NA} & \\ & & & E \times J_x & & \\ & \text{sym} & & & E \times J_y & \\ & & & & & G \times J_t \end{bmatrix} \tag{2.1}$$

The wingbox designed with GUESS is rectangular and symmetric i.e. it is described by its width, height, upper skin thickness, upper stringer area and front web thickness. The aft web thickness and lower elements are equal to the upper and front ones. This representation of the wingbox is simplified and it is valid in early design phases when stiffness and mass are not well defined yet. This limits the design space and leads to a non optimal solution because the wingbox stress distribution is not symmetric, for example the ones obtained with a 2.5g pull up and -1g push down manoeuvre.
It is possible to find an analytical solution for non symmetric and multiple cell structure [35], but this approach is not able to catch the coupling terms due to the composite materials. This aspect can not be neglected any more at conceptual design level for two main reason: the first one is that the coupling terms, specially the bending-torsion one, have an huge impact on the load distribution and dynamic stability (flutter) of the aircraft. The second reason is the aeroelastic tailoring, which allows a wider design space to optimize the structural components by acting on the coupling terms itself. To fully exploit the potential of the composite materials it is needed a tool for the correct evaluation of all the components of the stiffness matrix.
The composite wingbox modelling is not the only missing item of NeoCASS, one of the limitation of the current sizing procedure is the sequential optimization process implemented in GUESS, which uses only the static trim manoeuvres to size the structure. The trim loads are a part of the sizing envelope, the dynamic loads are not accounted and they may play a relevant role in the load envelope. Structural constraints like failure and buckling are not the only constraints which must be considered in the wing design, aeroelastic constraint must be considered as well: the aircraft have to be dynamically stable in all its flight envelope i.e. there is no flutter and the handling qualities must meet the prescribed value without loosing their effectiveness with the increasing wing flexibility.
In this environment, the natural position of NeOPT is right after GUESS for two reason: the first one is because thanks to the cross-section modeller it is possible to refine the description of stiffness and mass matrices of the stick model before running further analyses, the second one is because the

preliminary sizing performed by GUESS can be used as starting point for the optimization of the wingbox. The block diagram of NeoCASS becomes the one in Fig. 2.3.

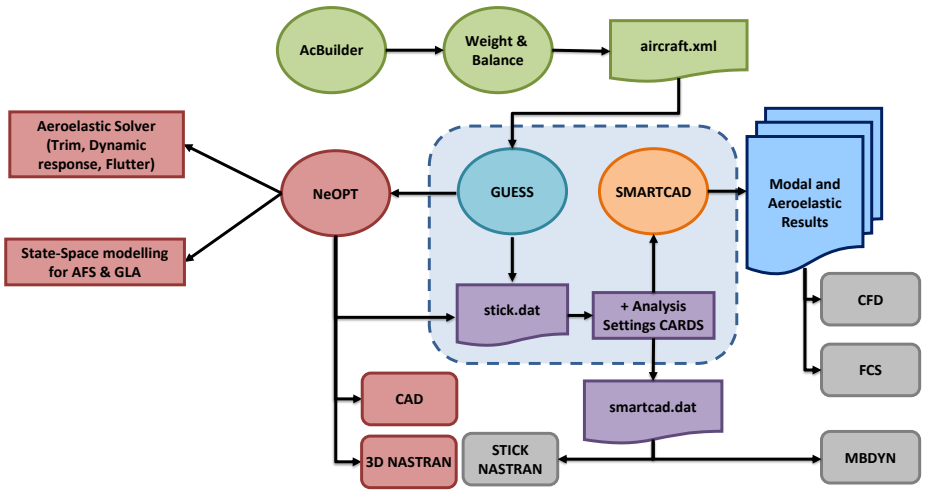

Figure 2.3: *NeoOPT position inside NeoCASS framework*

2.2 Wingbox meta-model

The meta-model is an analytical three-dimensional representation of the wingbox containing both geometrical and structural information.
The concept recalls the approach proposed in [36] and further develop the idea leading to an higher fidelity and single-environment application.
The stick model realized by GUESS describes the wingbox only with 1D beam elements, hence all the information about the structural components (geometry, thickness,...) are not used any more. The meta-model creates a database of the wingbox properties which is used to store and preserve its physical properties, this information allow to expand the 1D beam element in the correspondent analytical representation of the wingbox's chunk.
It is used to elaborate the information necessary to realize an analysis model or to post-process analysis results. Fig. 2.4 illustrates the pivotal role of the meta-model with respect to all the models available as output, its information are used to realized different analysis model (stick model, cross section model or 3D FEM model) and to post-process the results of each analysis, typically the internal forces coming from the stick model are used to recover

the cross sectional stresses which are expanded in 3D to obtain the wingbox stress state.

A geometry module (Sec. 2.3) process the geometrical information of the

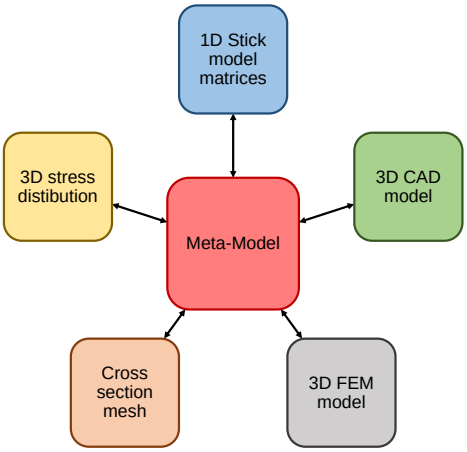

Figure 2.4: *Meta-model communication with available models*

wing and produces a database where are stored the intersection between the ribs and the stringers. Once obtained the 3D points it is possible to connect them in different ways to obtain different elements and models. A connectivity across the chordwise direction creates the 2D representation of the cross section for each rib, a global connectivity creates a 3D mesh of the wingbox suitable to realize a CAD or FEM model. The geometrical information alone are useless from the structural point of view, the properties of the structural elements (area and thickness) and the material characteristics are associated to the connectivity in order to identify each element of the wingbox in terms of position and properties.

The meta-model is more than a simple database of nodes, connections and properties. It preserve the coherence among the different models, this means that whichever modification of a property in one domain is automatically transmitted to the others models.

The analysis model that can be obtained through the meta model are:

- A cross section 2D FEM model, which is used by NeoANBA (Sec. 2.4) to obtain the beam stiffness and mass matrices.
- The aircraft stick model with the updated stiffness properties.
- The 3D FEM detailed model of the wingbox.

- The CAD model (IGES or CATIA) of the wingbox.

2.3 Geometry module

This module creates the meta-model starting from the information inherited from AcBuilder and GUESS. The first step is the identification of the wingbox and of the wing beams. The airfoils and the spar chordwise position provide a first spatial representation of the wingbox (Fig. 2.5).

The wingbox shape is obtained intersecting the external wing shape with

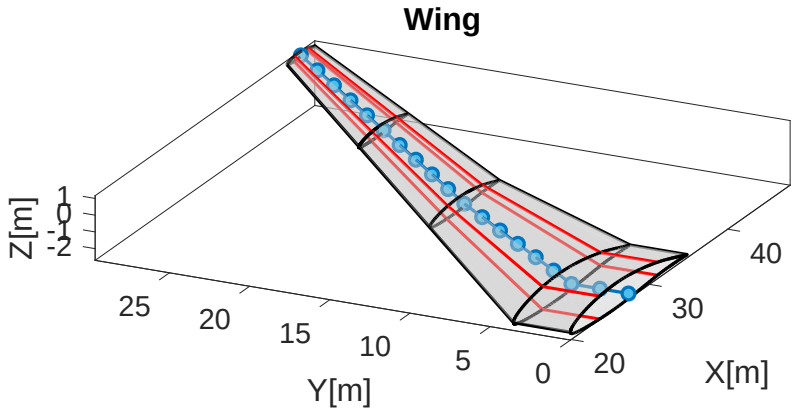

Figure 2.5: *Wing inherited from AcBUilder*

a set of planes representing the front and aft spar. Matlab is not a CAD program, where high level function for surfaces intersection are available. To overcome this problem, NeOPT exploits the algorithm described in [37] and implemented in [38], which allows to compute the intersections between triangle meshed surfaces. This method provides a set of points which describes the intersection curve between the wing external shape and the spars. Fig. 2.6 shows an example of identified wingbox.

At this point the wingbox is its external surface and no stringer or ribs are placed. The next step is the computation of the rib intersection with the wingbox shape. NeOPT computes the optimal rib spacing starting from an user provided rib pitch and creates a set of planes normal to the beam axis (Fig. 2.7).

The rib planes intersection with the wing box external shape provides the surface of the ribs. When a kink occurs, if the gap between two consecutive ribs is too width, a set of ribs is placed and automatically intersected (Fig. 2.9).

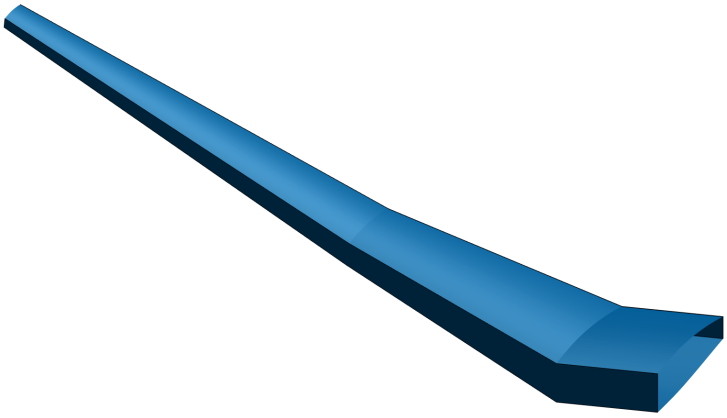

Figure 2.6: *Identified wingbox*

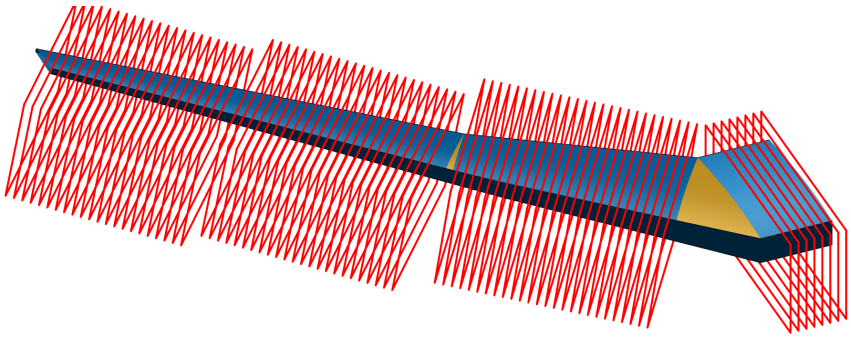

Figure 2.7: *Planes used to cut the ribs*

The last geometrical information needed to fully describe the wingbox is

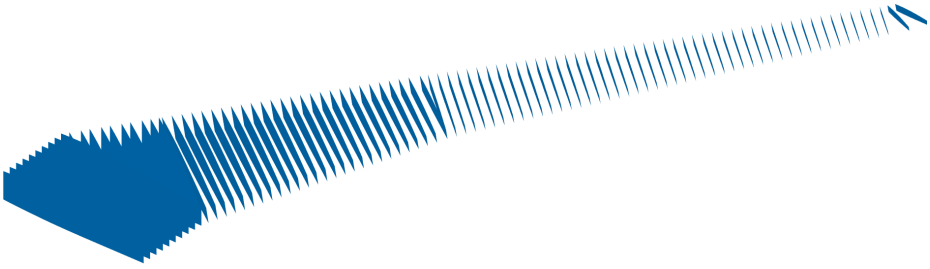

Figure 2.8: *Rib position*

the position of the stingers, computed starting from an user defined stringer

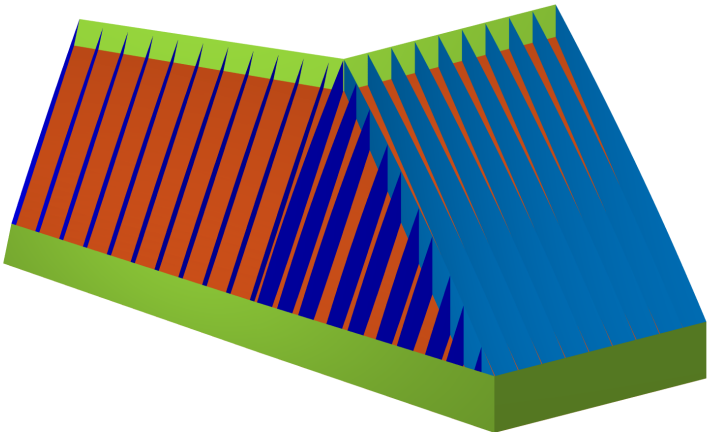

Figure 2.9: *Detail of ribs on kink*

pitch. NeOPT manages three different layout of equally spaced stringers in chordwise direction, in this case the driver is the reference plane for their orientation. They can be parallel to the front spar, to the beam axis or to the aft spar. If the wingbox is tapered, the stringers automatically interrupt on a rib before clashing with a spar, like Fig. 2.10 shows.

The result of this "cut & intersect" procedure is the coordinates of the inter-

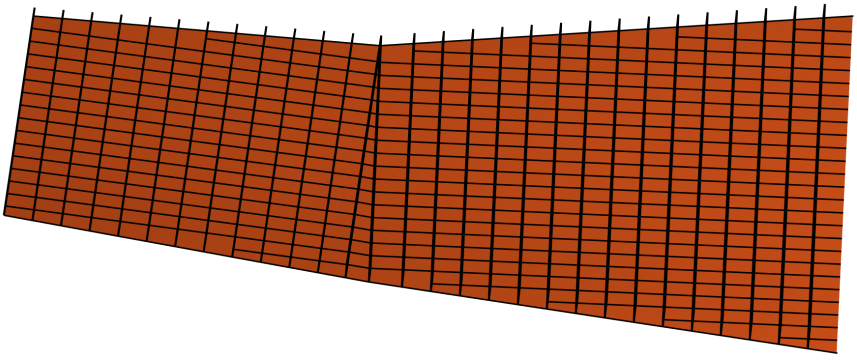

Figure 2.10: *Example of stringer aligned to the beam axis, interruption on the front and aft spars*

sections between stringers and ribs. This cloud of points and its properties is the meta-model, through which is possible to organize the data and realize several representation of the wingbox, as shown in Fig 2.4.

The first model produced is the FEM of the cross section: the 3D points

of each ribs are projected on a 2D plane and the geometrical and material information are organized in the format required by NeoANBA. Fig. 2.11 shows an example of a cross-section mesh used by the cross section solver. The model is analysed obtaining the beam stiffness and mass matrices together with the stress distribution for unit loads. Since the method is linear, the stress distribution due to a real case is obtained simply scaling the unit load stress by the magnitude of internal loads (the method will be deeply discussed in sec. 2.4).

Another analysis model which is created is a Nastran's 3D FEM detailed

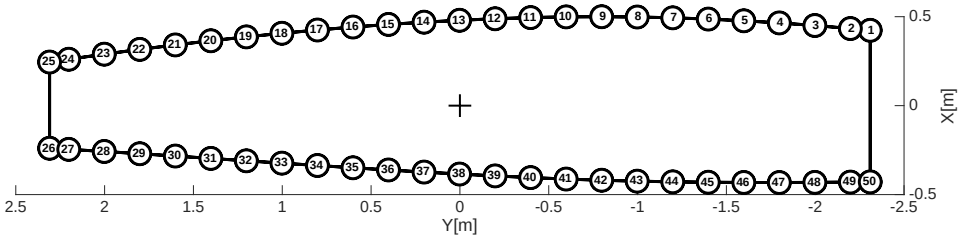

Figure 2.11: *Example of a NeoANBA cross section mesh*

model of the wingbox, shown in Fig. 2.12. The meta-model allows to define the desired mesh refinement in three directions: in chordwise direction it must be specified the number of elements between the stringers, in spanwise direction the number between the ribs must be provided and in the third direction the number of elements of the spars' webs. The properties (thickness and inertial) of the elements (PSHELL and PBAR) are inherited from the meta-model, as well as the material characteristic and ply orientation in case of composite (MAT1 or MAT8). The model can be realized with the properties obtained with GUESS and with the ones obtained after the NeOPT sizing.

This model is not used during the optimization, but it is ready for the next steps of the design procedure, where higher fidelity models are necessary for more specific analysis e.g. accurate stress distribution computation.

It is important to notice that the relation between 3D FE model and the beam properties is known through the meta-model, this means that whichever property variation applies both to the stick-model and to the 3D FE model. This property is exploited when NeOPT is used to reduce computationally burdensome 3D FEM into light and agile stick-model suitable for aero-servo-elastic analyses, or when higher fidelity analysis are required and a 3D FE model is needed.

The last model that can be created is the full 3D CAD model of the wingbox (Fig. 2.13), available in IGES or CATIA format.

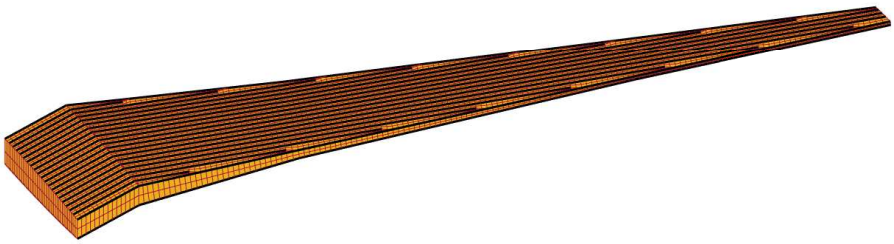

Figure 2.12: *Example of a wingbox 3D FEM mesh realized with geometry module*

When the CATIA format is required, NeOPT writes a VBA Marco which

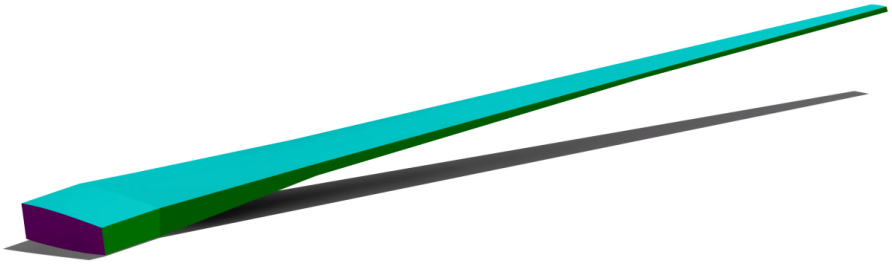

Figure 2.13: *Wingbox representation in a CAD environment*

runs inside the CAD program, creating in a parametric way the points, the splines and the surfaces which represents the wingbox structural elements. When the IGES format is selected, NeOPT writes an ASCII file compliant with the CAD format. In this case the curves are described by Non-Uniform Rational B-Splines (NURBS), which allows to describe the geometry with an analytical formulation.
This kind of description of the geometrical entities is widely adopted by drawing software and FEM pre-processors, the equation in the following comes from chapter 4 of [39]. The p-th degree NURBS curve is defined in Eq. (2.2)

$$\mathbf{X}(u) = \frac{\sum_{i=0}^{N} N_{i,p}(u) w_i \mathbf{P}_i}{\sum_{i=0}^{N} N_{i,p}(u) w_i} \tag{2.2}$$

Where $\mathbf{X}$ are the physical coordinate in the space obtained evaluating the NURBS in $u \in [a, b]$ $a = 0,\ b = 1$, which is a non-dimensional curvilinear abscissa. $\mathbf{P}_i$ is the i-th control point and w_i the associated weight. $N_{i,p}$ are the p-th degree B-spline basis function defined on the non-periodic and

non-uniform knot vector $\mathbf{U}$:

$$\mathbf{U} = \{\underbrace{a, \ldots, a}_{p+1}, u_{p+1}, \ldots, u_{n-p-1}, \underbrace{b, \ldots, b}_{p+1}\} \tag{2.3}$$

By writing:

$$\mathbf{R}_{i,p}(u) = \frac{N_{i,p}(u) w_i \mathbf{P}_i}{\sum_{j=0}^{N} N_{j,p}(u) w_J} \tag{2.4}$$

It is possible to rewrite Eq. (2.2) as:

$$\mathbf{X}(u) = \sum_{i=0}^{N} \mathbf{R}_{i,p}(u) \mathbf{P}_i \tag{2.5}$$

The equations from Eq. (2.2) to Eq. (2.5) are used to define a physical point when the NURBS parameters $\mathbf{R}_{i,p}, \mathbf{P}_i$ are fully known, in our case there are known the physical points $\mathbf{X}$ and the NURBS parameters need to be defined to obtain the analytical expression of the NURBS passing through the physical points. For this reason a procedure is implemented to define the control points and the weights starting from an arbitrary set of physical coordinates.
The points are translated into the non-dimensional curvilinear abscissa $\mathbf{X}_k \rightarrow u_k$, which becomes the knot vector in the form of Eq. (2.3). By imposing $w_i = 1$, it is possible to write a well posed linear problem by imposing that the NURBS evaluated in u_k returns $\mathbf{X}_k$ and solving for $\mathbf{P}_i$. To well-pose the problem the number of control points must be equal to the number of physical points.

$$\mathbf{X}_k(u_k) = \sum_{i=0}^{N} \mathbf{R}_{i,p}(u_k) \mathbf{P}_i \tag{2.6}$$

and it leads to:

$$\mathbf{AP} = \mathbf{X} \rightarrow \mathbf{P} = \mathbf{A}^{-1}\mathbf{X} \tag{2.7}$$

The solution of Eq. (2.7) provides the position of the control points and together with the defined weights allow to analytically describe the NURBS passing through the desired points.
The geometrical description trough NURBS curve or parametric CAD open new design possibilities. The first one is the capability of describing the geometry through an analytical formulation avoiding approximation. The geometry is known only on the intersection between stringer and ribs, if additional points are required between two consecutive points linear interpolation leads to an error as depicted in Fig. 2.14. The analytical description

of the curve allows to thicken the mesh or add points without errors. This is useful when significant geometric discretization are needed for CFD analysis, avoiding sharp edges during the refinement process.
Another possibility offered by NURBS geometrical description is to face the

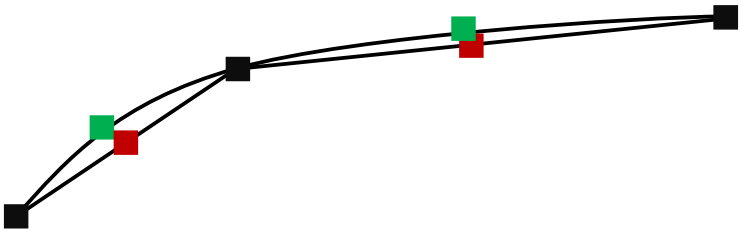

Figure 2.14: *Approximation error when using linear interpolation to refine the geometry*

iso-geometric approach, proposed by T. Hughes [40] [41]. This approach is an alternative to the iso-parametric Finite Element analysis, which substitutes the iso-parametric shape function with the NURBS. This approach overcomes the duality of geometrical description and FE domain, using a common dataset to design and analyse a problem.
The CAD parametric manipulation is another possibility, the shape modification can be obtained manipulating the NURBS control points position as in Fig. 2.15a, modifying the control points weights or acting on the points used as support for the spline definition in CAD environment, like Fig. 2.15b

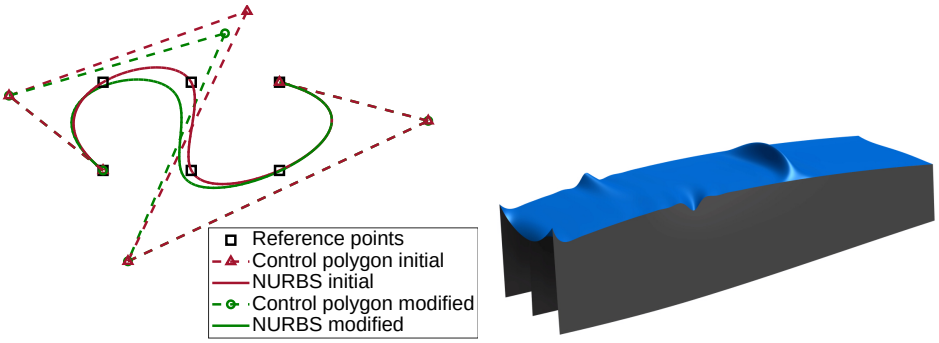

(a) *Example of NURBS modification by changing the control points*

(b) *Wingbox deformation in a parametric CAD environment*

Figure 2.15: *NURBS geometry manipulation*

2.4 NeoANBA

In chapter 1 we already spent some words about the importance of increasing the fidelity of the numerical models adopted in early design phases, the goal of this section is to present the improvement achieved in beam description. One of the limits of NeoCASS is the reduced availability of FEM element type, since it was born as an aircraft conceptual design tool and not as a FEM solver. The main structural components of the aircraft are slender bodies and it is a common practice to represent them with a beam approximation. For this reason the only structural element implemented in NeoCASS is the beam.
The beam properties are provided in a Nastran format, the set of information required to define the 1D element are the end nodes, the orientation in the space, if present the shear centre and neutral axis offsets, the material and the cross section inertial properties (GRID, PBEAM, CBEAM and MAT cards in [30]). The elements of the stiffness matrix are obtained by multiplying the cross section geometrical information by the elastic modulus of the material e.g. the axial stiffness is given multiplying the cross section area by the elastic modulus $EA = E \times A$.
Performing an optimization using as design variable the PBEAM entries can lead to values of stiffness which are not physically achievable, for this reason the design variables used by NeOPT are the thicknesses of the main wingbox components (further details in Sec. 4.2.1).
Many analytical formulation can be used to get the stiffness and inertial properties of a cross section starting from the geometry and material distribution. Usually axial and bending stiffness are not difficult to obtain, problems may arise for the correct evaluation of the torsional stiffness. The easiest way to compute this value is the Bredt's formula, which allows to compute the torsional stiffness of whichever thin walled closed section. More sophisticated methods like [42] and [35] come to a suitable formulation of the problem for semimonocoque structure like wingbox. This last formulation overcomes hyperstaticity issues e.g. multiple spar section. Moreover it accounts for warping effects, wing taper, shear centre and neutral axis offset but it does not account for coupling effects introduced with orthotropic material e.g. Carbon Fibre Reinforced Polymer (CFRP).
The evolution and diffusion of Polymer-Matrix Composite (PMC) in aerospace industry requires design methodologies that manage these materials, describing their behaviour since the early design phases.
Tackling the aforementioned request, a new section modeller is developed on the basis of ANBA [43] and it is named NeoANBA (NeoCASS + ANBA).

The characteristics of this section modeller are suitable to easily pass from a 3D representation of the wingbox to a stick model through the meta-model and vice-versa. The possibility of automatically switch from a 3D to a 1D model without losing information is very powerful because each change in one domain is automatically reflected in the other domain, e.g. component thickness variation becomes stiffness and mass matrices variation.
In the previous sections NeoANBA is described as a section modeller which computes structural beam matrices and recovers the stress state, the next section finally provides a description of the tool.

2.4.1 NeoANBA mathematical model

Fig. 2.16 shows the kinematic of the cross section. The displacement of a point $\mathbf{P}$ is decomposed into the rigid displacement of the cross section $\mathbf{v}$ and the warping contribution $\mathbf{g}$. The rigid displacement $\mathbf{v}$ is the combination of the section origin displacement and rotation. The model accounts for a

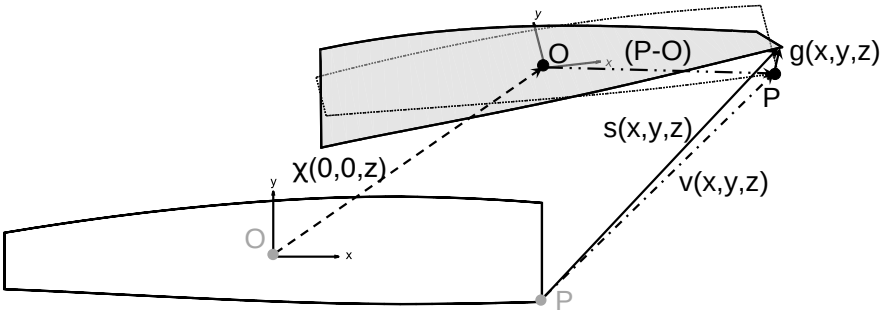

Figure 2.16: *Section kinematic*

3D displacement Eq. (2.8), 6 deformation Eq. (2.9) and 6 stress Eq. (2.10) components, which are partitioned to have the ones acting on the cross section in the last three elements of the vector.

$$\mathbf{s} = [u\ v\ w]^T \tag{2.8}$$

$$\boldsymbol{\varepsilon} = [\gamma_{xy}\ \varepsilon_x\ \varepsilon_y\ \gamma_{xz}\ \gamma_{yz}\ \varepsilon_z]^T \tag{2.9}$$

$$\boldsymbol{\sigma} = [\tau_{xy}\ \sigma_x\ \sigma_y\ \tau_{xz}\ \tau_{yz}\ \sigma_z]^T \tag{2.10}$$

The relation between strain and stress Eq. (2.11) is linear and it is provided by the constitutive law $\mathbf{C}$.

$$\boldsymbol{\sigma} = \mathbf{C}\boldsymbol{\varepsilon} \tag{2.11}$$

With an extraction matrix Eq. (2.12) $\mathbf{S}$ it is possible to get the cross section normal stress vector $\mathbf{p}$.

$$\mathbf{p} = [\tau_{xz}\ \tau_{yz}\ \sigma_z]^T = [\mathbf{0}_3\ \mathbf{I}_3]\boldsymbol{\sigma} = \mathbf{S}^T\boldsymbol{\sigma} \tag{2.12}$$

Eq. (2.13) describes the rigid displacement of an arbitrary point P through the cross section origin displacement $\boldsymbol{\chi}$ and rotation $\boldsymbol{\varphi}$, grouped in the vector $\mathbf{r}$.

$$\mathbf{v} = \boldsymbol{\chi} + [(\mathbf{P}-\mathbf{O})\wedge]^T\boldsymbol{\varphi} = [\mathbf{I}\ [(\mathbf{P}-\mathbf{O})\wedge]^T]\begin{bmatrix}\boldsymbol{\chi}\\ \boldsymbol{\varphi}\end{bmatrix} = \mathbf{Z}\mathbf{r} \tag{2.13}$$

The total displacement of the point $\mathbf{P}$ is given by Eq. (2.14), where the warping is accounted and the dependancies from the *x,y,z* coordinates of each term is shown.

$$\mathbf{s}(x,y,z) = \mathbf{Z}(x,y)\mathbf{r}(0,0,z) + \mathbf{g}(x,y,z) \tag{2.14}$$

Eq. (2.15) shows the relation between displacement and strain, which can be decomposed as in Eq. (2.16), where the derivative are splitted and the derivative with respect to *z* is isolated.

$$\boldsymbol{\varepsilon} = \mathbf{D}\mathbf{s} = \begin{bmatrix} \frac{\partial}{\partial y} & \frac{\partial}{\partial x} & 0 \\ \frac{\partial}{\partial x} & 0 & 0 \\ 0 & \frac{\partial}{\partial y} & 0 \\ \frac{\partial}{\partial z} & 0 & \frac{\partial}{\partial x} \\ 0 & \frac{\partial}{\partial z} & \frac{\partial}{\partial y} \\ 0 & 0 & \frac{\partial}{\partial z} \end{bmatrix} \begin{bmatrix} u \\ v \\ w \end{bmatrix} \tag{2.15}$$

$$\mathbf{D} = \begin{bmatrix} \frac{\partial}{\partial y} & \frac{\partial}{\partial x} & 0 \\ \frac{\partial}{\partial x} & 0 & 0 \\ 0 & \frac{\partial}{\partial y} & 0 \\ 0 & 0 & \frac{\partial}{\partial x} \\ 0 & 0 & \frac{\partial}{\partial y} \\ 0 & 0 & 0 \end{bmatrix} + \begin{bmatrix} 0 & 0 & 0 \\ 0 & 0 & 0 \\ 0 & 0 & 0 \\ \frac{\partial}{\partial z} & 0 & 0 \\ 0 & \frac{\partial}{\partial z} & 0 \\ 0 & 0 & \frac{\partial}{\partial z} \end{bmatrix} = \mathbf{D}_{xy} + \mathbf{S}(\cdot)_z \tag{2.16}$$

The derivative partition in Eq. (2.16) leads to the strain description of Eq. (2.17), which can be further divided in rigid section ε_r and warping ε_g strain leading to Eq. (2.18)

$$\boldsymbol{\varepsilon} = \mathbf{D}_{xy}\mathbf{s} + \mathbf{S}\mathbf{s}_{\partial z} \tag{2.17}$$

$$\boldsymbol{\varepsilon} = \mathbf{D}_{xy}\mathbf{Z}\mathbf{r} + \mathbf{S}\mathbf{Z}\mathbf{r}_{\partial z} + \mathbf{D}_{xy}\mathbf{g} + \mathbf{S}\mathbf{g}_{\partial z} = \boldsymbol{\varepsilon}_r + \boldsymbol{\varepsilon}_g \tag{2.18}$$

The numerical model has to describe a rigid body motion of the beam body, i.e. the rigid displacement does not produce rigid section strain. To better study this property, rigid section strain of Eq. (2.19) are portioned as in Eq. (2.20).

$$\boldsymbol{\varepsilon}_r = \mathbf{D}_{xy}\mathbf{Z}\mathbf{r} + \mathbf{S}\mathbf{Z}\mathbf{r}_{\partial z} \tag{2.19}$$

$$\boldsymbol{\varepsilon}_r^C = \begin{bmatrix} \gamma_{xy} \\ \varepsilon_x \\ \varepsilon_y \end{bmatrix}, \ \boldsymbol{\varepsilon}_r^N = \begin{bmatrix} \gamma_{xz} \\ \gamma_{yz} \\ \varepsilon_z \end{bmatrix} \tag{2.20}$$

First term of Eq. (2.20), $\boldsymbol{\varepsilon}_r^C$, is null irrespectively to $\mathbf{r}$.

$$\boldsymbol{\varepsilon}_r^C = \mathbf{0} \ \forall \mathbf{r}, \mathbf{r}_{\partial z} \tag{2.21}$$

Focusing on second term of Eq. (2.20), we can expand the expression as in Eq. (2.22), where $\mathbf{D}_N$ matrix is the last three rows of $\mathbf{D}_{xy}$ in Eq. (2.16).

$$\boldsymbol{\varepsilon}_r^N = \mathbf{D}_N\boldsymbol{\chi} + \mathbf{D}_N[(\mathbf{P}-\mathbf{O})\wedge]^T\boldsymbol{\varphi} + \boldsymbol{\chi}_{\partial z} + [(\mathbf{P}-\mathbf{O})\wedge]^T\boldsymbol{\varphi}_{\partial z} \tag{2.22}$$

First term of Eq. (2.22) is equally null, while substituting Eq. (2.23) in Eq. (2.22) one obtains Eq. (2.24).

$$\mathbf{D}_N[(\mathbf{P}-\mathbf{O})\wedge]^T = \begin{bmatrix} 0 & 0 & \frac{\partial}{\partial x} \\ 0 & 0 & \frac{\partial}{\partial y} \\ 0 & 0 & 0 \end{bmatrix} \begin{bmatrix} 0 & 0 & -y \\ 0 & 0 & x \\ y & -x & 0 \end{bmatrix}^T = \begin{bmatrix} 0 & -1 & 0 \\ 1 & 0 & 0 \\ 0 & 0 & 0 \end{bmatrix} = \mathbf{t} \tag{2.23}$$

$$\boldsymbol{\varepsilon}_r^N = \mathbf{t}\boldsymbol{\varphi} + \boldsymbol{\chi}_{\partial z} + [(\mathbf{P}-\mathbf{O})\wedge]^T\boldsymbol{\varphi}_{\partial z} \tag{2.24}$$

Two equation can be derived to grant $\boldsymbol{\varepsilon}_r^N$ to be null everywhere and are grouped in Eq. (2.25), which in matrix form becomes Eq. (2.26).

$$\begin{cases} \mathbf{t}\boldsymbol{\varphi} + \boldsymbol{\chi}_{\partial z} = 0, & (x,y) = 0 \\ [(\mathbf{P}-\mathbf{O})\wedge]^T\boldsymbol{\varphi}_{\partial z}, & \forall (x,y) \neq 0 \end{cases} \tag{2.25}$$

$$\begin{bmatrix} 0 & \mathbf{t} \\ 0 & 0 \end{bmatrix} \begin{bmatrix} \boldsymbol{\chi} \\ \boldsymbol{\varphi} \end{bmatrix} + \begin{bmatrix} \boldsymbol{\chi} \\ \boldsymbol{\varphi} \end{bmatrix}_{\partial z} = \mathbf{T}\mathbf{r} + \mathbf{r}_{\partial z} = \mathbf{0} \tag{2.26}$$

If Eq. (2.26) is satisfied, the displacement of the reference line is a rigid body motion of the beam which does not produce any deformations, otherwise it provides an indication of how far the displacement is from a rigid body motion. Eq. (2.27) introduces the generalized strain parameter $\boldsymbol{\Psi}$ which quantify the amount of deformation due to the motion of the beam's reference

line. If $\mathbf{\Psi} = 0$ a rigid body motion occurs, otherwise the motion produces cross sectional deformation.
$\mathbf{\Psi}(1:2)$ are the transverse shear in x and y direction, $\mathbf{\Psi}(3)$ is the axial strain, $\mathbf{\Psi}(4:5)$ are the deformation due to bending around x and y and $\mathbf{\Psi}(6)$ is the shear deformation due to torsion.

$$\mathbf{\Psi} = \mathbf{Tr} + \mathbf{r}_{\partial z} = \begin{bmatrix} -\beta_0 + u_{0\partial z} \\ \alpha_0 + v_{0\partial z} \\ w_{0\partial z} \\ \alpha_{0\partial z} \\ \beta_{0\partial z} \\ \gamma_{0\partial z} \end{bmatrix} \tag{2.27}$$

Using the definition of $\mathbf{\Psi}$, Eq. (2.19))can be rearranged into Eq. (2.28).

$$\boldsymbol{\varepsilon}_r = \mathbf{SZ\Psi} \tag{2.28}$$

Now all the kinematic assumption are presented and it is possible to write the virtual work principle for the problem, described by Eq. (2.29).

$$\int_v \delta\boldsymbol{\varepsilon}^T \boldsymbol{\sigma} dV = \int_v \delta\mathbf{s}^T \mathbf{F} dV + \int_{\partial V} \delta\mathbf{s}^T \mathbf{f} dS \tag{2.29}$$

It is assumed the there are not volume forces and that the external surfaces is divided into three portion: the two cross sections A_z, A_{z+dz} and lateral surface S_l (Fig: 2.17). This surface partitioning and the null volume forces

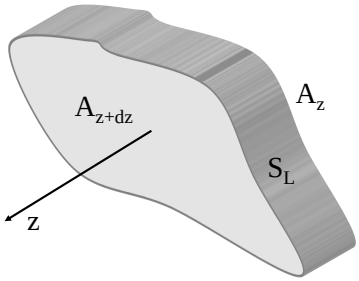

Figure 2.17: *Beam surfaces decomposition*

lead to and external work in the form of Eq. (2.30).

$$\int_{\partial V} \delta\mathbf{s}^T \mathbf{f} dS = \int_{A_{z+dz}} \delta\mathbf{s}^T \mathbf{f}_{A_{z+dz}} dS + \int_{A_z} \delta\mathbf{s}^T \mathbf{f}_{A_z} dS + \int_{S_l} \delta\mathbf{s}^T \mathbf{f}_{S_l} dS \tag{2.30}$$

Accounting for the hypothesis in Eq. (2.31), Eq. (2.30) can be rearranged in the form of Eq. (2.32).

$$\text{Hypothesis} = \begin{cases} \mathbf{S}_l = 0 \\ A = \text{const.} \\ \mathbf{f}_{z+dz} = \mathbf{p} \\ \mathbf{f}_z = -\mathbf{p} \end{cases} \tag{2.31}$$

$$\begin{gathered} \int_{\partial V} \delta \mathbf{s}^T \mathbf{f} dS = \int_{A_z} \delta \mathbf{s}^T \mathbf{p}_{A_z} dA - \int_{A_{z+dz}} \delta \mathbf{s}^T \mathbf{p}_{A_{z+dz}} dA = \\ dz \frac{\partial}{\partial z} \int_{A_z} \delta \mathbf{s}^T \mathbf{p}_{A_z} dA = dz \int_{A_z} (\delta \mathbf{s}^T \mathbf{p}_{A_z})_{\partial z} dA \end{gathered} \tag{2.32}$$

Eq. (2.32) leads to the VWP per unit length described by Eq. (2.33)

$$\int_A \delta \boldsymbol{\varepsilon}^T \boldsymbol{\sigma} dA = \int_{A_z} (\delta \mathbf{s}^T \mathbf{P}_{A_z})_{\partial z} dA \tag{2.33}$$

It is possible to consider the internal loads as the resultant of the stresses acting on the cross section, expressed in the form of Eq. (2.34).

$$\boldsymbol{\theta} = \int_A \begin{bmatrix} 1 & 0 & 0 & 0 & 0 & -y \\ 0 & 1 & 0 & 0 & 0 & x \\ 0 & 0 & 1 & y & -x & 0 \end{bmatrix}^T \begin{bmatrix} \sigma_z \\ \tau_{xz} \\ \tau_{yz} \end{bmatrix} dA = \int_A \mathbf{Z}^T \mathbf{p} dA \tag{2.34}$$

Eq. (2.34) leads to Eq. (2.35), which is the classic definition of internal forces as the section stresses integration over the section area.

$$\boldsymbol{\theta} = \begin{bmatrix} \int_A \sigma_z dA \\ \int_A \tau_{xz} dA \\ \int_A \tau_{yz} dA \\ \int_A -y\sigma_z dA \\ \int_A x\sigma_z dA \\ \int_A y\tau_{xz} - x\tau_{yz} dA \end{bmatrix} = \begin{bmatrix} T_z \\ T_x \\ T_y \\ M_x \\ M_y \\ M_z \end{bmatrix} \tag{2.35}$$

All the equations of this section are written in the continuous domain, now a numerical strategy is needed to solve the problem. Among the many possibilities, finite element method is adopted to approximate the warping field. In Eq. (2.36) the unknown warping field is approximated through a set of shape function $\mathbf{N}$, the nodal warping $\mathbf{a}$ is unknown at the element nodes.

$$\mathbf{g} = \mathbf{N}\mathbf{a} \tag{2.36}$$

The FE formulation leads to the displacement approximation of Eq. (2.37) and the strain of Eq. (2.38).

$$\mathbf{s} = \mathbf{Z}\mathbf{r} + \mathbf{N}\mathbf{a} \tag{2.37}$$

$$\boldsymbol{\varepsilon} = \mathbf{S}\mathbf{Z}\boldsymbol{\Psi} + \mathbf{D}_{xy}\mathbf{N}\mathbf{a} + \mathbf{S}\mathbf{N}\mathbf{a}_{\partial z} = \begin{bmatrix}\mathbf{B}_{\Psi} & \mathbf{B}_a & \mathbf{B}_{a\partial z}\end{bmatrix} \begin{bmatrix}\boldsymbol{\Psi} \\ \mathbf{a} \\ \mathbf{a}_{\partial z}\end{bmatrix} = \mathbf{B}\mathbf{q} \tag{2.38}$$

It is now possible to write the internal work replacing the stress with the constitutive law of Eq. (2.11). Following an integration rule and assembling the elements, the internal work becomes Eq. (2.39).

$$\delta\mathcal{W}_{int} = \int_A \delta\boldsymbol{\varepsilon}^T \mathbf{C}\boldsymbol{\varepsilon} dA = \delta\mathbf{q}^T \int_A \mathbf{B}^T\mathbf{C}\mathbf{B} dA\, \mathbf{q} = \delta\mathbf{q}\mathbf{W}\mathbf{q} \tag{2.39}$$

$\mathbf{W}$ is a 3x3 blocks symmetric matrix, each sub-matrix is described in Eq. (2.40) and assembled in Eq. (2.41).

$$\begin{aligned}
\hat{\mathbf{K}} &= \textstyle\int_a \mathbf{B}_a^T\mathbf{C}\mathbf{B}_a dA \\
\tilde{\mathbf{K}} &= \textstyle\int_a \mathbf{B}_{a\partial z}^T\mathbf{C}\mathbf{B}_{a\partial z} dA \\
\bar{\mathbf{K}} &= \textstyle\int_a \mathbf{B}_{\Psi}^T\mathbf{C}\mathbf{B}_{\Psi} dA \\
\hat{\mathbf{R}} &= \textstyle\int_a \mathbf{B}_a^T\mathbf{C}\mathbf{B}_{\Psi} dA \\
\tilde{\mathbf{R}} &= \textstyle\int_a \mathbf{B}_{a\partial z}^T\mathbf{C}\mathbf{B}_{\Psi} dA \\
\hat{\mathbf{H}} &= \textstyle\int_a \mathbf{B}_a^T\mathbf{C}\mathbf{B}_{a\partial z} dA
\end{aligned} \tag{2.40}$$

$$\mathbf{W} = \begin{bmatrix}\bar{\mathbf{K}} & \hat{\mathbf{R}}^T & \tilde{\mathbf{R}}^T \\ \vdots & \hat{\mathbf{K}} & \hat{\mathbf{H}} \\ \text{sym.} & \cdots & \tilde{\mathbf{K}}\end{bmatrix} \tag{2.41}$$

Focusing on the external work and introducing the displacement of Eq. (2.37), Eq. (2.32) becomes Eq. (2.42).

$$\delta\mathcal{W}_{ext} = \int_A (\delta\mathbf{s}^T\mathbf{p})_{\partial z} dA = \int_A (\delta\mathbf{a}^T\mathbf{N}^T\mathbf{p} + \delta\mathbf{r}^T\mathbf{Z}^T\mathbf{p})_{\partial z} dA \tag{2.42}$$

The first term of Eq. (2.42) becomes Eq. (2.43) and the second one becomes Eq. (2.44).

$$\delta\mathbf{a}_{\partial z}^T\mathbf{P} + \delta\mathbf{a}^T\mathbf{P}_{\partial z} \tag{2.43}$$

$$(\delta\mathbf{r}^T\boldsymbol{\theta})_{\partial z} \tag{2.44}$$

The external work becomes Eq. (2.45) and using Eq. (2.27) it becomes Eq. (2.46), where the z derivative of the $\delta\mathbf{r}$ term has been removed .

$$\delta\mathcal{W}_{ext} = \delta\mathbf{a}_{\partial z}^T\mathbf{P} + \delta\mathbf{a}^T\mathbf{P}_{\partial z} + \delta\mathbf{r}^T\boldsymbol{\theta}_{\partial z} + \delta\mathbf{r}_{\partial z}^T\boldsymbol{\theta} \tag{2.45}$$

$$\delta\mathcal{W}_{ext} = \delta\mathbf{a}_{\partial z}^T\mathbf{P} + \delta\mathbf{a}^T\mathbf{P}_{\partial z} + \delta\mathbf{r}^T(\boldsymbol{\theta}_{\partial z} - \mathbf{T}^T\boldsymbol{\theta}) + \delta\boldsymbol{\Psi}^T\boldsymbol{\theta} \tag{2.46}$$

Finally, in matrix form the V.W.P. becomes Eq. (2.47).

$$\begin{bmatrix} \delta\boldsymbol{\Psi} \\ \delta\mathbf{a} \\ \delta\mathbf{a}_{\partial z} \\ \delta\mathbf{r} \end{bmatrix}^T \left(\begin{bmatrix} \bar{\mathbf{K}} & \hat{\mathbf{R}}^T & \tilde{\mathbf{R}}^T & 0 \\ \vdots & \hat{\mathbf{K}} & \hat{\mathbf{H}} & 0 \\ \text{sym.} & \cdots & \tilde{\mathbf{K}} & 0 \\ 0 & 0 & 0 & 0 \end{bmatrix} \begin{bmatrix} \boldsymbol{\Psi} \\ \mathbf{a} \\ \mathbf{a}_{\partial z} \\ \mathbf{r} \end{bmatrix} - \begin{bmatrix} \boldsymbol{\theta} \\ \mathbf{P}_{\partial z} \\ \mathbf{P} \\ \boldsymbol{\theta}_{\partial z} - \mathbf{T}^T\boldsymbol{\theta} \end{bmatrix} \right) = \mathbf{0} \tag{2.47}$$

By imposing the arbitrariness of virtual displacement, two sets of equations are derived. First case of Eq. (2.48) is the known differential property of internal load expressed by Eq. (2.49) and it is obtained imposing a unit displacement of the reference beam line while other terms are null. The second set of equation is obtained for null beam origin motion and unit warping, warping derivative and generalized strain parameter. This set describes the governing equations which must be solved to obtain the generalized strains and the warping.

$$\begin{cases} \boldsymbol{\theta}_{\partial z} - \mathbf{T}^T\boldsymbol{\theta} = \mathbf{0} & \delta\mathbf{r} = 1, \delta\mathbf{a} = \delta\mathbf{a}_{\partial z} = \delta\boldsymbol{\Psi} = \mathbf{0} \\ \begin{bmatrix} \bar{\mathbf{K}} & \hat{\mathbf{R}}^T & \tilde{\mathbf{R}}^T \\ \vdots & \hat{\mathbf{K}} & \hat{\mathbf{H}} \\ \text{sym.} & \cdots & \tilde{\mathbf{K}} \end{bmatrix} \begin{bmatrix} \boldsymbol{\Psi} \\ \mathbf{a} \\ \mathbf{a}_{\partial z} \end{bmatrix} = \begin{bmatrix} \boldsymbol{\theta} \\ \mathbf{P}_{\partial z} \\ \mathbf{P} \end{bmatrix} & \delta\mathbf{r} = 0, \delta\mathbf{a} = \delta\mathbf{a}_{\partial z} = \delta\boldsymbol{\Psi} = \mathbf{1} \end{cases} \tag{2.48}$$

$$\begin{aligned} \tfrac{\partial M_x}{\partial z} &= T_y \\ \tfrac{\partial M_y}{\partial z} &= -T_x \end{aligned} \tag{2.49}$$

Considering the first case of Eq. (2.48) and defining the loads acting on $z = 0$ section as $\boldsymbol{\theta}_0$, it is possible to assume the linear variation of the load distribution of Eq. (2.50) in the proximity of $z = 0$. $\mathbf{T}$ accounts for the bending moments increase due to the shear forces.

$$\begin{cases} \boldsymbol{\theta}_0 = \boldsymbol{\theta}(z = 0) \\ \boldsymbol{\theta}(z) = (\mathbf{I} + z\mathbf{T}^T)\boldsymbol{\theta}_0 \end{cases} \tag{2.50}$$

According to Eq. (2.50), a linear behaviour can be assumed for the unknowns as in Eq. (2.51) .

$$\begin{cases} \boldsymbol{a}(z) = (\mathbf{A}_0 + z\mathbf{A}_1)\boldsymbol{\theta}_0 \\ \boldsymbol{P}(z) = (\mathbf{P}_0 + z\mathbf{P}_1)\boldsymbol{\theta}_0 \\ \boldsymbol{\Psi}(z) = (\boldsymbol{\Psi}_0 + z\boldsymbol{\Psi}_1)\boldsymbol{\theta}_0 \end{cases} \tag{2.51}$$

The unknowns behaviour of Eq. (2.51) leads to Eq. (2.52), which must be solved for arbitrary z and leads to the two set of linear system of Eq. (2.53).

$$\left(\begin{bmatrix} \bar{\mathbf{K}} & \hat{\mathbf{R}}^T & \tilde{\mathbf{K}}^T \\ \vdots & \hat{\mathbf{K}} & \hat{\mathbf{H}} \\ \text{sym.} & \cdots & \tilde{\mathbf{K}} \end{bmatrix} \begin{bmatrix} \boldsymbol{\Psi}_0 + z\boldsymbol{\Psi}_1 \\ \mathbf{A}_0 + z\mathbf{A}_1 \\ \mathbf{A}_1 \end{bmatrix} = \begin{bmatrix} \mathbf{I} + z\mathbf{T}^T \\ \mathbf{P}_1 \\ \mathbf{P}_0 + z\mathbf{P}_1 \end{bmatrix} \right) \boldsymbol{\theta}_0 \tag{2.52}$$

$$\begin{cases} \begin{bmatrix} \bar{\mathbf{K}} & \hat{\mathbf{R}}^T & \tilde{\mathbf{K}}^T \\ \vdots & \hat{\mathbf{K}} & \hat{\mathbf{H}} \\ \text{sym.} & \cdots & \tilde{\mathbf{K}} \end{bmatrix} \begin{bmatrix} \boldsymbol{\Psi}_1 \\ \mathbf{A}_1 \\ 0 \end{bmatrix} = \begin{bmatrix} \mathbf{T}^T \\ 0 \\ \mathbf{P}_1 \end{bmatrix} & \forall z \\ \begin{bmatrix} \bar{\mathbf{K}} & \hat{\mathbf{R}}^T & \tilde{\mathbf{K}}^T \\ \vdots & \hat{\mathbf{K}} & \hat{\mathbf{H}} \\ \text{sym.} & \cdots & \tilde{\mathbf{K}} \end{bmatrix} \begin{bmatrix} \boldsymbol{\Psi}_0 \\ \mathbf{A}_0 \\ \mathbf{A}_1 \end{bmatrix} = \begin{bmatrix} \mathbf{I} \\ \mathbf{P}_1 \\ \mathbf{P}_0 \end{bmatrix} & z = 0 \end{cases} \tag{2.53}$$

By solving first equations set of Eq. (2.53) and feeding $\boldsymbol{\Psi}_1, \mathbf{A}_1$ and $\mathbf{P}_1$ in the second equation set, the problem is fully solved. Recalling Eq. (2.38) the strains for unit internal loads are known and become Eq. (2.54).

$$\boldsymbol{\varepsilon} = \left(\mathbf{B}_\Psi \boldsymbol{\Psi}_0 + \mathbf{B}_a \mathbf{A}_0 + \mathbf{B}_{a\partial z} \mathbf{A}_1\right) \boldsymbol{\theta}_0 \tag{2.54}$$

It is possible to identify the cross section stiffness (or compliance) matrix as a link between the generalized strains parameter and the internal load as in Eq. (2.55).

$$\mathcal{W}_{ext} = \delta\boldsymbol{\theta}_0^T \boldsymbol{\Psi}_0 = \delta\boldsymbol{\theta}_0^T \mathbf{K}_{sec}^{-1} \boldsymbol{\theta}_0 = \delta\boldsymbol{\Psi}_0^T \mathbf{K}_{sec} \boldsymbol{\Psi}_0 \tag{2.55}$$

Recalling Eq. (2.46) and substituting the solution of the Eq. (2.52), the external virtual work can be rewritten as Eq. (2.56), hence the stiffness matrix becomes Eq. (2.57).

$$\mathcal{W}_{ext} = \delta\boldsymbol{\theta}_0^T (\mathbf{A}_1^T \mathbf{P}_0 + \mathbf{A}_0^T \mathbf{P}_1 + \boldsymbol{\Psi}_0^T) \boldsymbol{\theta}_0 = \delta\boldsymbol{\theta}_0^T \mathbf{K}_{sec}^{-1} \boldsymbol{\theta}_0 \tag{2.56}$$

$$\mathbf{K}_{sec} = (\mathbf{A}_1^T \mathbf{P}_0 + \mathbf{A}_0^T \mathbf{P}_1 + \boldsymbol{\Psi}_0^T)^{-1} \tag{2.57}$$

The formulation proposed shows how it is possible to obtain cross section stress distribution and stiffness matrix for a generic 2D problem. When considering a wingbox, it is possible to do some assumption to simplify the problem. For example it is assumed that spar webs and skins are subjected to a stress state where the two components are axial stress and transverse shear, while the stringers and spar caps withstand only axial stress. Moreover, the warping has only the out of plane component. Thanks to this two hypotheses the wingbox is described with just two type of element.
The first element type is a flat panel used to represent skins and webs, the second type is an area element used for stringers representation. The following sections re-formulates the problem for this two elements.

Isoparametric panel element

The panel element's formulation is based on the kinematics illustrated in Fig. 2.18. For sake of simplicity, only 2 nodes panel are described hereafter, but the formulation can exploit higher order shape function.
The local coordinate system $(\bar{\mathbf{x}}, \bar{\mathbf{y}})$ is defined by two unit orthogonal vectors

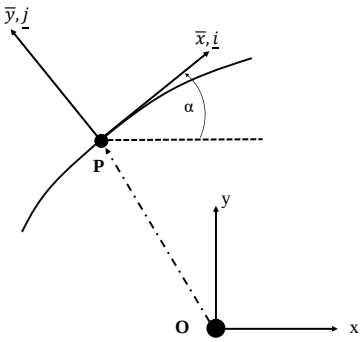

Figure 2.18: *Kinematics of the panel element*

$\underline{\mathbf{i}}, \underline{\mathbf{j}}$:

$$\underline{\mathbf{i}} = \begin{bmatrix} i_x \\ i_y \end{bmatrix} = \begin{bmatrix} \cos\alpha \\ \sin\alpha \end{bmatrix} \text{ and } \underline{\mathbf{j}} = \begin{bmatrix} j_x \\ j_y \end{bmatrix} = \begin{bmatrix} -\sin\alpha \\ \cos\alpha \end{bmatrix} \tag{2.58}$$

The panel element is described by the line connecting the two end points (X_k, Y_k) with $k = 1 : 2$. The coordinates of a generic point along the

connecting line are provided by Eq. (2.59):

$$\begin{cases} x = \sum_{k=1}^{2} N_k X_k \\ y = \sum_{k=1}^{2} N_k Y_k \end{cases} \tag{2.59}$$

Where $\mathbf{N}$ are the linear shape function.

$$\mathbf{N} = \frac{1}{2}\begin{bmatrix} -1 & 1 \\ 1 & 1 \end{bmatrix}\begin{bmatrix} \lambda \\ 1 \end{bmatrix} \text{ with } \lambda \in [-1, 1] \tag{2.60}$$

And in matrix form:

$$\begin{bmatrix} x \\ y \end{bmatrix} = \begin{bmatrix} \mathbf{N}^T & 0 \\ 0 & \mathbf{N}^T \end{bmatrix}\begin{bmatrix} \mathbf{X} \\ \mathbf{Y} \end{bmatrix} \tag{2.61}$$

It is possible to use the same shape function of Eq (2.60) to approximate the warping field.

$$g = \mathbf{N}^T \mathbf{a} \tag{2.62}$$

The plate elements account for σ_z and $\tau_{\bar{x}z}$ stresses, recalling Eq. (2.11) we can write the following expression for the strain-stress relation specified for a reduced stress state:

$$\bar{\boldsymbol{\sigma}} = \mathbf{C}\bar{\boldsymbol{\varepsilon}} \text{ where } \bar{\boldsymbol{\sigma}} = \begin{bmatrix} \sigma_x \\ \tau_{\bar{x}z} \end{bmatrix} \text{ and } \bar{\boldsymbol{\varepsilon}} = \begin{bmatrix} \varepsilon_x \\ \gamma_{\bar{x}z} \end{bmatrix} \tag{2.63}$$

The equivalent of Eq. (2.38) in a $(\bar{x}, \bar{y})$ coordinate system becomes:

$$\bar{\boldsymbol{\varepsilon}} = \hat{\mathbf{D}}\mathbf{N}\mathbf{a} + \hat{\mathbf{S}}\mathbf{N}\mathbf{a}_{\partial z} + \hat{\mathbf{Z}}\hat{\boldsymbol{\Psi}} \tag{2.64}$$

With

$$\begin{gathered} \hat{\mathbf{D}} = \begin{bmatrix} 0 & 0 & 0 \\ 0 & 0 & \frac{\partial}{\partial \bar{x}} \end{bmatrix} \\ \hat{\mathbf{S}} = \begin{bmatrix} 0 & 0 & 1 \\ 1 & 0 & 0 \end{bmatrix} \\ \hat{\mathbf{Z}} = \begin{bmatrix} 0 & 0 & 1 & (\mathbf{P}-\mathbf{O})\underline{\mathbf{j}} & -(\mathbf{P}-\mathbf{0})\underline{\mathbf{i}} & 0 \\ 1 & 0 & 0 & 0 & 0 & -(\mathbf{P}-\mathbf{0})\underline{\mathbf{j}} \end{bmatrix} \end{gathered} \tag{2.65}$$

$$\begin{gathered} \varepsilon_z = \frac{\partial}{\partial z}(\mathbf{N}\mathbf{a}) + \hat{\mathbf{Z}}_1\hat{\boldsymbol{\Psi}} \\ \gamma_{\bar{x}z} = \frac{\partial}{\partial \bar{x}}(\mathbf{N}\mathbf{a}) + \mathbf{N}\mathbf{a}_{\bar{x}\partial z} + \hat{\mathbf{Z}}_2\hat{\boldsymbol{\Psi}} \end{gathered} \tag{2.66}$$

$\mathbf{N}\mathbf{a}_{\bar{x}\partial z}$ is neglected because is small with respect the others terms.

$$\bar{\boldsymbol{\varepsilon}} = \bar{\mathbf{D}}\mathbf{N}\mathbf{a}_z + \bar{\mathbf{S}}\mathbf{N}\mathbf{a}_{z\partial z} + \hat{\mathbf{Z}}\hat{\boldsymbol{\Psi}} \tag{2.67}$$

With

$$\bar{\mathbf{D}} = \begin{bmatrix} 0 \\ \frac{\partial}{\partial \bar{x}} \end{bmatrix} \quad \text{and} \quad \bar{\mathbf{S}} = \begin{bmatrix} 1 \\ 0 \end{bmatrix} \tag{2.68}$$

In local coordinate system, generalized strain parameters comes from:

$$\bar{\mathbf{\Psi}} = \bar{\mathbf{T}}\mathbf{\Psi} \tag{2.69}$$

Where

$$\bar{\mathbf{T}} = \begin{bmatrix} \cos\alpha & \sin\alpha & 0 & & & \\ -\sin\alpha & \cos\alpha & 0 & & 0_{3x3} & \\ 0 & 0 & 1 & & & \\ & & & \cos\alpha & \sin\alpha & 0 \\ & 0_{3x3} & & -\sin\alpha & \cos\alpha & 0 \\ & & & 0 & 0 & 1 \end{bmatrix} \tag{2.70}$$

It is possible to derive $\mathbf{Z} = \bar{\mathbf{Z}}\bar{\mathbf{T}}$

$$\mathbf{Z} = \begin{bmatrix} 0 & 0 & 1 & y & -x & 0 \\ \cos\alpha & \sin\alpha & 0 & 0 & 0 & x\sin\alpha - y\cos\alpha \end{bmatrix} \tag{2.71}$$

$$\bar{\boldsymbol{\varepsilon}} = \bar{\mathbf{D}}\mathbf{N}\mathbf{a}_z + \bar{\mathbf{S}}\mathbf{N}\mathbf{a}_{z\partial z} + \mathbf{Z}\mathbf{\Psi} \tag{2.72}$$

Strain components are

$$\begin{gathered} \varepsilon_z = \mathbf{N}\mathbf{a}_{z\partial z} + w_{0\partial z} + y\alpha_{0\partial z} - x\beta_{0\partial z} \\ \gamma_{\bar{x}z} = \mathbf{N}\mathbf{a}_{z\partial\bar{x}} + i_x(u_{0\partial z} - \beta_0) + i_y(v_{0\partial z} + \alpha_0) + \gamma_{0\partial z}(xi_y - yi_x) \end{gathered} \tag{2.73}$$

$$\bar{\mathbf{B}} = \begin{bmatrix} 0 & 0 \\ \frac{\partial N_1}{\partial \bar{x}} & \frac{\partial N_2}{\partial \bar{x}} \end{bmatrix} \tag{2.74}$$

The element has constant thickness, hence the area integral becomes a line integral along $\bar{x}$, for convenience the integral is performed along a non dimensional coordinate $\lambda \in [-1, 1]$. For the linear shape function employed, the Jacobian is equal to half the panel length, hence $d\bar{x} = \frac{\mathcal{L}}{2}d\lambda$. Following the scheme of Eq. (2.40) it is possible to find $\hat{\mathbf{K}}, \bar{\mathbf{K}}, \tilde{\mathbf{K}}, \hat{\mathbf{R}}, \tilde{\mathbf{R}}, \hat{\mathbf{H}}$ and assemble the elemental matrices.

Stringer

Following the same formulation adopted for the panel element, it is possible to manage the stringer element. It is represented with a point with coordinates X, Y. The unique stress component is the normal axial stress

σ_z, which is proportional to the axial strain through the elastic modulus $\sigma_z = E\varepsilon_z$. For this element the axial strain is:

$$\varepsilon_z = \frac{\partial a}{\partial z} + \hat{\mathbf{Z}}_1 \hat{\mathbf{\Psi}} \tag{2.75}$$

The shape functions are not needed for this element.

$$\varepsilon_z = a_{z\partial z} + w_{0\partial z} + y\alpha_{0\partial z} - x\beta_{0\partial z} \tag{2.76}$$

In this case the $\hat{\mathbf{B}}$ matrix is null and the constitutive law is simply the Young's modulus. Since $\hat{\mathbf{B}}$ is null, $\hat{\mathbf{K}}, \hat{\mathbf{R}}, \hat{\mathbf{H}}$ are identically null. The integral on the area is unnecessary for this kind of element.

Using the two elements above described, the number of unknown for the problem is equal to the number of nodes because it is accounted the only out of plane warping component g_z. The elemental matrices are assembled following common FE techniques, and then assembled into the global problem matrices.
The solution of Eq. (2.53) is done in two step, both of them requires the inversion of:

$$\mathcal{X} = \begin{bmatrix} \bar{\mathbf{K}} & \hat{\mathbf{R}}^T \\ \hat{\mathbf{R}} & \hat{\mathbf{K}} \end{bmatrix} \tag{2.77}$$

Following the formulation adopted, $\mathcal{X}$ is three times rank deficient. This is due to the section's rigid body motion that can be described by the out plane warping. The motions are a section translation along **z** axis and the rotations around **x** and **y** axes. To solve this singularity, two ways are available. The first one is constraining isostatically the problem by removing row and columns of prescribed degrees of freedom, the second one is the adoption of Lagrange's multiplier. NeoANBA implements the last one.

2.4.2 NeoANBA Validation

This section shows some test cases used to validate the model implemented in the previous section. The main aspects which need to be verified are:

- The correct evaluation of the cross section stiffness and mass matrices
- The correct recovery of the cross sectional stresses with respect to known analytical solution
- The behaviour of a stick model with respect to a higher fidelity 3D FEM model in terms of displacement and stress distribution obtained

through the meta-model. This must be checked both for isotropic and orthotropic materials

In the next sections several test cases are reported to validated NeoANBA.

Cross section model validation

The first validation case is a rectangular cross section with 6 stringers, shown in Fig. 2.19. The thickness of the skins is $2mm$ and the area of the stringer is $800mm^2$.

Tab. 2.1 compares the analytical and numerical values for stiffness and

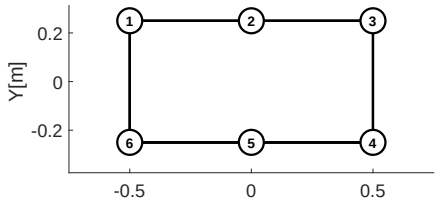

Figure 2.19: *Rectangular cross section*

mass terms. The error is low $(err \leq 10^{-4})$ for all the components.

A sensitivity test on the number of stringers shows in Fig. 2.20 that it does

Table 2.1: *Analytic vs. NeoANBA results. Cross section stiffness value and unit length mass properties.*

		Analytic	NeoANBA	Error [%]
EA	$[N]$	7.970e+08	7.970e+08	+0.000e+00 %
EJxx	$[Nm^2]$	4.367e+07	4.367e+07	-2.254e-05 %
EJyy	$[Nm^2]$	1.205e+08	1.205e+08	-4.082e-05 %
GJt	$[Nm^2]$	1.850e+07	1.850e+07	+0.000e+00 %
M	$[kg]$	1.080e-02	1.080e-02	+0.000e+00 %
Ixx	$[kgm^2]$	5.917e-04	5.917e-04	-3.054e-15 %
Iyy	$[kgm^2]$	1.633e-03	1.633e-03	-5.531e-16 %
Izz	$[kgm^2]$	2.225e-03	2.225e-03	-8.989e-05 %

not affect the quality of the results obtained with NeoANBA.

It is possible to recover stress distribution through analytic formulation and Fig. 2.21 shows that the stresses obtained with NeoANBA are equal to the analytical ones.

This two cases proves NeoANBA ability of computing correct structural properties and stress distribution for an isotropic section.

Since an analytical formulation for the evaluation of the coupling terms introduced by orthotropic materials is not available, this test is demanded to the

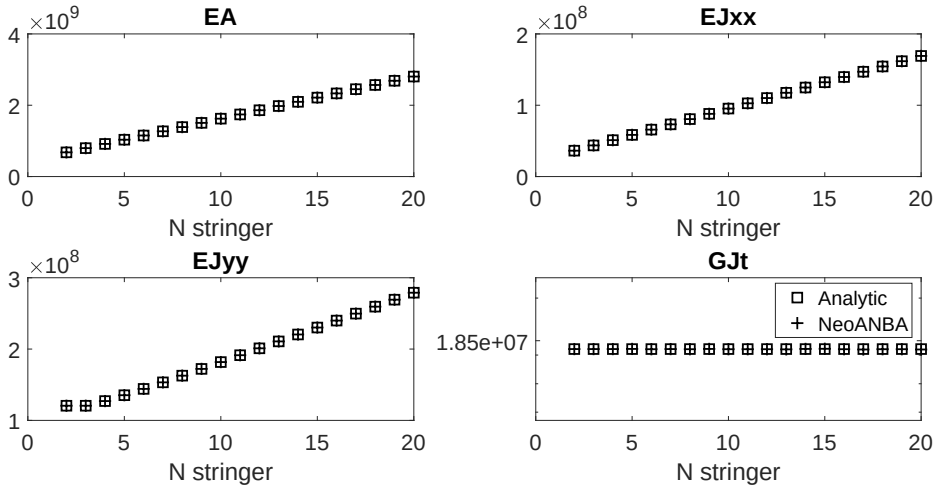

Figure 2.20: *Stiffness properties varying stringer number*

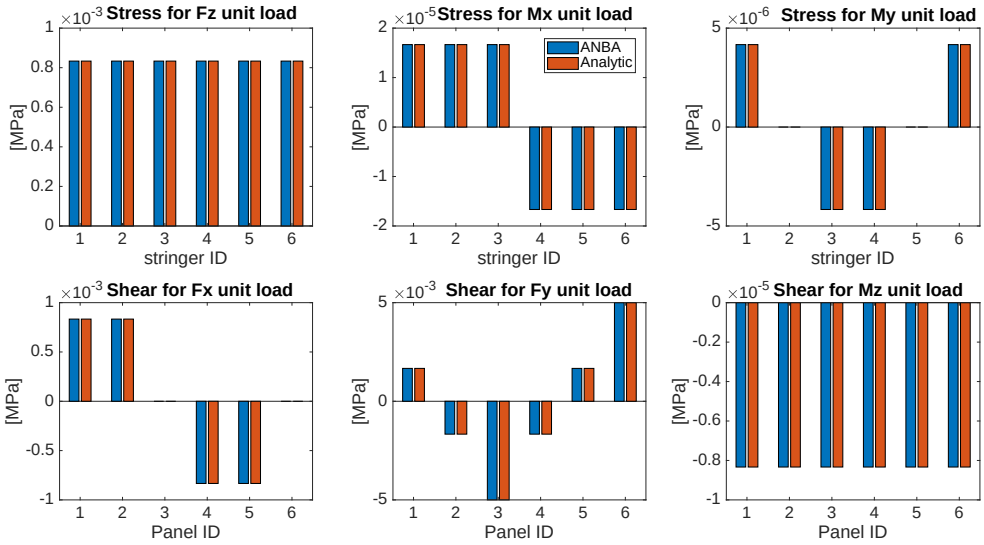

Figure 2.21: *Comparison between analytical and NeoANBA stress*

next section where the comparison between the stick and 3D FEM model is performed.

Stick model validation

NeoANBA is validated at cross section level, in this paragraph the properties obtained with NeoANBA are applied to the stick model in terms of beam stiffness matrices. Thanks to the meta-model, it is available the 3D FEM of the same wingbox, the two models are loaded with the same conditions. The stress distributions and the displacements obtained for the two models are then compared.
The aim of this section is to show that the improved stick model is able to approximate the solution obtained with an higher fidelity model like a 3D shell elements FEM of the same wingbox, both in term of displacement and stress distribution.
The wingbox considered (Fig. 2.22) is is 4.62m x 0.923m x 29.82m with 25 equally spaced stringers for upper and lower skins. It comes from a NeoCASS model of a dummy aircraft and it is made of aluminium. The reference system has the **x** axis in chordwise direction and the **y** axis in spanwise direction.
The meta-model creates the 2D mesh of the wingbox cross section where

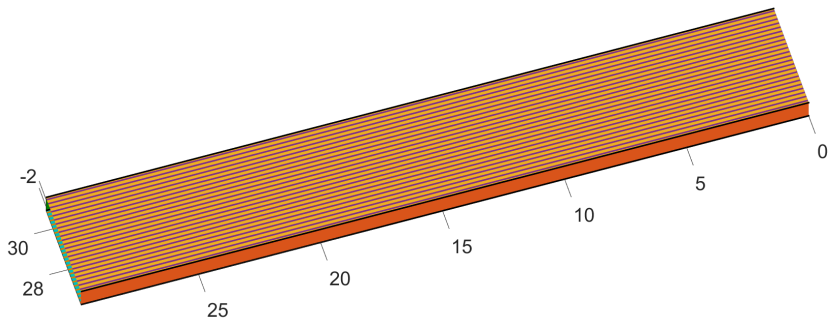

Figure 2.22: *Rectangular Wing Box*

a rib is present and NeoANBA computes the structural matrices which are transferred to the stick model. Fig. 2.23 compares the displacements obtained with the stick and 3D models under tip loading. First two images (2.23a and 2.23b) compares the z displacement and x rotation for a z oriented tip load (out of plane bending), while 2.23c represents the y rotation for a tip torsional moment.
For both cases, the displacements and rotations obtained with the stick model are equal to the one obtained with the 3D model, proving that the stiffness properties are well identified and transferred to the stick model.

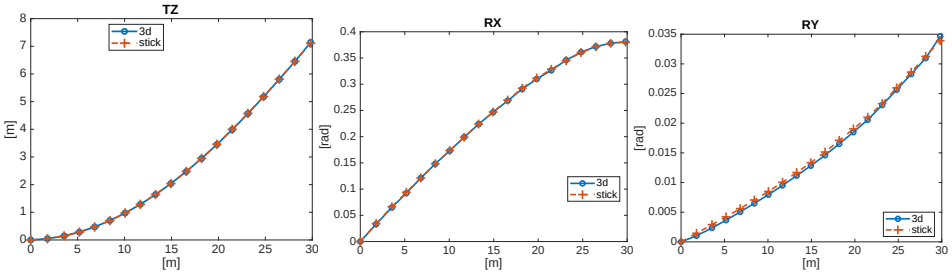

(a) *z diplacement, z force* **(b)** *x rotation, z force* **(c)** *y rotation, y moment*

Figure 2.23: *Stick vs. 3D model deformed shapes*

Fig. 2.24 shows the stress pattern obtained with a vertical (**z** direction) tip load (out of plane bending). Since NeoANBA consider only axial stress and transverse shear, it is possible to compare this stress pattern with the one obtained with the full 3D model. Von Mises's stress is compared as well, but the one obtained with Nastran accounts for all the stress computed with a SHELL element while NeoANBA considers only the ones available in the model (axial and transverse shear).

Some differences are present in the constraint and load introduction area, this are local effects which can not be catch with NeoANBA. In the region not affected by local phenomena, the stress distribution obtained with the two models is very similar, NeoANBA slightly overestimates the stress values, which is in favour of safety and desirable during preliminary design phase. The global stress pattern is well identified with a satisfactory correlation level.

To verify that NeoANBA correctly represents non homogeneous wingbox, the isotropic model of the previous example is converted into a composite wingbox. The top and bottom skins are made of unidirectional CFRP with an orientation of 30° with respect to the beam axis. The lamination scheme is shown in Fig. 2.25 and generates a bending-torsion coupling. In this case it is important to correctly evaluate the coupling terms, which means check the displacement component that are not in the same direction of the applied force. In this case the parameters to be investigated are the torsional rotation generated by a vertical force and the vertical displacement generated by a torsional moment.

Fig. 2.26 shows the comparison between 3D FEM and stick model displacement due to a vertical (**z** direction) force. In particular, Fig. 2.26c shows the bending-torsion coupling, where a vertical load generates a rotation around

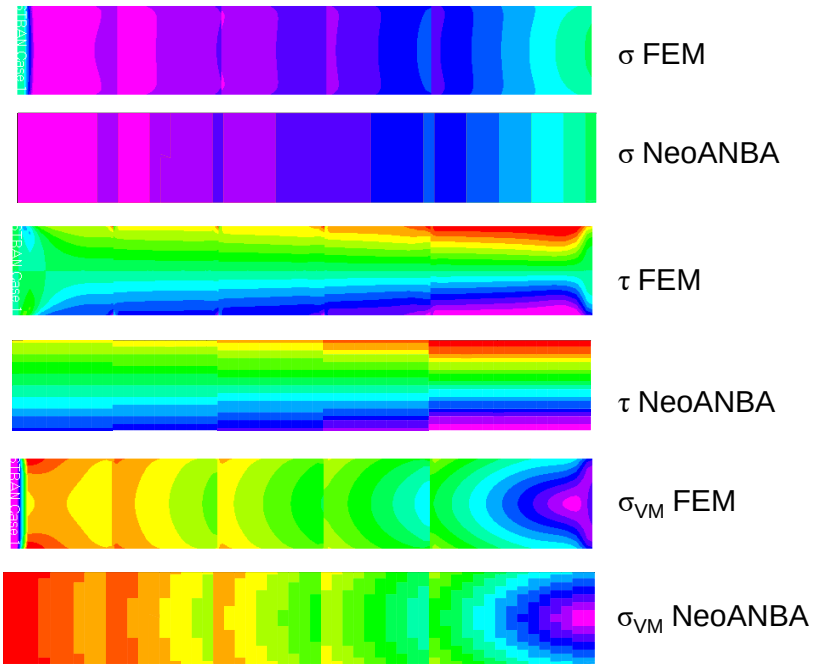

Figure 2.24: *Isotropic wingbox stress distribution, z force. Stress scale is equal for both cases.*

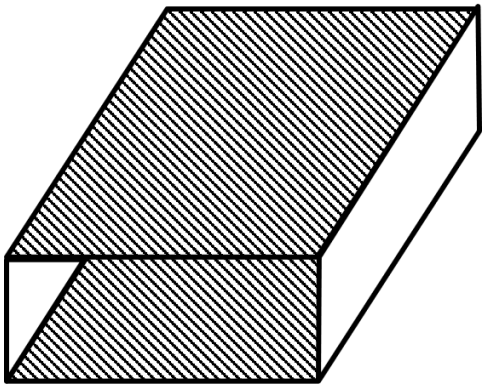

Figure 2.25: *Wingbox with symmetric upper and lower panel*

the beam axis (**y** axis). The main difference for the y rotation at the root (y=0m) is due to the constraints applied to the 3D FEM model which limits the coupling term. The opposite phenomena appears at the end (y=30m) where the coupling effect is overestimated where the load is applied.

The first local effect introduces an offset between the two curves which is constant spanwise (far away from constraints and loads), this means that far from the constraint the coupling term is well evaluated. The z displacement and x rotation are perfectly matched as shown for the isotropic wingbox.
The same comparison is performed applying a torsional moment and com-

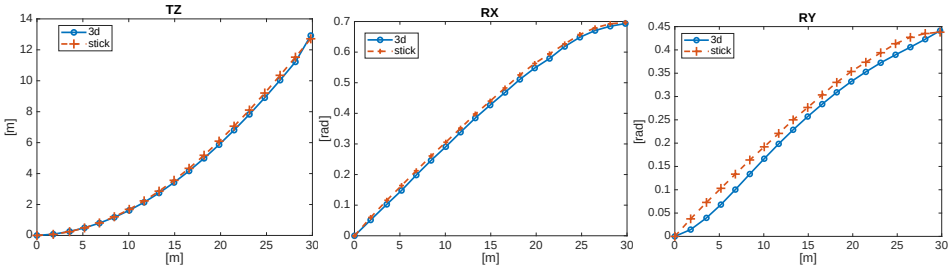

(a) *z diplacement, z force* **(b)** *x rotation, z force* **(c)** *y rotation, z force*

Figure 2.26: *Stick vs. 3D model deformed shapes, orthotropic wingbox, z force*

paring the same displacement components (2.27a). In this case the stick model z displacement(Fig 2.27a) and x rotation (Fig 2.27b) match the result of the 3D FEM.
The last two test cases showed the correct evaluation of the bending-torsion

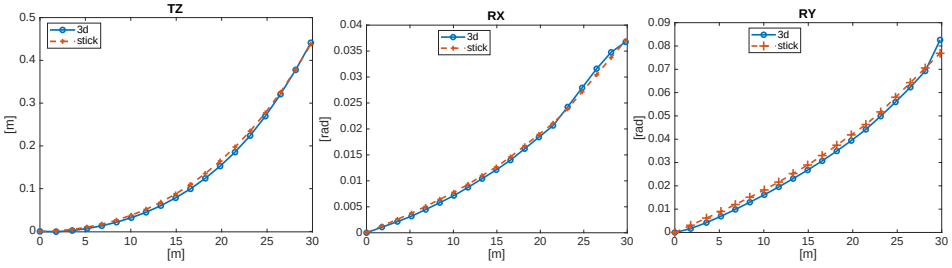

(a) *z diplacement, y monment* **(b)** *x rotation, y moment* **(c)** *y rotation, y moment*

Figure 2.27: *Stick vs. 3D model deformed shapes, orthotropic wingbox, y moment*

coupling term.
The comparison in Fig. 2.28 shows how the stress pattern obtained for the composite wingbox with NeoANBA is simalr to the one obtained with the 3D FEM model, in this case material discontinuities across the patches and boundary effects are more marked in the 3D FEM model and are missed by NeoANBA.
The tests performed on the 3D model show that the stiffness properties are evaluated and transferred correctly between the 3D model and the stick

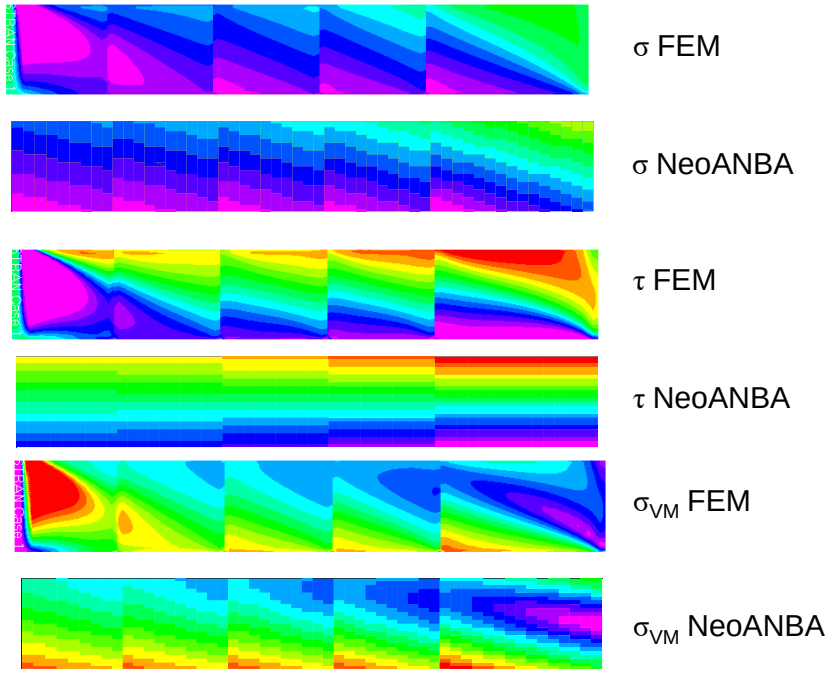

Figure 2.28: *Composite wingbox stress distribution, z force. Stress scale is equal for bot cases.*

model, catching in a proper way the coupling terms introduced with the composites skins. The stresses are recovered in a satisfactory way both for isotropic and composite wingboxes.

Concluding remarks on NeoANBA

This section illustrated the theory behind NeoANBA and its numerical implementation. Several test cases prove that the section modeller is able to correctly estimate cross section stiffness and mass matrices, transferring these properties into the stick model through the meta-model. The cross section stress state obtained with NeoANBA and expanded in 3D with the meta-model is similar to the one obtained with the 3D FEM. Some differences appears when considering the boundary effects but the general behaviour is well estimated.
NeoANBA has some limitation, for example it works with stick model which considers the rib as infinitely stiff. The stress components modelled are only

transverse shear and axial stress while 3D plate element considers the full stress tensor.
It must be considered that stick model results are obtained on a small beam model (15-30 elements) while the detailed model has more than 20000 elements, the stress evaluation obtained with the proposed procedure provides an indication of the stress distribution in preliminary design phases and it do not aim to substitute the 3D FEM for detailed stress analysis of next design phases.
The correct evaluation of the coupling terms allows to consider composite materials in the stick-model, which remains the reference model for aero-servo-elastic load envelope computation and flutter estimation. This increases the fidelity of the model adopted in the early design phases.

2.4.3 Concluding remarks on the wingbox description

This chapter showed how the fidelity of the model is increased without modification to the topology of the element employed. The meta-model plays a central role in this phase opening the possibilities of dealing with different but coherent models. The automatic generation of 3D CAD and FEM model speeds up the design process by providing ready to use models for the next design steps. The beam structural model is now able to manage whichever orthotropic hollow section providing the full stiffness matrix of the beam element and opening the possibility of consider the composite materials since the conceptual design phases.

CHAPTER 3

Active controls for load alleviation and flutter suppression

There is a long tradition of applications of active control technologies on aircraft for several purposes, with an increasing interest in the last years driven by lightweight structures, by the evolution of digital computers and by the improved performance of actuation systems.
Since the end of the World War II many studies and application of active control technologies can be found: [44] provides a survey of the experimental tests on active load controllers and their applications, while [17] is a sort of encyclopedic collection of the activity done on the active flutter suppression.
The structural efficiency improvement through active control is known since the 50', an example is the Bristol Brabazon that was designed with a structure 20% weaker than necessary thanks to the designer's faith in the gust alleviation feed-forward controller [45].
The interaction of the control system with aeroelastic model plays a relevant role in dynamic load computation, in the last years several methodologies were developed in academia and industrial environment for this purpose. One of them is presented in [46] and used as standard tool for aero-servo-

elastic load computation by Airbus Defence and Space.
Potential mass saving must be evaluated since the early design phases to optimize simultaneously the structure and the controller, for this reason a simple but effective methodology to design and tune the controller is needed. This chapter presents an user friendly control design process which can be easily automated and included in an optimization loop to control the dynamic load and dynamic instability.
The aim is to establish a simple and fast procedure for the preliminary design of the active control law, suitable to be embedded in the NeoCASS aero-servo-elastic simulation tool to assess its impact on the dynamic behaviour (load and stability) of the aircraft. It is not intended to compare the performance of the designed controller with other more sophisticated and performant control design methodologies.
During the doctoral research program there was the occasion of being involved in two projects: the AIRGREEN2 (AG2) and the Active Flutter Suppression (AFS) project. Both of them will be presented after the discussion of the numerical method for control law design and despite they do not directly exploit NeoCASS, they allowed to validate the proposed methodology. In the AG2 project, a NeoCASS-ready model of a regional transportation aircraft is used as a platform for the evaluation of Gust and Manoeuvre Load Alleviation techniques, hence only the development of control laws is performed. In the second project, AFS, the focus once again was on the development of active control strategy for the flutter suppression of a wind tunnel model and also in this case the experiment is used to validate the control law design approach.

3.1 Controller design

NeoCASS uses the doublet-lattice method for the evaluation of the unsteady aerodynamic forces, this method computes the aerodynamic matrices for a user-provided set of reduced frequencies and Mach number. Typically the problem is solved in frequency domain and then it is transformed in the time domain through the inverse Fourier transform. Among its features, NeoCASS implement a tool for the identification of the aerodynamic transfers function [33, 47] which allows to re-write the aeroelastic problem in the time-domain, creating a State-Space model of the aircraft. This procedure allows to realize an aero-servo-elastic model which can be simulated in time domain. This kind of modelling is suitable to develop and investigate active control laws for load reduction and stability augmentation like manoeuvre

load alleviation (MLA), gust load alleviation (GLA) and active flutter suppression (AFS). The active reduction of the static and dynamic load can lead to a reduction of the design load and a possible improvement of the structural mass.
The aim of the active control in this phase is to investigate if it can be beneficial to the wing design, reducing the load envelope and to evaluate its impact on the final structural configuration. In few words, the implementation of active controls in this stage is more devoted to the trade-off studies on the impact of the dynamic loads on the aero structural design. Control laws detailed design and verification is demanded to later stages.
Many approach to the aero-servo-elastic control of the aircraft have been developed in aviation history, for the sake of continuity with the activities done at Politecnico of Milano Department of Aerospace Science and Technology and the wind tunnel activities performed during the doctoral programme, in this thesis only the Static Output Feedback (SOF) control architecture is considered [48].
The controller is synthesised using as control variable the deflection of the conventional control surfaces (aileron, elevator, rudder) and/or dedicated control surfaces, the feedback is provided by standard measures typically available on new generation aircraft like wing and centre of gravity accelerations and IMU data.
The system (aircraft) considered is a linear time-invariant (LTI) model, which representation is:

$$\begin{cases} \dot{\mathbf{x}} = \mathbf{A}\mathbf{x} + \mathbf{B_u}\mathbf{u} + \mathbf{B_d}\mathbf{d} \\ \mathbf{y} = \mathbf{C_y}\mathbf{x} + \mathbf{D_{yu}}\mathbf{u} + \mathbf{D_{yd}}\mathbf{d} \\ \mathbf{z} = \mathbf{C_z}\mathbf{x} + \mathbf{D_{zu}}\mathbf{u} + \mathbf{D_{zd}}\mathbf{d} \end{cases} \tag{3.1}$$

Where **x** is the state vector, **u** is the control vector and **d** is the disturbance. The control vector is the only way the user (controller) can modify the system, in the case of a control law for GLA/MLA/AFS it contains the surface command, while the disturbance is the gust impacting the aircraft or the continuous turbulence. Measurements **y** are the only quantities known in the real case, while **z** are the performances of system which are not available among the measure set and which are needed to evaluate the objective and constraints for the controller design. In the SOF architecture, the control input is a linear combination of the measures:

$$\mathbf{u} = -\hat{\mathbf{G}}\mathbf{y} \tag{3.2}$$

Using the expression of **y** in Eq.(3.1), the control input becomes:

$$\mathbf{u} = -(\mathbf{I} + \hat{\mathbf{G}}\mathbf{D_{yu}})^{-1}\hat{\mathbf{G}}(\mathbf{C_{yx}x} + \mathbf{D_{yd}d}) \tag{3.3}$$

By writing $\mathbf{G} = (\mathbf{I} + \hat{\mathbf{G}}\mathbf{D_{yu}})^{-1}\hat{\mathbf{G}}$, it is possible to obtain a control input which is linear in $\mathbf{G}$, and lead to the expression of the closed loop State-Space model:

$$\begin{cases} \dot{\mathbf{x}} = (\mathbf{A} - \mathbf{B_u}\mathbf{G}\mathbf{C_y})\mathbf{x} + (\mathbf{B_d} - \mathbf{B_u}\mathbf{G}\mathbf{D}\mathbf{y}\mathbf{d})\mathbf{d} \\ \mathbf{z} = (\mathbf{C_z} - \mathbf{D_u}\mathbf{G}\mathbf{C_y})\mathbf{x} + (\mathbf{D_{zd}} - \mathbf{D_{zu}}\mathbf{G}\mathbf{D}\mathbf{y}\mathbf{d})\mathbf{d} \\ \mathbf{u} = -\mathbf{G}\mathbf{C_y}\mathbf{x} - \mathbf{G}\mathbf{D_{yd}}\mathbf{d} \end{cases} \tag{3.4}$$

Using an overbar to indicate the closed loop matrix, the system is rewritten as:

$$\begin{cases} \dot{\mathbf{x}} = \bar{\mathbf{A}}\mathbf{x} + \bar{\mathbf{B}}_\mathbf{d}\mathbf{d} \\ \mathbf{z} = \bar{\mathbf{C}}_\mathbf{z}\mathbf{x} + \bar{\mathbf{D}}_\mathbf{zd}\mathbf{d} \\ \mathbf{u} = -\bar{\mathbf{C}}_\mathbf{y}\mathbf{x} - \bar{\mathbf{D}}_\mathbf{ud}\mathbf{d} \end{cases} \tag{3.5}$$

The unknown of the control problem is the gain matrix $\hat{\mathbf{G}}$, which is computed with a numerical procedure.
Many algorithms are available for the computation of $\hat{\mathbf{G}}$, like [49–54] and the method proposed in Fonte's MsC thesis [55, 56].
The methodology proposed in this section tries to minimize the closed loop time response of some performances of interest, satisfying stability and other constraints. The objective function is provided by Eq. 3.6 and can consider more than one performance with it own weight if required. Each i-th term of the summation is the ratio between the closed and open loop maximum absolute value.

$$f(x) = \sum_{i=1}^{n} w_i \frac{max(|z_i(x,t)|)}{max(|z_{i0}(x_0,t)|)} \tag{3.6}$$

Where $z_i(x)$ is the i-th closed-loop performance and $z_{i0}(x)$ is the i-th open-loop one. The mandatory constraints to be satisfied are the stability of the closed loop state matrix i.e. $\bar{\mathbf{A}}$ eigenvalues must have negative real part. The constraint is not imposed on the real part of the eigenvalue but on its damping ratio. In this way it is possible to guarantee sufficient damping to the aeroelastic modes by imposing the minimum value of damping acceptable.

$$\xi(\lambda_i) < \xi_{min} \leq 0 \tag{3.7}$$

Other constraints can be imposed to limit the control activity or to consider the actuator performance. The actuator transfer function can be easily included in the SS model, but in some case other actuator technological limits must be accounted in controller design. A typical one is the controller authority which limits the deflection available for active control purpose, or surface rotation rate which is limited by actuator performances.
The measure used as feedback can be whichever quantity directly measured on the aircraft e.g. accelerations or their elaboration e.g. integration of the acceleration to obtain the velocity.
The next sections show two different applications of the proposed methodology.

3.2 Gust Load Alleviation

Disclaimer

Some data of this section are covered by Non-Disclosure Agreement. For this reason sensitive data are non-dimensional and some others are intentionally omitted.

3.2.1 Project introduction

The Politecnico di Milano department of aerospace science and technology is actively involved in the Clean Sky 2 Green Regional Aircraft (GRA) Project [57]. The AIRGREEN2 consortium is composed by industries (Hellenic Aerospace Industry (HAI), SICAMB, Siemens Industry Software NV, FOXBIT, AEROSOFT, ITALSYSTEM, NOVOTECH, TECNAM, Umbra Cuscinetti), research centres (Centro Italiano Ricerche Aerospaziali (CIRA), Office national d'études et de recherches aérospatiales (ONERA)) and universities (Politecnico di Milano, Politecnico di Torino, Università degli Studi di Napoli "Federico II", Università di Pisa). The project is running since 2015 and aims to the investigation and technology readiness level improvement of a new electric wing equipped with innovative morphing devices for aerodynamic performances improvement and load alleviation. A morphing leading edge and a morphing flap are studied to substitute classical slat/flap solution to achieve better performance in take-off and landing phase, a morphing winglet is investigated to improve the cruise/climb aerodynamics performances and to perform manoeuvre load alleviation (quasi-static application) while an innovative wing tip (IWT) is designed to perform manoeuvre and gust load alleviation (MLA+GLA).

Polimi is the technical responsible of the Innovative Wing Tip concept which aims to be in-flight tested by the end of 2022. Two main design disciplines are involved: the aero-servo-structural project of the item and the design and validation of the control laws. Many control strategies were investigated during the project: several static output feedback (SOF) controllers for GLA/MLA [58] proposed by Politecnico di Milano and an H_∞ controller developed by the group led by E. Capello at Politecnico of Torino.
One of the SOF was realized with the methodology proposed in this chapter and it was tested with the aero-servo-elastic simulator of the aircraft and with an aeroelastic model in wind tunnel.
In the following it is presented the design of the SOF controller, its numerical validation and the comparison with the experimental data.
The aircraft investigated is a possible Next Generation 90 passengers turboprop (TP90 in fig 3.1), with an high trapezoidal wing, underwing mounted engines and a T-Tail.

Inside the work package devoted to the wingtip design and control law



Figure 3.1: *TP90 concept*

development, the activities were subdivided in the following macro-tasks:

- Wing tip device layout identification
- Control law development and integration in the numerical model
- Control law experimental test on a scaled aeroelastic model (WTT3)
- IWT ground demonstrator design and testing
- Control law application to the iron-bird
- Control law and IWT flight test on a flying test-bed (FTB1)

During the 7 year project the concept TRL has to mature and reach the authorization to the flight testing, producing an item which is ready to fly.

3.2.2 Gust Load Alleviation strategy development and validation

The first step was the identification of the most promising layout for the device. After a bibliographical review on the concept adopted in the past for alleviating or controlling the loads through conventional and unconventional movable surfaces [44, 58–78], a parametric optimization study was performed on the performances of the IWT. The design parameters are the ones illustrated in Fig. 3.2 and the optimal solution is identified in [58, 79], and is described by Tab. 3.1.

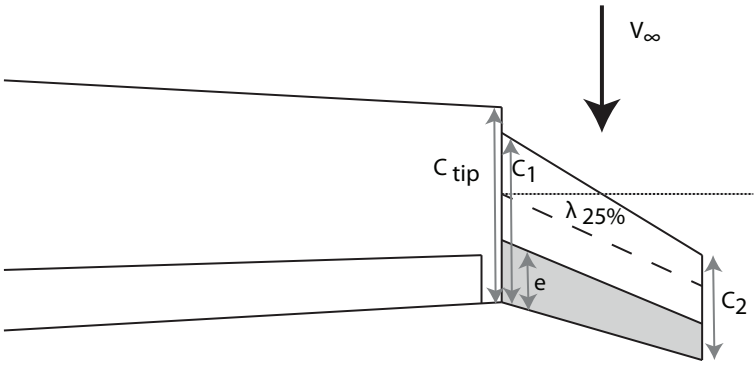

Figure 3.2: *Geometrical parameters used to study the IWT*

Table 3.1: *IWT optimal layout*

$\frac{C_1}{C_{tip}}$	$\frac{C_2}{C_1}$	$\frac{e}{C_1}$	25% Sweep [deg]	L [m]	Dihedral [deg]	All-Movable
1	0.5	0.35	35	1	0	no

After a preliminary sizing, the IWT was added to the aeroelastic stick model of the TP90, depicted in Fig. 3.3.

The stick model was translated into a State-Space model exploiting Neo-CASS and a controller for GLA was designed following the approach presented in Sec. 3.1.

The loads are monitored in four station spanwise, at the wing root (WS00), before and after the engine (WS01 and WS02), at inboard aileron section (WS03) and at the root of the IWT (WS04). The wing's dynamic behaviour is strongly influenced by the under-wing mounted engine that divides the

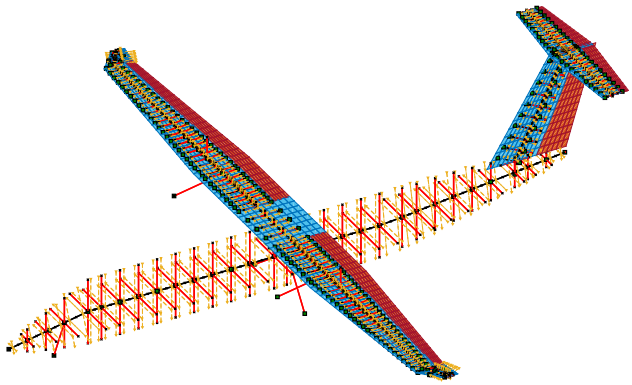

Figure 3.3: *TP90 stick model*

wing's properties in two regions: the inner wing is very stiff and its behaviour is strongly influenced by the presence of the engine, the outer wing behaves more likely as a cantilevered beam. This difference in the dynamic behaviour is accounted when designing the controller, by considering as performances the bending and torsional moment on the WS00 and WS02 sections (wing root and outer engine) in the objective function of Eq. 3.8. The gust used to design the controller is the one producing the highest WRBM.

$$f = \sum_{i=0,i=2} \frac{max|WS0i_{BM,CL}|}{max|WS0i_{BM,OL}|} + \frac{max|WS0i_{TM,CL}|}{max|WS0i_{TM,OL}|} \tag{3.8}$$

The measures used as feedback are wing-tips and centre of gravity accelerations, their numerically integrated velocities and the pitch rate coming from IMU data.
The control variables are the symmetric rotations of IWTs movable surface, ailerons and elevator. The constraints used during the optimization are: the stability of the system i.e. negative real part of the state matrix eigenvalues and control surface rotation rate lower than $80\frac{deg}{sec}$. The controller is designed on a LTI SS model in continuous time.
To verify the controller performances before wind tunnel and flight test, an aero-servo-elastic (ASE) simulator of the model is realized. The simulator has to be the closest possible to the physical aircraft, for this reason all the electronic components are modelled with the same accuracy, transfer function and sampling rate of the real aircraft. For the same reason, the simulation time discretization is the inverse of the Flight Control Computer frequency $\Delta T = 1/f_{FCC}$. Moreover, the detailed Simulink of the physical electro mechanical actuator (EMA) of the IWT is embedded in the simulator,

accounting for rate saturation, stall torque, saturation-motor temperature relation. The aircraft is modelled with the LTI SS model used to design the controller and it is intentionally left in continuous time.
The non-linear discrete time model is fully representative of the real aircraft sensing and control hardware and it can be used to verify the performance of the controller.

3.2.3 Numerical Results

The controller synthesized in the previous section is validated in with the ASE simulator. The controller is designed on the MTOW configuration of the aircraft and it is tested in 7 flight points (Tab. 3.2) and different mass conditions.

Table 3.2: *TP90 flight points*

ID	z[m]	TAS[m/s]	CAS[m/s]	EAS[m/s]	Mach
0	6096	164.6	122.3	120.2	0.52
1	0	138.9	138.9	138.9	0.41
2	5854	183.9	138.9	136.0	0.58
3	8534	177.3	115.6	112.5	0.58
4	0	162.0	162.0	162.0	0.48
5	5801	212.6	162.0	157.7	0.67
6	8534	204.9	134.7	130.0	0.67

In the following some results for the GLA controller are presented. The flight point considered is the FP2 (VMO at cruise altitude) and the gust is the one producing the maximum wing root bending moment.
Fig. 3.4 shows the comparison between open and closed loop values of the bending and torsional moment at the wing root (WS00). The WRBM peak is lowered of a 10% while the torsional peak is slightly increased. The WS02 monitoring station has a similar behaviour. Despite the increase of the torsional moment, the results reflect the optimization metric used in the controller design: the performance to be optimized is defined in Eq. (3.8) and in this case $f = 3.868$, meaning that the bending moment reduction is bigger than the torsional moment increase for the controller design gust.

The controller alleviates the bending loads spanwise, a slight increase appears for the torsional moment between the wing root and the engine section locate at 30% of the span, the spanwise maximum load distribution

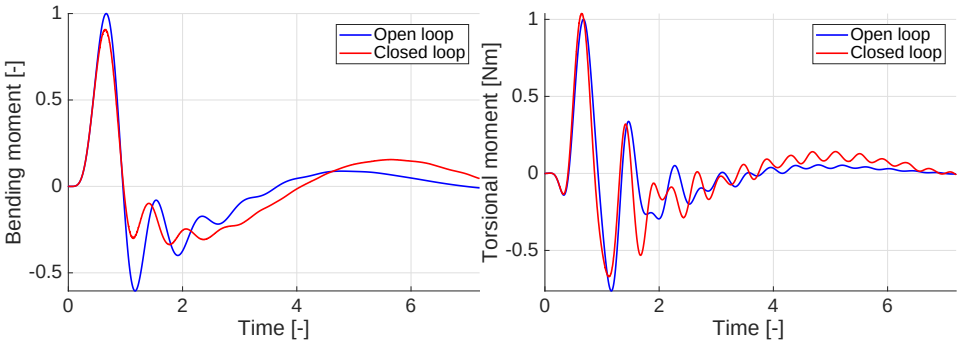

(a) *WS00 Bending moment* **(b)** *WS00 Torsional moment*

Figure 3.4: *Load station WS00 bending and torsional moment in open and closed loop*

is shown in Fig. 3.5.

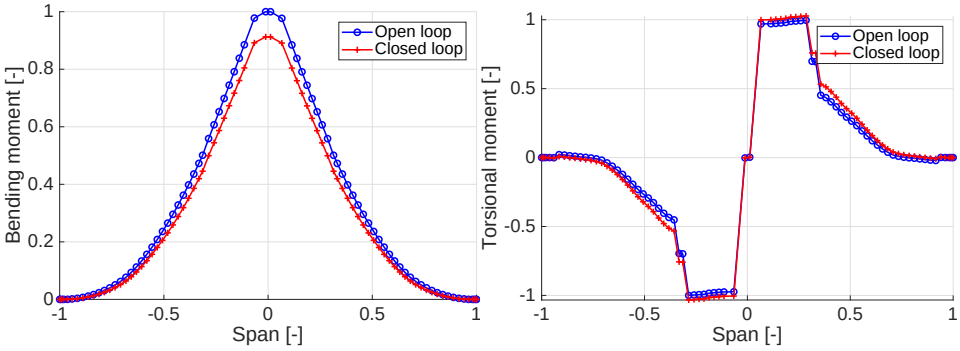

(a) *Bending moment spanwise distribution* **(b)** *Torsional moment spanwise distribution*

Figure 3.5: *Spanwise distribution of bending and torsional moment in open and closed loop*

The peak variation with respect to the open loop simulation is reported in Tab 3.3.

The acceleration peak of the centre of gravity (Fig. 3.6a) does not changes with the GLA controller while a 30% reduction is obtained for the wing tip acceleration (Fig. 3.6b). Not significant comfort improvement is achieved with this kind of controller, which is mainly designed to alleviate loads rather than reduce accelerations i.e. load factor.

The controller activity is represented by Fig. 3.7, the deflections are lim-

Table 3.3: *Flight Point 2 load comparison between open and closed loop for the gust producing highest WRBM*

Station	Bending moment	Torsional moment
WS00	-9.3%	3.8%
WS01	-10.9%	2.1%
WS02	-11.3%	3.6%
WS03	-12.7%	26.6%
WS04	-22.2%	-9.8%

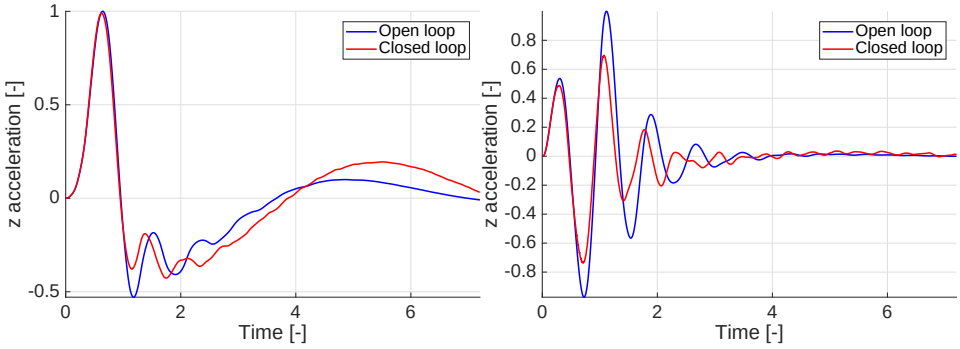

(a) *CG vertical acceleration* **(b)** *Wing tip vertical acceleration*

Figure 3.6: *CG and wing tip vertical acceleration in open and closed loop*

ited in a $\pm 5^{\circ}$ range, ensuring enough control authority to the pilot command. The control surface rotation rate is well below the $80 \frac{deg}{s}$ constraint imposed for the controller synthesis.

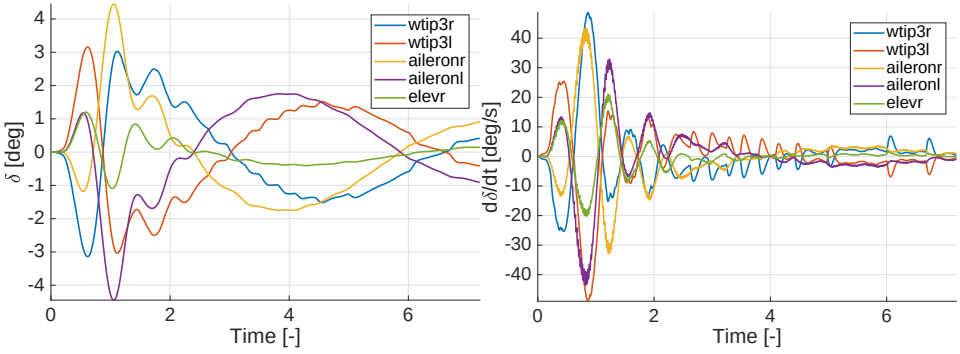

(a) *Control surface deflection* **(b)** *Control surfaces deflection rate*

Figure 3.7: *Control surface motion in closed loop*

Despite the controller performance are satisfying, there are some drawbacks due to the electronic hardware. The combination of low sampling frequency and low accuracy of the sensors lead to some discrepancies between the physical and measured values. Fig. 3.8a shows how the low accuracy of the CG accelerometer leads to a "stairs" shaped acceleration. A similar effect, due to low sampling rate, appears for the pitch rate measure Fig. 3.8b.

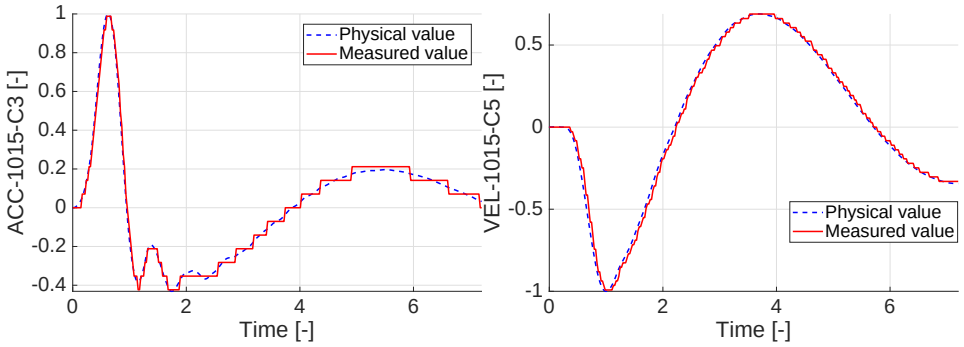

(a) *Physical vs. measured CG vertical acceleration* **(b)** *Physical vs. measured pitch rate*

Figure 3.8: *Physical vs. measured value for CG*

The situation is even worse when the indirect measure are considered i.e. the vertical velocity of Fig. 3.9, which is obtained through the numerical integration of the measured acceleration.

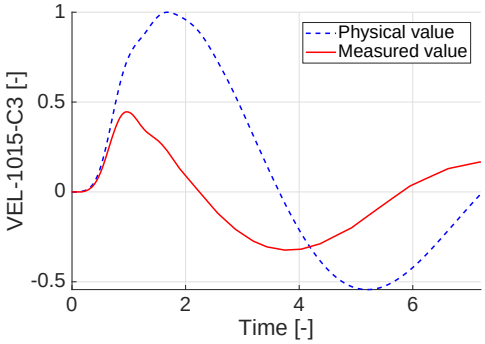

Figure 3.9: *Physical vs. velocity through numerical integration for CG*

The limitation of actuation system are visible in Fig. 3.10, the actuator acts like a low pass filter: on one hand it smooths the system input

(Fig 3.10a) filtering the higher frequency dynamics, on the other hand it introduces a delay which affect the effectiveness of the controller. This effect is considered during the controller design by modelling the actuator dynamic with a 2nd order low pass filter with 8Hz cutting frequency.

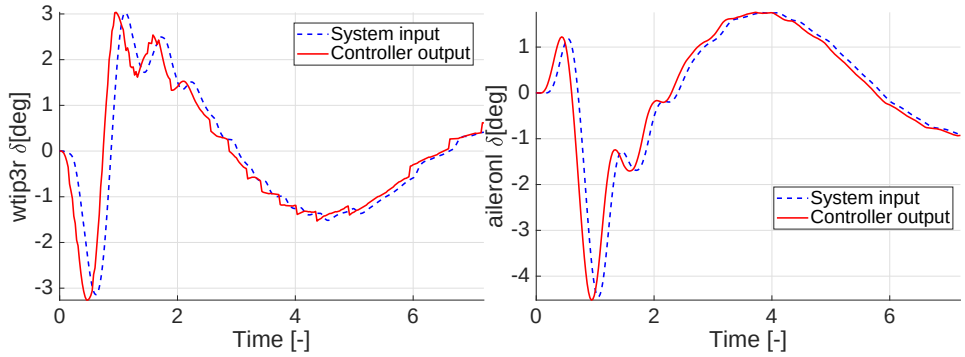

(a) *Required IWT deflection vs. aeroelastic system input* **(b)** *Required aileron deflection vs. aeroelastic system input*

Figure 3.10: *Required deflection vs. aeroelastic system input*

The controller, designed on a linear and time-continuous model, is effective even for a non-linear time-discrete model for the design gust.
Additional investigations of different flight points and mass configurations show that the controller performance worsen for faster gust i.e. low gust gradient (Fig. 3.11), specially in terms of inner wing's torsional moment. In fact higher frequencies gust excites the torsional mode of the wing, which is close to the bandwidth of the actuators. Despite of a general reduction of the bending moment, in some cases the the torsional load increase significantly ($\Delta WRTM > 30\%$), mainly due to the technological limitation of actuation and acquisition systems.

To verity if better performances are achievable with an improvement of the electronic hardware, without changing the actuators model, the flight computer and sampling rates are increased to 1 kHz. The results for the same gust and flight point considered before, in terms of load alleviation are reported in Tab. 3.4 where the bending (BM) and the torsional(TM) moment for the low (LF) and high(HF) frequency hardware are compared.

The bending moment reduction is improved in the inner wing section while it is slightly worsened in the outer wing. Torsional moment is reduced

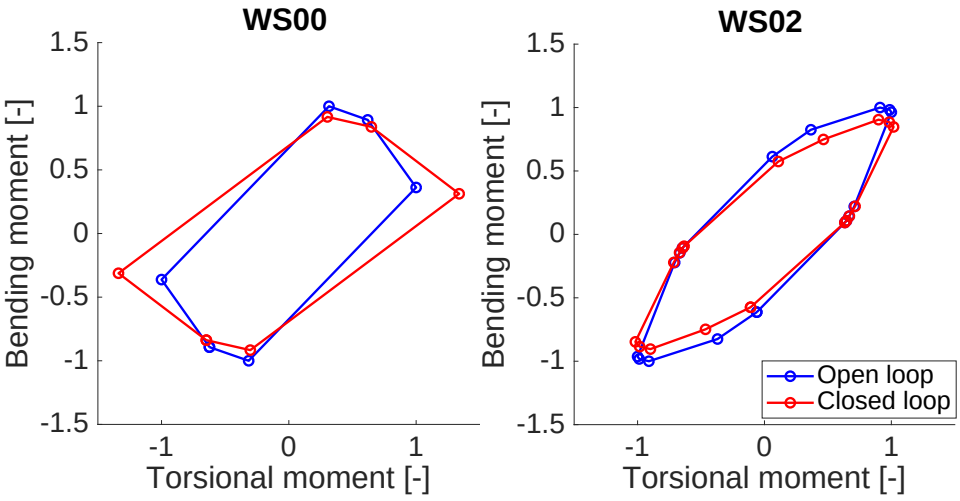

(a) *WS00 bending-torsional envelope* **(b)** *WS02 bending-torsional envelope input*

Figure 3.11: *Open loop vs. close loop load envelopes comparison*

Table 3.4: *Flight Point 2 load comparison*

Station	BM LF	BM HF	TM LF	TM HF
WS00	-9.3%	-11.1%	3.8%	-6.9%
WS01	-10.9%	-11.3%	2.1%	-13.0%
WS02	-11.3%	-11.3%	3.6%	2.5%
WS03	-12.7%	-8.0%	26.6%	25.9%
WS04	-22.2%	-16.6%	-9.8%	20.6%

in inboard wing, the big difference appears at the IWT root where the torsional moment increases (WS04). This section is not considered in the objective function, hence the increase of the internal forces at this section are acceptable. Fig. 3.12 represents the spanwise distribution on bending and torsional moment in open and closed loop with the two electronic hardware. The improvement between the wing root and the engine section is visible and not negligible.

The improved electronic hardware limits the closed loop torsional moment envelop increase: in the worst case the wing root torsional moment increases of 11% with respect to the open loop values, while the closed loop increment obtained with the nominal electronics is 33%. The gust load envelope for open loop, low frequency closed loop and high frequency closed loop for the root and engine section is reported in Fig. 3.13.

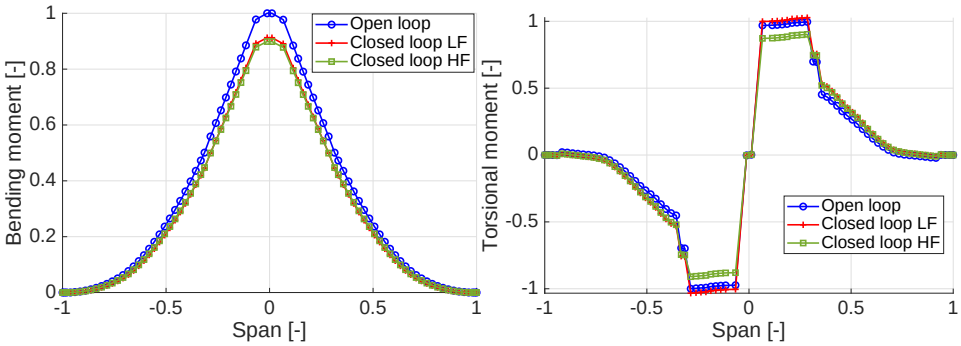

(a) *Bending moment spanwise distribution* **(b)** *Torsional moment spanwise distribution*

Figure 3.12: *Spanwise distribution of bending and torsional moment in open and closed loop*

The controller implemented for this kind of aircraft achieve a 10% reduction of the WRBM and an increase in the WRTM that depends on the electronic hardware used, in general bending moment is more critical than the torsional one for the sizing process and a slight increment of the last one is accepted if it provides significant WRBM reduction.

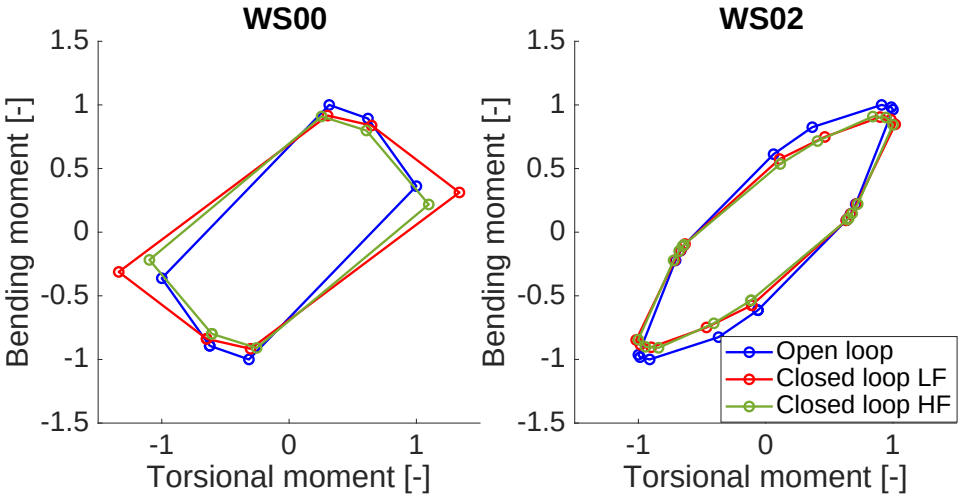

(a) *WS00 bending-torsional envelope, LF vs. HF* **(b)** *WS02 bending-torsional envelope, LF vs. HF input*

Figure 3.13: *Open loop vs. closed loop, LF vs. HF, load envelopes comparison*

3.2.4 Experimental validation

A task of the Airgreen 2 project is devoted to the wind tunnel test of the GLA controller designed in the previous section. The test are performed at the Politecnico di Milano large wind tunnel, which has a 4x4x6m test room and reaches 55m/s.
The wind tunnel model is a revamping of the model used in the GLAMOUR project [80], since the scaled dimension of the TP90 are similar to the one of the existing model, the similar components (fuselage beam and aerodynamic sectors, VTP) are recycled while the wing and the HTP are completely redesigned matching the scaled properties of the TP90.
The scaling of the model is performed keeping constant the time scale, in this way the dynamic of the scaled model is identical to the reference aircraft one. This approach allows to directly apply the full-scale control laws to the wind tunnel model, the only modification to the controller is the scaling of its input, following the scale factor of the measures used as feedback. The digital implementation of the controller allows to apply the sampling and controller frequency of the reference aircraft.
The iso-frequency scaling process implies that the length and velocity scaling factors must be the same. The problem is that a length scale factor of 1/12 should be used to fit the full aircraft in the wind tunnel, this would lead to an extremely low values of wind tunnel speed (10-15 m/s) and to a small and thin wing in which it would be impossible to fit the actuation system for the control surfaces. To avoid this issue, only half model is realized and it is vertically mounted. The half model allows to increase the length/velocity scale factor up to 1/6, Fig. 3.14 shows the top view of the model installed in the wind tunnel.

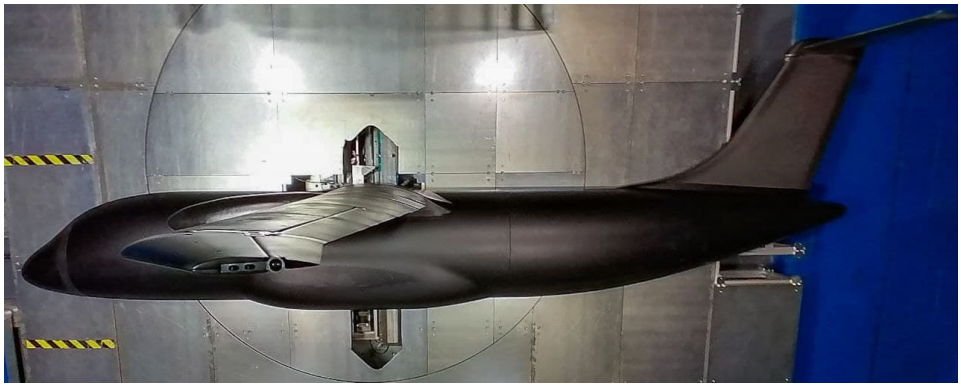

Figure 3.14: *WTT3 top view inside the wind tunnel test room*

The longitudinal symmetry of the model automatically delete the non-symmetric rigid body motion (yaw, roll and translation along the wing span), the translation in fuselage direction is not accounted because it is not relevant for the gust response and it would imply a system that counteract the model's aerodynamic drag. The free body motion is reduced to two rigid body modes: the vertical displacement as known as plunge and the pitch rotation around the centre of gravity. To preserve these two rigid body motion, the model is mounted on a pivot joint that allows the pitch rotation and which is connected to a sledge mounted on two parallel track that allows the plunge motion. This mechanism is in correspondence of the centre of gravity and allows to reproduce the rigid aircraft dynamic.
The unconventional test layout with the vertically mounted model introduces the problem of trimming the aircraft: the lift generated is not counteracted by any weight force because the gravity is perpendicular to the lift. Two solution are available to solve the problem: the first one is to trim the aircraft to have a zero lift condition, the second one is to reproduce the weight of the aircraft and trim on the equilibrium point. The model implements the second option, in this way it is possible to perform a trimmed gust response (1g load + dynamic load), the weight of the aircraft is reproduced by an electro-magnetic actuator which acts on the plunge sledge and introduces a forces equal to the scaled aircraft weight. This mechanism is called Weight Augmentation System (WAS) and allows to trim the aircraft for different load factors.
Once decided the length, velocity and time scaling factor, it is possible to recover the scaling factors for the other properties. The scale factor for mass and elastic properties are obtained keeping constant the ratios between aerodynamic forces and inertial/elastic forces. The Froude's number (ratio between inertial forces and weight) can not be maintained because of the test layout (gravity direction is different), but thanks to the WAS it is possible to scale the force acting on the centre of gravity, hence the Froude number is the same for the plunge motion. Reynold's and Mach's number are not respected, but their impact on the dynamic loads is less relevant than aerodynamic, elastic and inertial forces. Tab. 3.5 reports the scaling factors of the relevant properties.
The model is excited with a gust profile that is equivalent to the scaled real one, Fig. 3.15 shows the comparison between the theoretical 1-cos scaled gust velocity and the one measured in wind tunnel before the test: the experimental gust reproduces the numerical gust with good quality.
The model is excited with the gust and the responses in open and closed loop are measured in terms of bending moment and acceleration. The open loop acceleration profile of the wing tip obtained in wind tunnel is similar to

Table 3.5: *Scaling factors*

Parameter	λ	Scaling Factor
Length	λ_L	$1/6$
Velocity	λ_V	$1/6$
Time/Frequency	λ_t	1
Reduced Frequency	λ_k	1
Mass	λ_M	$1/6^3$
Inertia	λ_I	$1/6^5$
Bending stiffness	λ_{EJ}	$1/6^6$
Torsional stiffness	λ_{GJ}	$1/6^6$
Axial stiffness	λ_{EA}	$1/6^4$

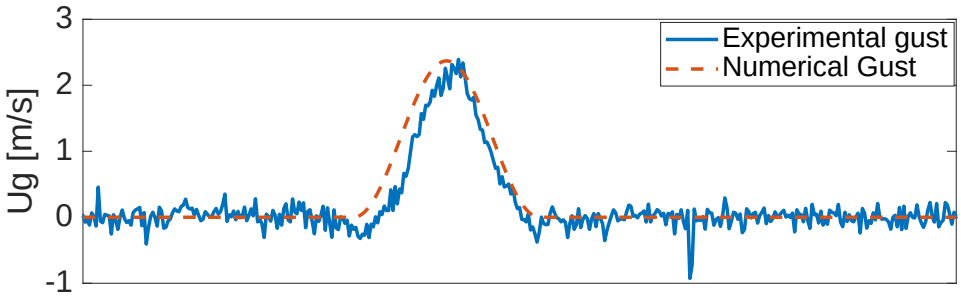

Figure 3.15: *Numerical and experimental gust profile*

the numerical one, meaning that the aero-elastic behaviour of the wind tunnel model is well matched, as Fig. 3.16 shows.

The comparison of the wing root bending moment (Fig. 3.17) shows a good

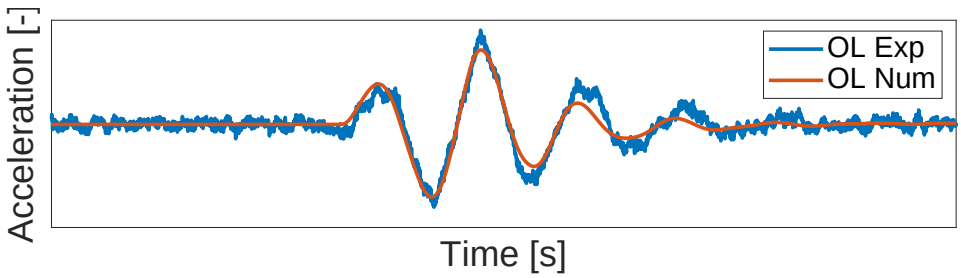

Figure 3.16: *Open Loop numerical and experimental wing tip acceleration comparison*

correlation between numerical and experimental results, both for the open and close loop responses. The difference in the WRBM response after the first peak is mainly due to the free body motion, which is not well reproduced by the wind tunnel model and the wing appears to be more similar

to a clamped wing rather than a fully free 2DOF system. Despite this difference, the first peak, mainly due to the dynamic properties of the wing (first bending mode in this case), is well matched in terms of magnitude. The alleviation achieved is around 9% for the experimental test, close to the 9.3% numerically predicted.

The correlation between numerical and experimental data means that the

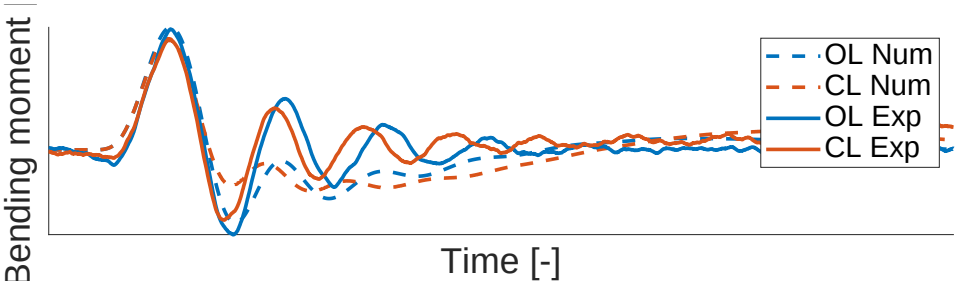

Figure 3.17: *Open Loop and Closed Loop, experimental and numerical wing root bending moment comparison*

wind tunnel model is representative of the real aircraft and it is possible to test the controller in wind tunnel and validate the GLA technology before flight tests.

The load alleviation predicted with the numerical model is achieved in the wind tunnel experiment, meaning that the controller design methodology applied is effective for the gust load alleviation purpose.

Tab. 3.6 summarizes the alleviation obtained in the wind tunnel for three station spanwise for the fligth point and gust considered: the two speeds are equivalent to the VMO and VD, the gust frequency used are the one which produces the maximu wing root bending moment (Max) and the one tuned on the first wing bending mode (Tuned). Each flight point is excited with positive and negative gust. The control reduces the loads for all the condition tested, except for the VMO positive tuned gust. This result seems more like a test issue rather than a controller failure. The mean reduction oof the eight test performed is reported in the last raw of the table.

Acknowledgements

Part of the research described in this document has been carried out in the framework of AIRGREEN2 Project, which gratefully received funding from the Clean Sky 2 Joint Undertaking, under the European's Union Horizon 2020 research and innovation Program, Grant Agreement No. 807089-REG

Table 3.6: *Wing bending moment alleviation achieved in the wind tunnel*

V_∞	Gust sign	gust frequency	WS00	WS01	WS02	WS03
VMO	+	Max	-9.1%	-8.5%	-10.4%	-16.0%
VMO	-	Max	-3.9%	-6.4%	-7.3%	-10.0%
VMO	+	Tuned	0.9%	0.1%	-1.7%	0.6%
VMO	-	Tuned	-1.6%	-4.6%	-5.9%	-10.2%
VD	+	Max	-2.1%	-7.1%	-9.3%	-11.7%
VD	-	Max	-4.1%	-11.3%	-13.4%	-19.6%
VD	+	Tuned	-11.7%	-10.8%	-13.2%	-17.7%
VD	-	Tuned	-5.7%	-6.4%	-6.2%	-1.9%
Mean			-4.7%	-6.9%	-8.4%	-10.8%

GAM 482 2018-H2020-IBA-CS2-GAMS-2017.

3.3 Active Flutter Suppression

This section summarizes the activities carried out in the framework of the Active Flutter Suppression (AFS) project. It was a cooperation between University of Washington and Politecnico di Milano sponsored by Federal Aviation Administration (FAA), devoted to the investigation and validation of technologies for flutter suppression on a wind tunnel model. The following sections provides an overview of the project, focusing on the development of an AFS control law, its implementation and testing on the wind tunnel model.
A detailed description of the project can be found in [81–83].

3.3.1 Project overview

The aim of the AFS Project is to investigate different control strategies to suppress the flutter on a wind tunnel model and understand their sensitivity to gain and delay variation.
The wind tunnel model is a revamping of the X-DIA project [84–87], which was designed for flutter studies on a three surfaces aircraft. The model installed in the Politecnico's wind tunnel is represented in Fig. 3.18.
The model is designed to have non-explosive flutter around 40 m/s, it is equipped with a safety flutter recovery system that increases the flutter speed to 45 m/s. It consists in a sliding mass at the wing tip which is actuated with a pneumatic actuator, when the acceleration exceeds a given threshold, the mass is automatically moved forward, changing the inertial properties of the wing an stopping the flutter mechanism.

The model has about 3m of wing span and it is equipped with conventional

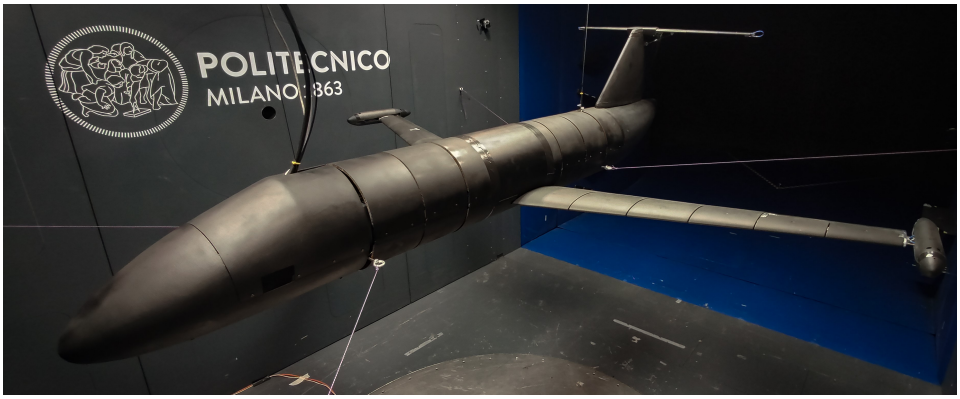

Figure 3.18: *X-DIA model in the Politecnico of Milano wind tunnel*

control surfaces like ailerons and elevator (Fig. 3.19). The model is instrumented with a set of accelerometers to save the measures used both for flutter identification and control.

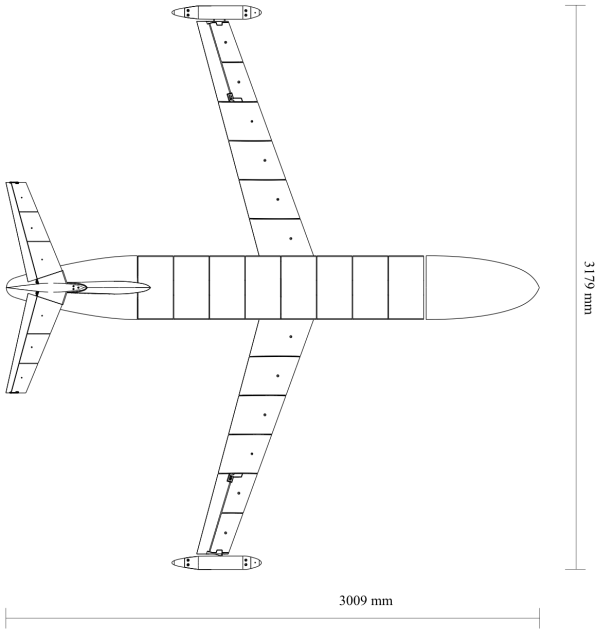

Figure 3.19: *X-DIA size and top view*

The main features of the wind tunnel model are:

- stiffness properties represented by internal aluminium spars
- 3D printed and composite aerodynamic sector to represent the external shape, fixed to the spars on a single point to do not change the stiffness properties
- movable surfaces (ailerons and elevator) for excitation and control
- Anti-flutter sliding safety mass to recover from flutter if control fails
- On-board PC for data acquisition and control law application
- Ground communication through an ethernet cable and power supplied by a power cable.

The wind tunnel tests are the conclusion of the work lasted two years which can be summarized as follow:

1. Re-design of the old three surface forward swept X-DIA model into a more conventional T-tail configuration with a positive sweep angle for the wing.

2. Design of the new components (aerodynamic sector, control surface, HTP)

3. Production of a single wing

4. Dynamic identification and updating of a single wing through GVT and clamped half wing in the wind tunnel

5. Full model production, assembly, GVT & updating

6. Wind tunnel flutter identification and passive anti-flutter testing

7. Wind tunnel AFS investigation

3.3.2 Control Law Design

The control law is designed following the procedure shown in Sec. 3.1. The measure used as feedback are the wing tips accelerations, which are numerically integrated to obtain the velocities. The control input is provided by the ailerons. The choice of the measures and input points leads to a control architecture similar to the Identically Location of Accelerations and Forces (ILAF) structure [88–91]. This kind of controller is a classical approach from the very early days of active control development for flexible aircraft. It is based on the insight that if velocity measurements can be linked to forces at the locations of those velocity measurements and in the opposite direction, a mechanism for adding damping to the structure by active control can be materialized that will be independent of the mode shapes of the configurations to be stabilized.
The choice of using the velocities as gain matrix inputs is driven by the nature of the phenomena to be controlled, the flutter is classified as a lack of damping. In the classic formulation of dynamic, the damping is proportional to the velocity: $m\ddot{x} + \mathbf{c}\dot{\mathbf{x}} + kx = F$. It is natural to think a controller which increases directly the damping of the closed loop system e.g. a control term proportional to the velocity to have additional term which can be summed to the aero-structural damping: $m\ddot{x} + (c\dot{x} + G\dot{x}) + kx = 0$.
This idea is implemented through a SOF controller where the numerically integrated acceleration are the input of the controller. The gain matrix is optimized using as constraint the stability of the system.

In this case, the objective function is the ratio between closed and open loop wing tips accelerations expressed in Eq. 3.9.

$$f = \frac{max|\ddot{x}_{left\ CL}|}{max|\ddot{x}_{left\ OL}|} + \frac{max|\ddot{x}_{right\ CL}|}{max|\ddot{x}_{right\ OL}|} \tag{3.9}$$

The constraints are the stability of the system $\xi(\lambda_i) < 0$ and the control surface deflection rate $\dot{\delta} \leq 80°/s$. The flight envelope (10-50 m/s) root locus of the open-loop system is shown in Fig. 3.20. The **+** markers indicate the eigenvalues at the flutter speed of 41.7 m/s. The flutter mechanism is a coupling between the wing bending and the wing torsional mode, the frequency of the unstable pole is around 6Hz, well below the actuator bandwidth of 12 Hz.

The aim of the controller is to increase the flutter speed of 10%, extending

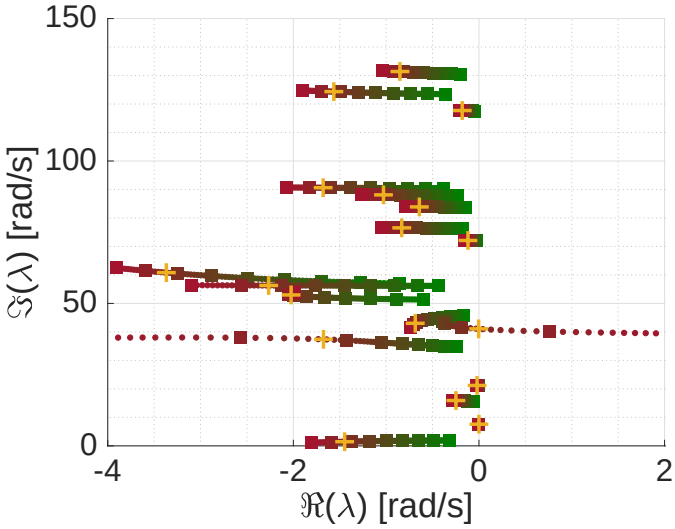

Figure 3.20: *X-DIA SS model root locus of the flight envelope*

the flutter limit up to 45.5 m/s. The controller is designed on the SS assembled for the target velocity and then it is tested over the flight envelope.
The feedback is performed on the wing tips velocities, obtained through the numerical integration of the accelerations. The structure of the controller is the one in Eq. (3.10)

$$\mathbf{u} = -\hat{\mathbf{G}}\mathbf{y} = \begin{Bmatrix} \delta_r \\ \delta_l \end{Bmatrix} = \begin{Bmatrix} g_1 & g_2 \\ g_3 & g_4 \end{Bmatrix} \begin{Bmatrix} \text{vel tip right} \\ \text{vel tip left} \end{Bmatrix} \tag{3.10}$$

The nature of the flutter is a symmetric bending-torsion coupling, which suggest to adopt a symmetric control input $g_3 = g_2,\ g_4 = g_1$, reducing the gains

to be defined to g_1 and g_2. A further simplification to the controller is introduced by using as feedback the mean of the two measures, leading to the controller structure of Eq. (3.11)

$$\hat{\mathbf{G}} = \begin{Bmatrix} g_1 & g_1 \\ g_1 & g_1 \end{Bmatrix} \tag{3.11}$$

The first optimization performed lead to a gain value of $g_1 = 0.8567$ and the correspondent root locus is depicted in 3.21a, with a zoom on the imaginary axis in 3.21b. The star markers indicate the closed loop poles at the optimal solution while the dots represent the evolution of the poles for a gain increasing from 0 to 1 with .01 step.
The constraint adopted for this solution is that all the eigenvalues have negative real part (or positive damping). The optimizer increases the gain until the unstable pole is stabilized and then continues to increase the gain until another pole reaches the imaginary axis. The obtained solution is stable but a slight increase of the gain would destabilize the system.

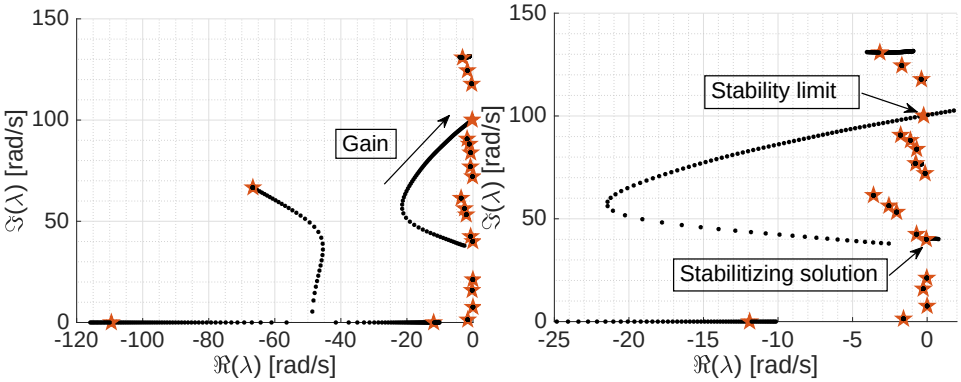

(a) *Root locus* **(b)** *Zoom on imaginary axis*

Figure 3.21: *X-DIA SS model root locus at 45 m/s, control gain 0:0.01:1 and optimal gain g=0.85*

For this reason a constraint on the evolution of the critical mode is imposed, in order to maximize the damping of this pole. The optimization with the updated constraints set leads to a gain $g_1 = 0.25$. The root locus for the closed loop system with the updated gains is shown in Fig. 3.22, where the mode which was close to instability with the previous gain is now well damped.

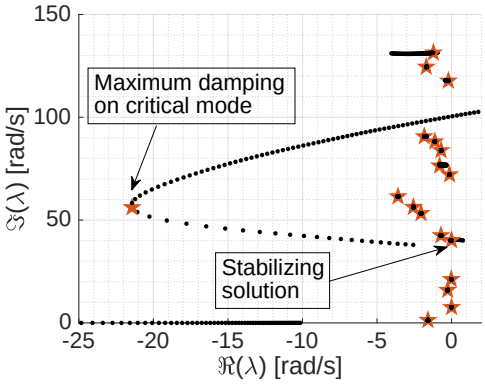

Figure 3.22: *X-DIA SS model root locus at 45 m/s zoom on the imaginary axis, control gain 0:0.01:1 and recomputed optimal gain g=0.23*

Fig. 3.23 shows the comparison between the OL and CL root locus evolution with the increasing airspeed (10:1:50m/s, multiple of 10m/s are bigger markers). The CL flutter speed is moved between 45 and 46m/s and the flutter mechanism is more damped and approaches the imaginary axis with a more gradual $\frac{\Delta\xi}{\Delta V}$ ratio.

Fig. 3.24 shows a comparison between open-loop and closed-loop re-

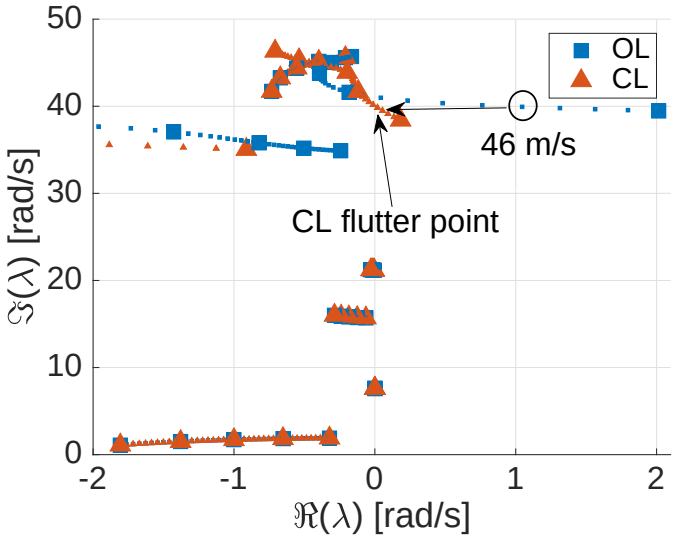

Figure 3.23: *Comparison between the OL and CL root locus evolution increasing the airspeed, 10-50 m/s. Bigger marker at 10-20-30-40-50 m/s*

sponse to a sinusoidal aileron excitation (1°, 6.5 Hz): for the closed loop system the tip acceleration doesn't diverge while the open loop is clearly

unstable.

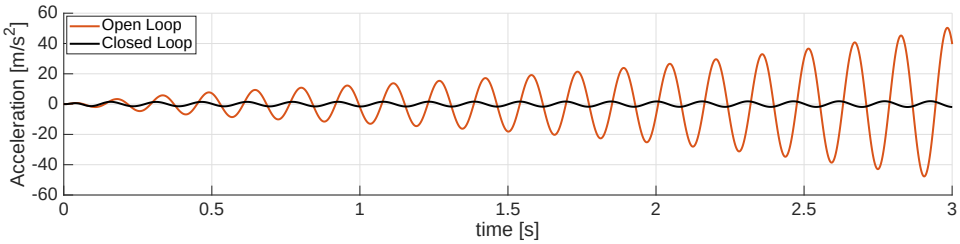

Figure 3.24: *X-DIA SS model response to 6.5Hz sine aileron excitation at 45 m/s, wingtip acceleration*

Before applying the controller to the wind tunnel model, it was tested on a numerical simulator realized with a discrete time state space model in Simulink, where the continuous time models were translate in the discrete time and the sampling frequency used is the same of the experiment. Fig. 3.25 presents a comparison between the continuous and discrete time model (1000Hz), the acceleration due to the same sinusoidal input are the same for the two models.

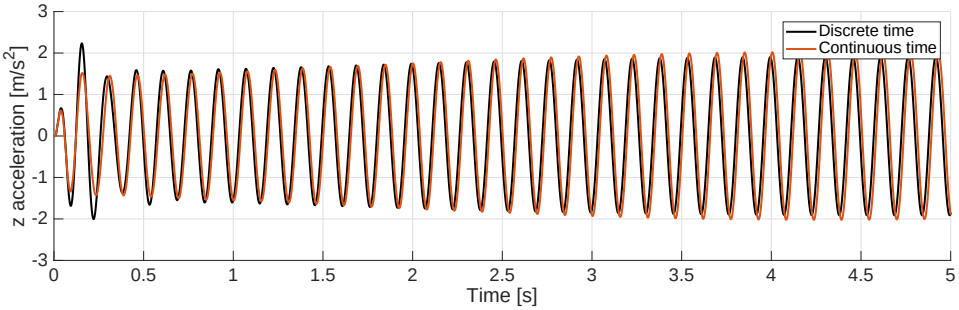

Figure 3.25: *X-DIA Simulink model response to 6.5Hz sine aileron excitation at 45 m/s, comparison between discrete and continuous time of the wingtip acceleration*

3.3.3 Wind tunnel test

The designed controller is applied to the wind tunnel model, the air speed is increased with the active controller disengaged and data are acquired for the open loop. The model is excited using the ailerons, the excitation is a chirp signal between 4 and 9Hz and 50s duration (Eq. (3.12)), for each test point the model is excited for 3 minutes (50s excitation 10s rest for 3 times) to have enough data to perform a mean of the identified transfer functions. A trigger signal is generated to identify the 3 excitation slots.

$$y(t) = A \sin\left(2\pi\left(f_0 + \frac{f_1 - f_0}{T}t\right)t\right) \tag{3.12}$$

The wind tunnel model is stable up to 41 m/s and a 0.5m/s increase in the wind tunnel speed leads to the flutter.
Once identified the flutter point, the controller is enabled and the data are collected for the same flight points (20,30,40 m/s) and for the same excitation method. The data are processed using Matlab's signal processing toolbox [92].
The sum of the frequency response function for the test matrix is shown in 3.26. Increasing the wind tunnel speed it is possible to see how the 5Hz peak (wing bending) becomes stiffer and more damped while the 7Hz peak (wing torsion) becomes less stiff an less damped, until 40m/s where the frequency separation between the modes is low. Increasing the wind tunnel speed to 41.5 m/s the torsional mode becomes unstable and flutter occurs. The controller acts introducing more damping to the system and it is possible to see how the peaks of closed loop transfer functions in Fig. 3.26 are suppressed in the range of 4-9Hz.
Fig. 3.27 shows a comparison between the open-loop and closed loop fre-

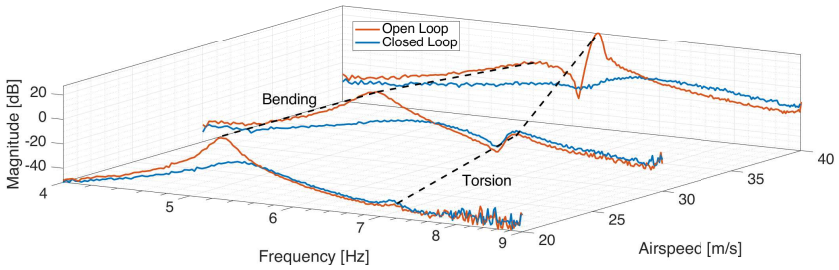

Figure 3.26: *X-DIA identified FRF between 20 and 40 m/s*

quency response function (FRF) at 40m/s, the mode which is going to be unstable in open-loop (6Hz peak) is flatten by the action of the controller.

In time domain it is possible to observe the same behaviour (Fig. 3.28), the system is excited with the chirp signal of Eq. (3.12) and it is possible to know the excitation frequency for each time. Between 23 and 30s, respectively 6.07Hz and 6.77Hz of the chirp signal, the wing tip acceleration of the closed-loop system is limited in a 1.5g band, while the open-loop acceleration has a band of 5g (the -1g offset is the gravitational acceleration). The frequency interval is the same of the peak highlighted by the FRF of Fig. 3.27. In the same frequency interval, time domain response suggests

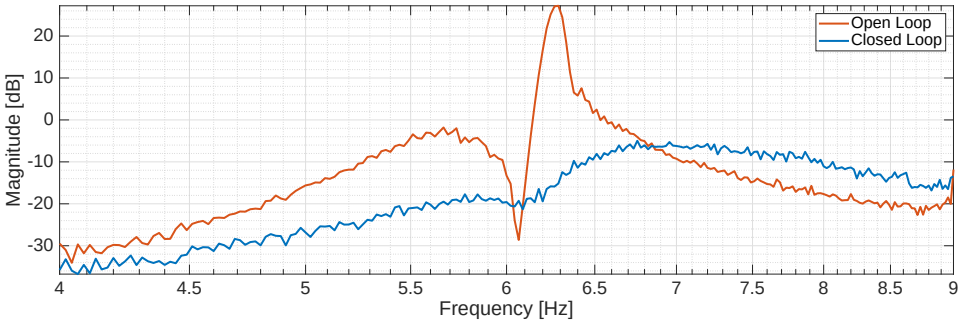

Figure 3.27: *X-DIA identified FRF at 40 m/s*

the presence of three modes (the 3 pack of signal amplified) which are indistinguishable from the FRF analysis.

The controller is effective reducing the open loop FRFs peaks below the

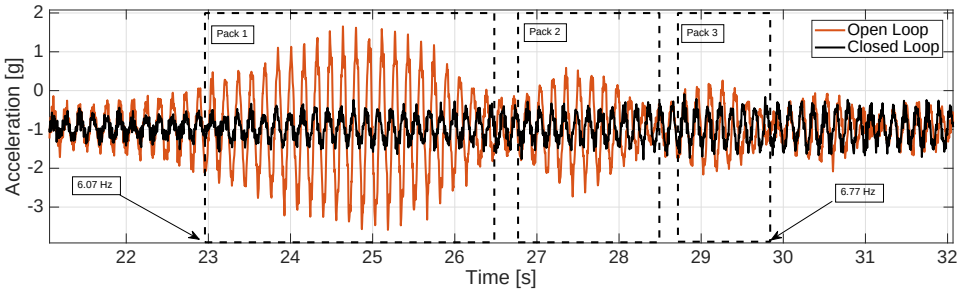

Figure 3.28: *X-DIA acceleration due to a chirp excitation through aileron rotation at 40 m/s*

flutter point, the next step is increasing the wind tunnel speed to define the robustness of the controller and its efficiency in stabilizing the system beyond the flutter point.

Flutter point and beyond

Thanks to the anti-flutter safety system, it is possible to increase the wind tunnel speed beyond the flutter point safely, if the flutter occurs or if the controller fails the safety system moves the mass in forward position and switches off the controller, recovering the stability of the system. The threshold for the safety system activation is 5g for the wing tip accelerometers. This approach allows to fly the model outside its open-loop flutter envelope and to investigate how much the flutter boundary can be increased with an AFS strategy.

In this protected environment, the wind tunnel speed is increased with 0.5m/s

step up to 47m/s and the aircraft is stable, this speed increment is equivalent to a 30% increase of the dynamic pressure.
To investigate the robustness of the controller, delay and gain variation were applied to the control scheme. At flutter point (41.5 m/s) the controller is stable with a variation of the nominal gain in the range on 15%-200% and a delay up to 10ms. Beyond the flutter point the controlled system is stable with a 5ms delay up to 45m/s. Tab. 3.7 shows a summary table of the controller tested.
The stability is guaranteed with a gain reduction of 50%, which means that

Table 3.7: *Summary table of tested controller*

V [m/s]	Gain	Delay[ms]
0-47	100%	0
41.5	100%	10
45	100%	5
41.5	20%-200%	0

thanks to the feedback strategy adopted (mean values of tip accelerations), the controller is able to keep the aircraft stable even if a measurement channel is lost.

Acknowledgements

Support by the Federal Aviation Administration as well as contributions by Wael Nour and Sohrob Mottaghi from the FAA are gratefully appreciated.

3.4 Concluding remarks on active control

This section highlighted a possible control synthesis approach which is suitable for flutter suppression and gust load alleviation. The Matlab based procedure is fully automatic once the control inputs, measures and performances are defined. This makes the control law design methodology fully automated and ready to be implemented in the overall aircraft optimization loop, where at each function evaluation the control law can be re-designed to follow the modification of the aircraft's aeroelastic behaviour.
The user friendly structure of the controller and the automatic design process allows the exploitation of the control design framework by people that are not experts in this field, providing them a preliminary design of the control law. The numerical and experimental results prove the quality and

soundness of the proposed approach, which generates a simple and versatile controller with few user provided information (measures, performances and control inputs).
The controllers designed in a continuous time domain (LTI models) are effective when translated in discrete time, the technological limitation of the actuation systems are accounted during the controller design in term of actuator bandwidth and surface rotational rate as a constraint.
Other better, more performant and robust control approaches could be implemented in the optimization loop, but the goal of this thesis in not a comparative study among the performances of different controller design methodologies. One of the objective of the thesis is to understand if and how the active control affects the structural sizing in preliminary design phases.

CHAPTER 4

NeOPT: the optimization framework

4.1 Short introduction to the optimization in aeronautical engineering

Nature optimizes [93].
People optimize.
Aeronautic engineering optimizes.
We could draw up a infinite list of activities and behaviours which can be described as optimization processes. Most of them can be considered spontaneous, like walking a straight line between two points or birds flying in a V formation. Numerical optimization is the process of modelling a problem by identifying objectives,variables and constraints. This process applies to aeronautical engineering in many disciplines at several level with different objectives and constraints.
The list of optimization software is long and it is not the objective of this section to write a survey of them, but it is important to understand how they work. Since unconstrained optimization finds few application in engineering science, it is assumed that the problem set up is made of three steps:

1. Identification of the objective function to be minimized

2. Identification of the design variables

3. Definition of the constraints.

In the simplest cases, the relation between the design variables and the objective/constraints is explicit but in the most of the cases it is implicit and it is provided by a numerical procedure. The implicit relation goes to few line of codes to complex analysis e.g. global FEM model or RANS CFD simulation of an entire aircraft. When the optimization is multidisciplinary, the relation between the design variables and the constraint/objective is described by two ore more disciplines/numerical procedures.
Once defined the constraints, the objective, the design variables and the relationship among each other, the optimizer is in charge of understand how to vary the design variables to minimize the objective function satisfying the constraints. On this last sentence it has been written a whole literature of methods.
Two fundamental elements of a generic optimization procedure have been described above: the optimizer itself and the functions for constraints and objective evaluation. In a numerical procedure, these two elements (the optimizer and the functions) are software which can be programmed in several language, in the most general case each piece of code is written in a different language e.g. the optimizer is in Python, the objective function is evaluated with a C++ CFD solver and the constraints come from a FEM solution of a Fortran program. Focusing on the aero-structural filed, many examples of optimization are available, from the simplest elliptical lift distribution to the complex Multi-Disciplinary and Multi-Objective Design and Optimization.
In the late '80s the first attempts of MDO where performed across the whole word, Grossman, Haftka et al. in [94] showed that the results obtained with an integrated optimization are better than the one with a sequential optimization. Bindolino, Ricci and Mantegazza [95] performed a servo-structural optimization of iso/orthotropic wing with aeroelastic constraints with AIDIA. In the same years Livne, Schmit and Friedmann developed LS-CLASS for the aero-servo-elastic optimization [96]. In [97] a Navier-Stokes solver is coupled with a beam solver, while in [98] a full 3D FEM model is coupled with an Euler solver. A well documented survey of the MDO methodologies and application in aerospace up to late '90s is provided by [99] and are not here reported to do not burden the reading.
The evolution of the computer sciences together with improved optimization algorithms led to fast and reliable framework able to combine several disciplines and fast enough to obtain results in some days. One of the most widespread open source optimization framework is *openMDAO* [100], but

on the market there is a long list of commercial or open source software for optimization.
The latest achievements in high fidelity aero-elastic optimization were reached by the University of Michigan MDO Lab leaded by Prof. Martins, performing MDO aero-structural optimization like [101] (full publications list available at [102]).
In this universe of methods, software and languages, NeOPT is classified as an aero-servo-elastic wingbox optimizer suitable for conceptual and preliminary design phases, based on medium fidelity numerical models. It is part of the NeoCASS suite and it is entirely developed in Matlab.
The main difference between NeoCASS and similar aero-servo-elastic optimization framework, like TU-Delft PROTEUS [25], is the starting point of the design procedure: NeoCASS starts from a blank sheet providing the first structural aero-servo-elastic model of the aircraft, while other suites starts from an existing model. It must be pointed out that currently there are not commercial suite for the aero-servo-elastic optimization including dynamic loads and active control e.g. Nastran can perform optimization considering trim and flutter but it can not consider the gusts unless the implementation of external routines. One of the latest work about the aero-servo-elastic MDO optimization considering MLA and GLA technique is presented in [103].

4.2 Overview on NeOPT

NeOPT is the name of the optimization and sizing framework developed. It is the brain of the procedure and manages the communication among all the subcomponents presented in the previous chapters.
The most general statement of an optimization problem is:

$$\min_{\mathbf{x}} f(\mathbf{x}) \; s.t. \; \mathbf{x} \in \mathbf{S}; \; \mathbf{S} : \left\{ \mathbf{x} \in \mathbb{R}^n \; s.t. \; \mathbf{g}(\mathbf{x}) \leq \mathbf{0} \; \cap \; \mathbf{x_l} \leq \mathbf{x} \leq \mathbf{x_u} \right\} \quad (4.1)$$

Eq.(4.1) can be read as: *"In the search space S, find the set of design variables x that satisfies the constraints g and minimizes the objective function f."*. This section shows which are the objective function and the constraints adopted by NeOPT, which are the design variables and how them are linked among each other. Since NeoCASS is completely Matlab based, to preserve a unique code language and simulation environment NeOPT is coded in Matlab and exploits its functions, among which well documented optimizers are available. The chosen one is *fmincon* [104], which searches for the minimum of a constrained non linear function and the problem is specified

as:

$$\min_{\mathbf{x}} f(\mathbf{x}) \text{such that} \begin{cases} \mathbf{c}(\mathbf{x}) \leq \mathbf{0} \\ \mathbf{c}_{eq}(\mathbf{x}) = \mathbf{0} \\ \mathbf{A}\mathbf{x} \leq \mathbf{b} \\ \mathbf{A}_{eq}\mathbf{x} = \mathbf{b}_{eq} \\ \mathbf{lb} \leq \mathbf{x} \leq \mathbf{ub} \end{cases} \tag{4.2}$$

In (4.2) the search space **S** of (4.1) is subdivided in smaller domains.
With *fmincon* it is possible to impose linear/non linear equality/inequality constraints and to limit the search space between upper and lower bound. It is a gradient based optimizer and among the available solver, NeOPT uses the Sequential Quadratic Programming (SQP) algorithm based on the work of Nocedal and Wright in chapter 18 of [93]. The choice of this algorithm is due to its stability and fast convergence when starting in *hot zones* i.e. feasible solution, which comes from the GUESS sizing in our case. It requires a number of function evaluation strictly necessary for gradients (objective and constraint) estimation, computational time is proportional to the iteration duration which depends on the number of function evaluations.
The gradient computation is one of the most challenging task for gradient based optimizer, SQP manages both user provided or automatically computed gradient. The nature of the problem makes the computation of an analytical gradient difficult, hence the gradient is estimated by finite differences.
The optimization algorithm is a piece of the framework, which is made of several interconnected modules.
The first step of the procedure is the identification of the wingbox (presented in chapter 2). Once the meta-model is identified, it is possible to start the optimization process.
At this point the design variable of the optimization problem must be identified.

4.2.1 Design variables

Thanks to the meta-model it is possible to convert physical values like panel thickness and stringer area into stiffness properties. NeOPT works with the physical variables at cross sectional level.
The possible design variables for each cross section are the thickness of each skin element and the area of each stringer, this would lead to an exaggerate number of variable for the optimization problem. To limit the design variables number, a two levels variables linking strategy is adopted.

The first linking level is on the cross section, where the maximum number of variable available is 10 for a single cell wingbox and they are:

- upper and lower stringer area (2) (area of the single stringer, the cross-section number of stringers is computed in the geometry module for each rib as in Sec. 2.3, the total stringers area is $A_{tot} = N_{str} * A_{str}$).
- upper and lower skin thickness (2).
- front and aft spar thickness (2).
- spar cap thickness (4).

In case of multiple cell wingbox and additional variable is the mid spars thickness and if the skins are made of composite materials, the symmetric or asymmetric laminate orientation can be included among the variables.
When composite materials are employed, the stacking sequence is not a design variable: it is defined before the optimization process in terms of ply orientation and the % of thickness of each ply. During the optimization only the total thickness and the global orientation of the laminate are modified, not the thickness and the orientation of each ply.
The available cross section linking options are reported in Tab. 4.1.

Table 4.1: *Cross section linking options, (* if present)*

Type	Upper skin	Lower Skin	Upper stringer	Lower stringer	Front Spar	Aft spar	Spar caps	Mid Spar	Upper skin orientation	Lower skin orientation
ISO4	free	=upper skin	free	=upper stringer	free	=front spar	all equal	free*	-	-
COMP4	free	=upper skin	free	=upper stringer	free	=front spar	all equal	free*	-	-
ISO7	free	free	free	free	free	free	all equal	free*	-	-
COMP7	free	free	free	free	free	free	all equal	free*	-	-
ISO10	free	free	free	free	free	free	all free	free*	-	-
COMP10	free	free	free	free	free	free	all free	free*	-	-
ASYM4	free	=upper skin	free	=upper stringer	free	=front spar	all equal	free*	free	= upper skin
ASYM7	free	free	free	free	free	free	all equal	free*	free	= upper skin
ASYM10	free	free	free	free	free	free	all free	free*	free	= upper skin
SYM4	free	=upper skin	free	=upper stringer	free	=front spar	all equal	free*	free	= - upper skin
SYM7	free	free	free	free	free	free	all equal	free*	free	= - upper skin
SYM10	free	free	free	free	free	free	all free	free*	free	= - upper skin

The T-shaped stringer and L-shaped spar cap dimensions are parametrized on their thickness as Fig. 4.1 shows, this parametrization can be modified by the user before the optimization but not during it. The link between the thickness and the area is: $t = \sqrt{\frac{\text{Area}}{A_1+A_2}}$.

The second level of variable linking is in spanwise direction, the variable are constant for a given set of ribs, called patch. The patches are provided

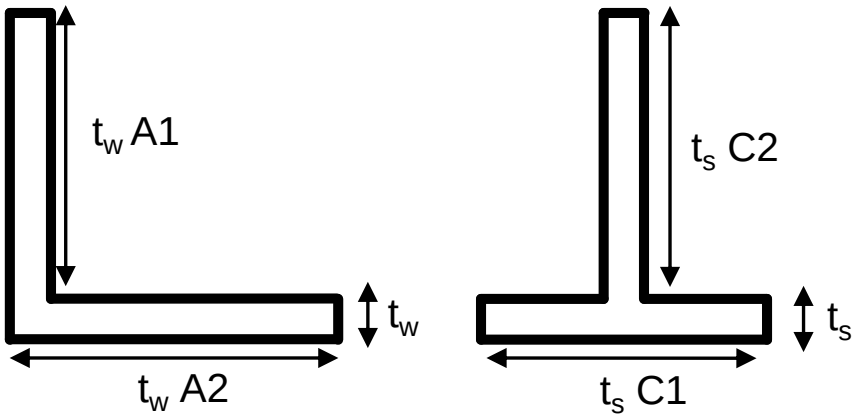

Figure 4.1: *L-shaped spar cap and T-shaped stringer*

by the user in the geometry module, their subdivision is demanded to the designer but load and geometry discontinuities like engines, kinks and control surfaces are good driver for the patches division.
The total number of design variable is equal to the cross section variables multiplied by the number of the patches i.e. $n_{tot} = n_{section} \times n_{patch}$.

4.2.2 Aeroelastic solvers

In NeoCASS there are implemented all the classical aeroelastic solvers and they can be exploited by NeOPT (between brackets the equivalent Nastran [30] solution):

- Static solution (SOL 101)
- Normal modes (SOL 103)
- Linear elastic trim (SOL 144)
- Flutter (SOL 145)
- gust and dynamic aeroelastic response (SOL 146)
- Thanks to the procedure presented in [33] [47], it is possible to realize an aero-servo-elastic State-Space (SS) model of the aircraft.
- The active control methodology proposed in Chapter 3 can be included in the design loop as well.

When the optimization problem is setted up, it must be specified which solutions are required. Typically a set of trim manoeuvres compliant with CS25 is used (usually the same used for the GUESS sizing). When the dynamic analysis is required, its type (gust, control surface deflection, external load) must be specified, when the gust analysis is required the gust length and amplitude are computed for each flight point following CS25 regulation. Flutter analysis is not used for the evaluation of the loads but for the stability of the aircraft, for each prescribed altitude the flutter analysis provides the damping of the modes, which is constrained to be positive until 120% dive speed.
If the active control is enabled, its effect is considered for the dynamic load. The procedure for defining the control design has been deeply highlighted in the previous chapter.

4.2.3 Objective and constraints

NeOPT is designed to minimize the structural mass of the wingbox, but it can use whichever response analysis as objective or as a constraints. An example is provided by the following problem: given an already optimized wingbox, try to maximize the aileron efficiency for the roll manoeuvre with a maximum mass increase of X% or minimize the structural mass of the wing with a prescribed aileron efficiency.
The structural constraints to satisfy in the optimization/sizing procedure are:

- Skins panels failure
- Stringers and spars cap failure
- Spars failure
- Skins buckling
- Stringers webs buckling
- Spars buckling
- Stiffened panels global buckling

The user can define the safety margin used to multiply the loads for the constraints evaluation, by default the safety margin applied is 1.5 both for dynamic and trim loads, safety factor reduction can be applied following the section named *Interaction of system and Structures* of EASA regulation [105].

The failure of the metallic components is computed following the Von Mises criterion in Eq.(4.3), specified for a planar stress state with two components:

$$FI_{VM} = \frac{\sigma_{yield}}{\sigma_{VM}} \text{ where } \sigma_{VM} = \sqrt{\sigma_x^2 + 3\tau_{xy}^2} \tag{4.3}$$

In case of composite material, the Tsai-Hill criterion of Eq.(4.4) is adopted.

$$FI_{TH} = 1 - \left(\frac{\sigma_1^2}{\sigma_{1MAX}^2} + \frac{\sigma_2^2}{\sigma_{2MAX}^2} - \frac{\sigma_1 \sigma_2}{\sigma_{1MAX}^2} + \frac{\tau_{12}^2}{\tau_{12MAX}^2} \right) \tag{4.4}$$

The failure index for the composite is computed for each ply, the stress obtained in the laminate coordinate system must be rotated into the lamina coordinate system following Eq. (4.5).

$$\begin{bmatrix} \sigma_1 \\ \sigma_2 \\ \tau_{12} \end{bmatrix} = \mathbf{Q}_i \mathbf{A} \mathbf{R} \mathbf{A}^{-1} \mathbf{Q}^{-1} \begin{bmatrix} \sigma_x \\ 0 \\ \tau_{xy} \end{bmatrix} \tag{4.5}$$

Where $\mathbf{Q}$ is the laminate stiffness matrix, $\mathbf{A}$ is a matrix which accounts for the relationship between ε_{xy} and γ_{xy} and $\mathbf{Q_i}$ is the i-th ply stiffness matrix. The buckling indexes are obtained following the work of Weaver and his group presented in [106] and [107], where an analytical formulation for the instability is presented. The buckling index of a simply supported plate loaded with axial, shear and bending stresses is obtained through the interaction formula of Eq. (4.6). The stress state (N_x, N_{xy}, N_b) is obtained with NeoANBA and the critical stress values ($N_{cr\ x}, N_{cr\ xy}, N_{cr\ b}$) depend on boundary conditions, geometry and material properties. These information are stored in the meta-model: e.g. the rib and stringer pitch used to evaluate the critical stress value for each component.

$$BI = 1 - \left(\frac{-N_x}{N_{cr\ x}} + \frac{|N_{xy}|}{N_{cr\ xy}} + \frac{N_b}{N_{cr\ b}} \right) \tag{4.6}$$

The critical stress values of Eq. (4.8) depends on the panel width L and bending stiffness properties of the plate i.e. $\mathbf{D}$ term in Eq. (4.7).

$$\begin{Bmatrix} \mathbf{N} \\ \mathbf{M} \end{Bmatrix} = \begin{bmatrix} \mathbf{A} & \mathbf{B} \\ \mathbf{B}^T & \mathbf{D} \end{bmatrix} \begin{Bmatrix} \boldsymbol{\varepsilon} \\ \kappa \end{Bmatrix} \tag{4.7}$$

$$\begin{aligned} N_{cr\ x} &= K_x \tfrac{\pi}{L}^2 \sqrt{D_{11} D_{22}} \\ N_{cr\ xy} &= K_{xy} \tfrac{\pi}{L}^2 \sqrt[4]{D_{11} D_{22}^3} \\ N_{cr\ b} &= K_b \tfrac{\pi}{L}^2 \sqrt{D_{11} D_{22}} \end{aligned} \tag{4.8}$$

Once again, the K factors of Eq. (4.8) depend on the plate bending stiffness matrix D as in Eq. (4.9) and Eq. (4.10).

$$\begin{aligned} K_x =& 2(1+\beta) - \frac{2(\beta+3+2\gamma^2)(\gamma+3\delta)^2}{(\beta+3)^2} + \\ & - \frac{4(\delta+2\gamma^3-\beta\gamma)(\gamma+3\delta)^3}{(\beta+3)^3} \\ K_{xy} =& 3.42 + 2.05\beta - 0.13\beta^2 - 1.79\gamma + \\ & - 6.89\delta + 0.36\beta(2\gamma+\delta) - 0.25(2\gamma+\delta)^2 \\ K_b =& 26.85 + 12.61\beta \end{aligned} \tag{4.9}$$

$$\alpha = \sqrt[4]{\frac{D_{22}}{D_{11}}};\ \beta = \frac{D_{12}+2D_{66}}{\sqrt{D_{11}D_{22}}};\ \gamma = \frac{D_{16}}{\sqrt[4]{D_{11}^3 D_{22}}};\ \delta = \frac{D_{26}}{\sqrt[4]{D_{11}D_{22}^3}} \tag{4.10}$$

In a similar way, the buckling of the T-shaped stiffeners is evaluated. The web is considered as a plate simply supported along three edges (2 short and one long edges) under axial loading. In this case the critical axial load becomes:

$$N_{cr}^{web} = \frac{12}{b^2}\left(D_{66} - \frac{D_{26}^2}{D_{22}}\right) \tag{4.11}$$

Where b, is the height of the stiffener web.
This approach manages bot iso- and orthotropic material using an unique formulation for the buckling evaluation.
When a flutter analysis is required in the optimization loop, the flutter constraint imposes the damping of the aeroelastic modes to be positive in each flight point considered (typically altitude-Mach number envelope). Surface effectiveness or maximum deflection can be constrained to avoid control reversal phenomena or lost of effectiveness due to the augmented wing flexibility.
In general, whichever analysis response can be formulated as a constraint.

4.2.4 Aerodynamics

Despite using low fidelity aerodynamic models, the computation of the steady and unsteady aerodynamic forces is a time consuming process, but it can be avoided. The aerodynamic models implemented in NeoCASS are a Vortex Lattice Method (VLM) [31] [108] for the rigid/elastic trim computation and a Doublet Lattice Method (DLM) [109] [110] for the unsteady aerodynamic forces.

The aerodynamics is coupled to the structure through a fluid-structure interface based on the splining technique presented in [111].
For both the methods the aerodynamic forces F_j computation is performed solving a linear system in the form of eq. (4.12), the influence matrix A_{jj} does not depends on the structural field, hence it and its inverse can be computed for unit boundary condition w_j (local incidence), the right-hand w_j term depends on the structural motion, but since the A_{jj}^{-1} is available, the aerodynamic forces can be obtained through a multiplication instead of solving the linear system for each analysis condition.

$$A_{jj}F_j = w_j \tag{4.12}$$

In trim case, when the aeroelastic system is assembled only mass and stiffness matrices are affected by design variables, hence only the structural part is updated and then coupled to the aerodynamic contribution. In this case no model reduction is performed and the problem is solved for all the degrees of freedom.
When a dynamic solution is required, the problem is projected and solved on an orthogonal subspace, i.e. the modal base. In this case the modal base depends on the structural properties and is recomputed for each function evaluation, the aeroelastic model is reassembled considering the updated projection space. The DLM matrices are not affected by this procedure, it changes only the base used for the projection of the forces into the reduced space.
For this reasons, a database of VLM and DLM aerodynamic matrices is computed and saved for each flight condition before starting the optimization.

4.2.5 Material and properties

NeOPT manages isotropic material as well as composites. To evaluate cross section stiffness and mass matrices with NeoANBA, elemental properties must be provided. The same properties are need to evaluate the buckling constraints as described in Sec. 4.2.3. Once defined the plate element's material, their stiffness is function of the thickness and of the material orientation if it is orthotropic, hence the properties of the elements can be evaluated only once before the optimization for unit thickness and during the optimization loop they are evaluated for the provided thickness value. The stiffness matrix of a plate is:

$$\mathbf{K} = \begin{bmatrix} \mathbf{A} & \mathbf{B} \\ \mathbf{B}^T & \mathbf{D} \end{bmatrix} \tag{4.13}$$

If the material is isotropic it becomes:

$$\mathbf{K} = \mathbf{Q}\begin{bmatrix} \int_{-\frac{t}{2}}^{-\frac{t}{2}} dz & \int_{-\frac{t}{2}}^{-\frac{t}{2}} zdz \\ \int_{-\frac{t}{2}}^{-\frac{t}{2}} zdz & \int_{-\frac{t}{2}}^{-\frac{t}{2}} z^2 dz \end{bmatrix} = \mathbf{Q}\begin{bmatrix} t & 0 \\ 0 & \frac{1}{12}t^3 \end{bmatrix} = \begin{bmatrix} \hat{\mathbf{A}}t & 0 \\ 0 & \hat{\mathbf{D}}t^3 \end{bmatrix} \tag{4.14}$$

with:

$$\mathbf{Q} = \begin{bmatrix} \frac{E}{1-\nu^2} & \frac{\nu E}{1-\nu^2} & 0 \\ \frac{\nu E}{1-\nu^2} & \frac{E}{1-\nu^2} & 0 \\ 0 & 0 & G \end{bmatrix} \tag{4.15}$$

The evaluation of the stiffness matrix for a orthotropic plate requires some more steps but it is still the result of material properties and thickness combination. It is derived from the classical lamination theory, assuming the ply stiffness matrix already oriented in laminate coordinate system.

$$\begin{aligned} \mathbf{A} &= \textstyle\sum_{i=1}^{n_{ply}} \mathbf{Q}_i(z_i - z_{i-1}) \\ \mathbf{B} &= \tfrac{1}{2}\textstyle\sum_{i=1}^{n_{ply}} \mathbf{Q}_i(z_i^2 - z_{i-1}^2) \\ \mathbf{D} &= \tfrac{1}{3}\textstyle\sum_{i=1}^{n_{ply}} \mathbf{Q}_i(z_i^3 - z_{i-1}^3) \end{aligned} \tag{4.16}$$

The z_i terms can be substituted by their thickness percentage, taking the thickness outside the summation:

$$\begin{aligned} \mathbf{A} &= t\textstyle\sum_{i=1}^{n_{ply}} \mathbf{Q}_i(\%_i - \%_{i-1}) \\ \mathbf{B} &= \tfrac{t^2}{2}\textstyle\sum_{i=1}^{n_{ply}} \mathbf{Q}_i(\%_i^2 - \%_{i-1}^2) \\ \mathbf{D} &= \tfrac{t^3}{3}\textstyle\sum_{i=1}^{n_{ply}} \mathbf{Q}_i(\%_i^3 - \%_{i-1}^3) \end{aligned} \tag{4.17}$$

Following this approach, the laminate stiffness matrix becomes:

$$\mathbf{K} = \begin{bmatrix} \hat{\mathbf{A}}t & \hat{\mathbf{B}}t^2 \\ \hat{\mathbf{B}}^T t^2 & \hat{\mathbf{D}}t^3 \end{bmatrix} \tag{4.18}$$

In Eqs. (4.14) and (4.18) it is possible to see how, once fixed the material or stacking sequence, the stiffness matrix is function of the only thickness. If a symmetric or asymmetric cross section option is chosen (from Tab. 4.1), the laminate stiffness matrix is rotated of the prescribed amount through Eq. (4.19).

$$\mathbf{Q}_{rot} = \mathbf{R}^{-1}\mathbf{Q}_0\mathbf{R}^{-T} \tag{4.19}$$

Where

$$R = \begin{bmatrix} \cos^2\alpha & \sin^2\alpha & 2\sin\alpha\cos\alpha \\ \sin^2\alpha & \cos^2\alpha & -2\sin\alpha\cos\alpha \\ -\sin\alpha\cos\alpha & \sin\alpha\cos\alpha & \cos^2\alpha - \sin^2\alpha \end{bmatrix} \tag{4.20}$$

The evaluation of the plate stiffness matrix can be done before the optimization for unit thickness and during the optimization procedure the properties are updated and rotated if required.

4.2.6 Load transfer module

This module is not directly involved in the optimization loop, but it is used when the internal forces obtained with a stick model need to be applied to a detailed model or when an equivalent static load set is required.
The internal forces are computed with whichever NeoCASS solver and when dynamic solution are required it is possible to choose the internal forces computation method (direct recovery or force summation). Once known the internal forces distribution and the position of the FEM nodes, it is possible to compute for each stick model node a load set of 3 forces and 3 moments in global axis (Fx,Fy,Fz,Mx,My,Mz) that reproduces the internal forces distribution obtained with aero-elastic analyses, its working principle is qualitatively shown by Fig. 4.2. The computed load set is then written in Nastran format.
This procedure is helpful when a load condition obtained with an aeroelastic analysis on a stick model must be reproduced with a static analysis on a 3D model.

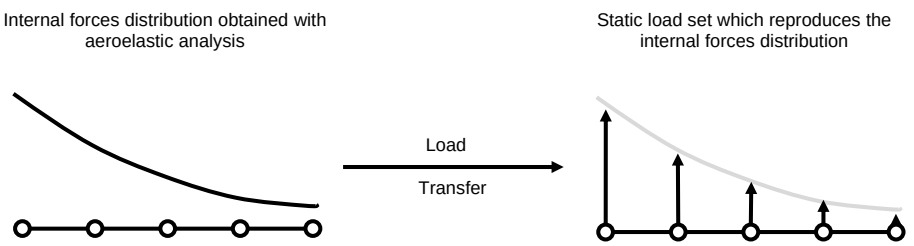

Figure 4.2: *Load Transfer module schematic representation*

Fig. 4.3 shows an application of this procedure to a B747-100 stick model: the internal forces obtained with a trim analysis are processed and the loads obtained are applied in a static analysis. The internal forces distribution of the two cases is equivalent.
This procedure becomes useful when the results of a dynamic aeroelastic condition, e.g. gust, must be transferred to a detailed model. The dynamic analysis of a 3D model is computationally burdensome specially if force summation is used to recover the loads, hence a fast and reliable strategy to obtain equivalent loads with a light stick model can reduce the analysis costs.

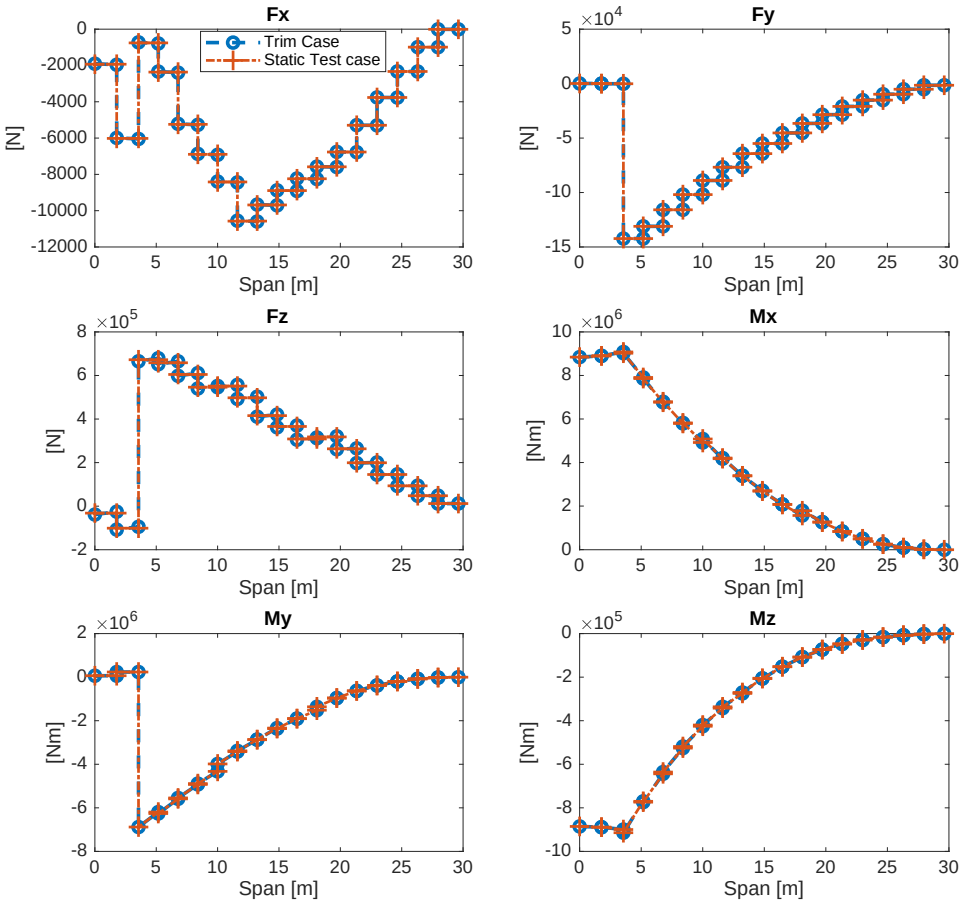

Figure 4.3: *Internal forces obtained with an elastic trim analysis (SOL144) vs. static analysis (SOL101), where the loads are computed through the load transfer module and applied statically.*

4.2.7 Procedure summary

Now all the element of the optimization framework are introduced, the following list summarizes the whole sizing procedure from the blank sheet to the 3D detailed model.

1. The aircarft is sized following the classical procedure of NeoCASS, hence the AcBuilder and GUESS module of fig. 2.2.

2. After the GUESS sizing the meta-model of the wingbox is defined and the stick model is updated with the properties computed by GUESS but processed by NeoANBA, this means that the stiffness matrices are not computed with analytical formulation and the wingbox match the shape

of the airfoil. A CAD and 3D FEM model with the initial properties is designed as well. Up to now the optimization is not stared yet but an improved description of the aircraft is already provided. The next steps are the core of the optimization procedure.

3. The cross section linking layout has to be specified, together with the spanwise patch subdivision.
4. If the materials are different from the one used by GUESS, they are assigned to the structural components e.g. the user provided stacking sequence.
5. The analyses used during the optimization are defined, if required the structure of the controller is assigned in terms of performance index, feedback measures, control input and eventual constraints.
6. The analyses required during the optimization performs a dummy run which produces the aerodynamic database which will not be modified during the optimization. At this stage all the information needed for the optimization are provided and the loop can start.
7. $\mathbf{X}_0$, the initial trial solution for the optimization problem is the result of the GUESS sizing.
8. NeoANBA translate geometrical, thickness and material information into stiffness and mass matrices, which are updated in the FE stick model of the aircraft.
9. If required, the active control is designed for the current aircraft model.
10. SMARTCAD performs the required analyses.
11. The internal loads obtained in the previous point are processed by NeoANBA, getting the stress state necessary for the structural constraints evaluation
12. objective function and constraints are evaluated by the optimization algorithm, providing the new value of the design variable $\mathbf{x}_{i+1}$.
13. step 8 to 11 are repeated until a stopping criteria is reached.
14. the wingbox 3D models and the stick one are updated with the latest value of $\mathbf{x}_i$

Fig. 4.4 conceptually shows the workflow of optimization loop.

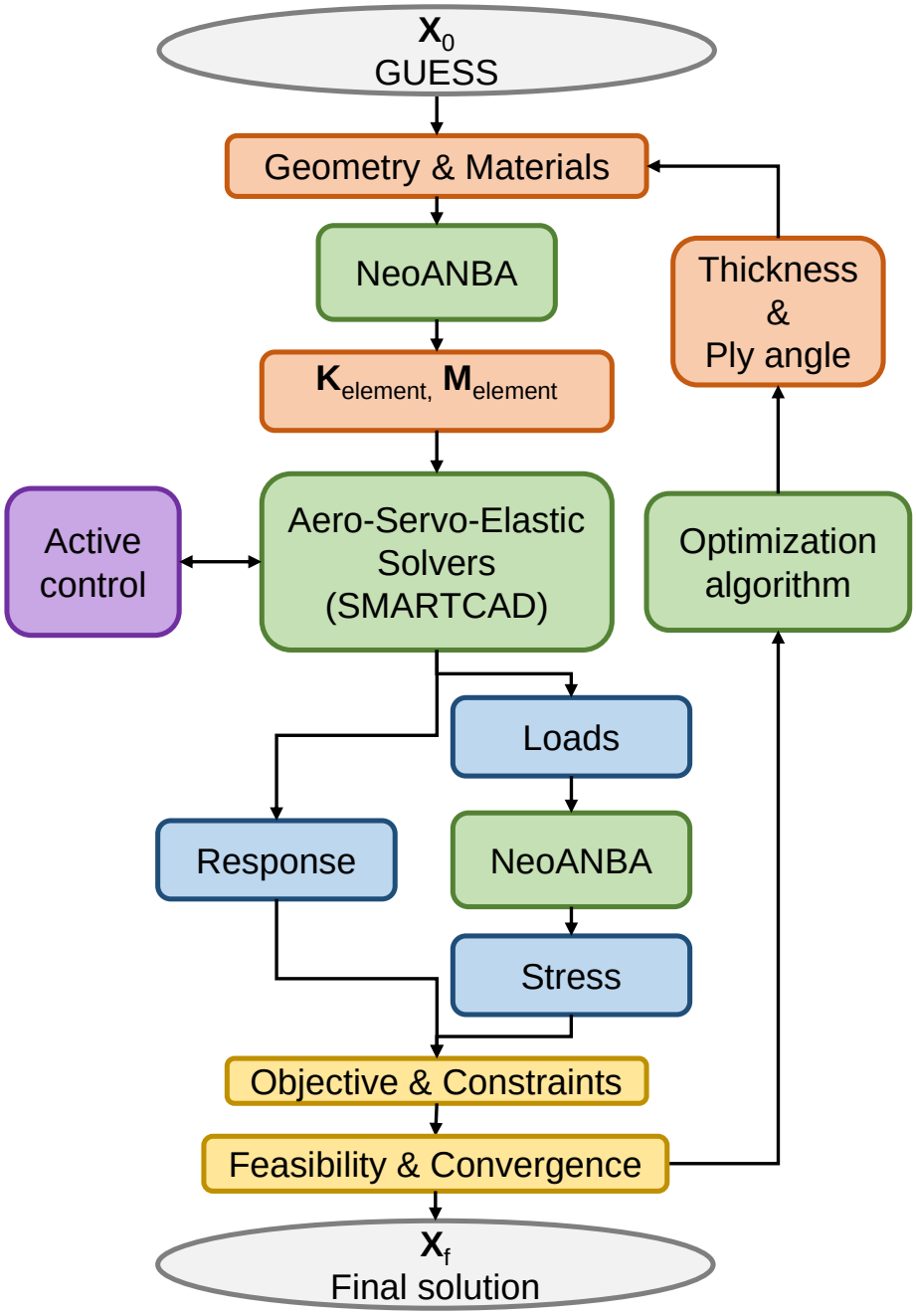

Figure 4.4: *NeOPT block diagram*

CHAPTER 5

Application of NeOPT for a trade-off study of a long haul aircraft

The aim of this chapter is to show an application of NeOPT, which is not the only possible exploitation of the procedure. In this particular case, the suite is exploited to understand how different kind of load envelope (trim, trim+gust, trim+gust+GLA), constraints sets (structural and flutter) and materials affects the structural sizing of the wingbox. The trade-off study is performed stretching the wing: the increase of the aspect ratio leads to a reduction of the induced drag and to an increase of the loads and of the wing mass, the trade-off objective is to understand which is aspect ratio which minimize the fuel burn on a given route.
As example a twin aisle long haul aircraft (TALH) is considered, the model is developed starting from the public available data of Airbus A330-300 aircraft of Fig. 5.1. Tab. 5.1 reports the general information of the aircraft, needed for the AcBuilder modelling and GUESS envelope computation.

The goal of this exercise is to perform trade-off studies by sizing the wingbox for different aspect ratios and fixed wing area, using different materials and cross section type. The optimization's objective is the wingbox structural

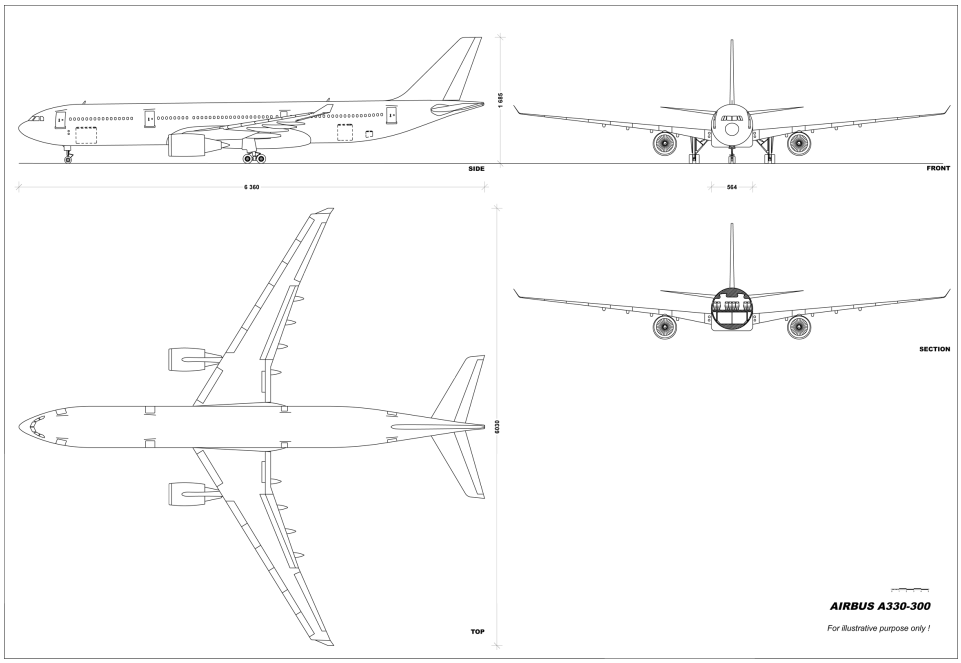

Figure 5.1: *A330-300 Tryptich [112]*

Table 5.1: *TALH general parameters*

Passengers	300
Wing Area	366.7 m^2
Aspect Ratio	9.17
Range	10200 km (5500Nm)
Max cruise altitude	13100m (43kft)
Max Operative Mach	0.87
Max Operating Speed (EAS)	175m/s (340 kt)
Cabin Altitude	2440m (8000ft)
TAS cruise 38kft	244.91m/s
EAS cruise	127.5m/s
Max CL TO	2.1
Max CL LND	2.5
Clean MAx CL	1.75
Clean CL slope	5.7/rad
Flap TO	15°
Flap LND	25°

mass while the constraints are the failure/buckling indexes of Sec. 4.2.3 for several load cases and the absence of flutter.
The information in Tab. 5.1 are used to model the aircraft in the AcBuilder

environment (Fig. 5.2a), producing the aeroelastic stick model which is sized running GUESS (Fig. 5.2b).

The manoeuvres used to size the aircraft are compliant with CS25 regula-

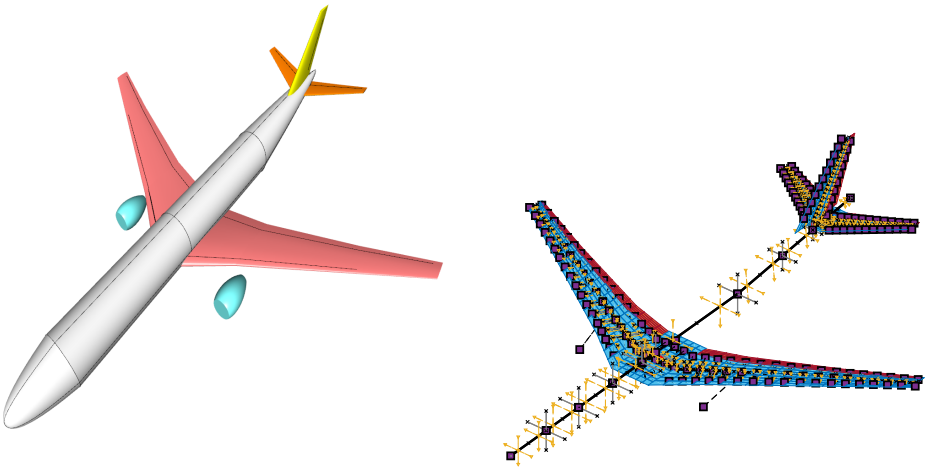

(a) *TALH ACBuilder model* **(b)** *TALH stick model*

Figure 5.2: *TALH models*

tion and are listed in Tab. 5.2: they are steady trim manoeuvre performed across the flight envelope of Fig. 5.3, mainly at sea level, corner point, cruise condition and maximum cruise Mach.

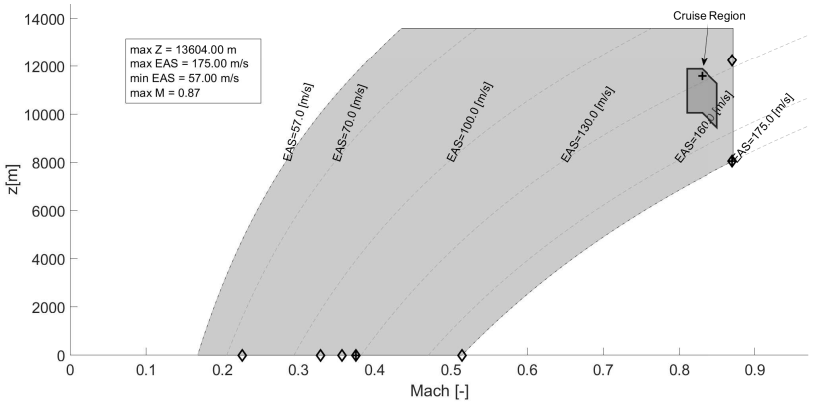

Figure 5.3: *TALH flight envelope, diamond markers are the manoeuvre points, plus markers are the 1g trim for gust*

Table 5.2: *TALH manoeuvre set definition for GUESS sizing based on CS25 requirements*

ID	Type	CS	N	z[m]	Mach	V
1	Pull-up	25.331	2,5	0	0,514	Max EAS VD Above corner point
2	Pull-up	25.331	2,5	8061	0,870	Max EAS Corner Point
3	Pull-up	25.331	2,5	0	0,375	Cruise sea level
4	Pull-up	25.331	2,5	12250	0,870	Cruise Max Mach
5	Push-down	25.331	-1,0	0	0,514	Max EAS above corer point
6	Push-down	25.331	-1,0	8061	0,870	Max EAS Corner Point
7	Push-down	25.331	-1,0	0	0,375	Cruise sea level
8	Push-down	25.331	-1,0	12250	0,870	Cruise Max Mach
9	Flap max down	25.345 a1	2,0	0	0,329	Cruise at VF= max(1,6 VFTO 1,8 VFLAND)
10	Static Gust for landing CONF	25.345 a2	1,0	0	0,329	Cruise at VF= max(1,6 VFTO 1,8 VFLAND)
11	Aft movement of pitch control at VA URDD5>0	25.331 b1	1,0	0	0,357	VA=sqrt(nmax)*VS
12	Aft movement of pitch control at VC URDD5>0	23.331 b1	1,0	0	0,375	VC
13	Aft movement of pitch control at VD URDD5>0	23.331 b1	1,0	0	0,514	VD
14	Aft movement of pitch control at VA URDD5<0	25.331 b1	1,0	0	0,357	VA=sqrt(nmax)*VS
15	Aft movement of pitch control at VC URDD5<0	23.331 b1	1,0	0	0,375	VC
16	Aft movement of pitch control at VD URDD5<0	23.331 b1	1,0	0	0,514	VD
17	Sideslipe max rudder >0	25.351 a	1,0	0	0,357	VA=sqrt(nmax)*VS
18	Sideslipe overswing >0	25.351 b	1,0	0	0,357	VA=sqrt(nmax)*VS
19	sideslipe manoeuvre 15° >0	25.351 c	1,0	0	0,357	VA=sqrt(nmax)*VS
20	Sideslipe max rudder >0	25.351 a	1,0	0	0,226	VS
21	Sideslipe overswing >0	25.351 b	1,0	0	0,226	VS
22	sideslipe manoeuvre 15° >0	25.351 c	1,0	0	0,226	VS
23	Sideslipe max rudder <0	25.351 a	1,0	0	0,357	VA=sqrt(nmax)*VS
24	Sideslipe overswing <0	25.351 b	1,0	0	0,357	VA=sqrt(nmax)*VS
25	sideslipe manoeuvre 15° <0	25.351 c	1,0	0	0,357	VA=sqrt(nmax)*VS
26	Sideslipe max rudder <0	25.351 a	1,0	0	0,226	VS
27	Sideslipe overswing <0	25.351 b	1,0	0	0,226	VS
28	sideslipe manoeuvre 15° <0	25.351 c	1,0	0	0,226	VS
29	Aileron abrupt maximum deflection at VA=sqrt(nmax) * VS >0	25.349	1,0	0	0,357	VA=sqrt(nmax)*VS
30	Aileron abrupt deflection + 2/3 max load factor >0	25.350	1,7	0	0,357	VA=sqrt(nmax)*VS
31	Aileron abrupt maximum deflection at VA=sqrt(nmax) * VS <0	25.349	1,0	0	0,357	VA=sqrt(nmax)*VS
32	Aileron abrupt deflection + 2/3 max load factor <0	25.350	1,7	0	0,357	VA=sqrt(nmax)*VS
33	Trim 1g for gust	gust	1,0	0	0,375	VC @ 0m
34	Trim 1g for gust	gust	1,0	11582	0,830	VC @ 38000ft
35	Trim 1g for gust	gust	1,0	8061	0,870	corner point

The GUESS's sizing provide a realistic mass and stiffness distribution which is used as starting point for the NeOPT optimization. This approach is used for each aspect ratio and cross section considered in order to have a common starting point for each configuration.
The first part of the chapter considers only trim manoeuvres and flutter constraints, evaluating how the range of the aircraft is affected by the parameters studied. In the second part it is considered the effects of dynamic load and active control on the structural sizing.

5.1 TALH family design with trim loads and flutter constraints

The baseline configuration has a span of 58m, to investigate how the structural mass is related to the aspect ratio, a family of aircraft with increasing span is sized with GUESS. The aspect ratio is modified keeping constant the wing surface and the chord ratio at a given span percentage. The wing span and aspect ratio considered are listed in Tab. 5.3, while their planar shape is illustrated in Fig 5.4. The wingboxes dimension are summarized in Tab. 5.4, which describes the position of the spars. For all the configuration the wing spars are straight and at the same chord percentage at root and

tip sections.

Table 5.3: *TALH family wing span and aspect ratio*

Span [m]	$\Lambda[-]$	Δ% Span	Δ% Λ
58	9.17	-	-
61	10.15	+5.17%	+10.69%
64	11.17	+10.34%	+21.81%
67	12.24	+15.51%	+33.48%

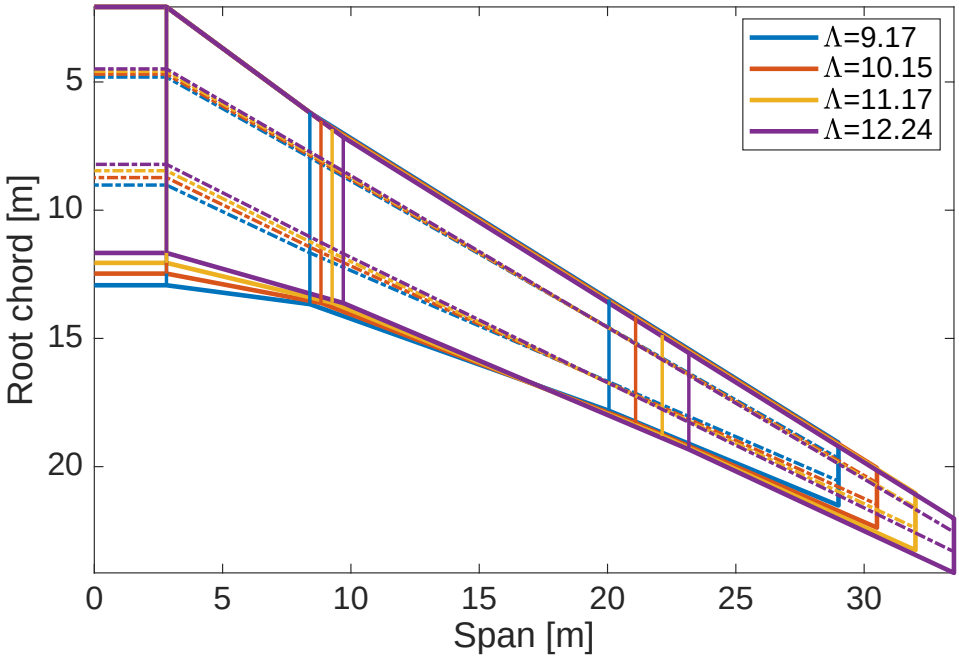

Figure 5.4: *TALH wing family*

Table 5.4: *Front spar (FS), rear spar (RS) and elastic axis (EA) positions in chordwise direction at wing root and tip*

$\Lambda[-]$	C Root [m]	C Tip [m]	FS Root C%	RS Root C%	FS Tip C%	RS Tip C%	EA Root C%	EA Root C%
9.17	12.556	2.448	25.2%	64.0%	25.0%	61.0%	44.6%	43.0%
10.15	11.939	2.328	25.2%	64.0%	25.0%	61.0%	44.6%	43.0%
11.17	11.379	2.219	25.2%	64.0%	25.0%	61.0%	44.6%	43.0%
12.24	10.870	2.120	25.2%	64.0%	25.0%	61.0%	44.6%	43.0%

During the optimization process, the design variables are spanwise linked. This means that in a prescribed region the thickness of structural elements

is constant. To be consistent among the TALH family wingboxes, 5 patches are chosen (Fig. 5.5): the first one covers the carry-through, the second one goes from the wing root to the engine connection and the three remaining patches are equally spaced along the span from the engine connection to the wing tip.

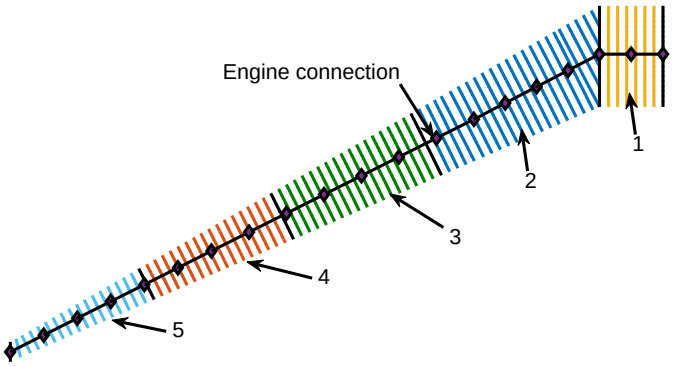

Figure 5.5: *TALH wing family patch subdivision*

To understand how the materials impact on the sizing, the wingbox is modelled with different materials (properties in Tab. 5.5) and cross section linking options.

- Aluminium wingbox, with both 7 and 10 cross section variables (ISO7 and ISO10).
- CFPR wingbox with stacking sequence of fig 5.6a, with both 7 and 10 cross section variables (COMP7 LAM1 and COMP10 LAM1).
- CFPR wingbox with stacking sequence of fig 5.6a, with 7 cross section variables and anti-symmetric ply orientation (design variable) between upper and lower skin (COMP7 LAM1 ASYM).
- CFPR wingbox with stacking sequence of fig 5.6b, with 7 cross section variables (COMP7 LAM2).

Table 5.5: *Materials properties*

	E11[GPa]	E22[GPa]	G12[GPa]	ν_{12}	$\rho[kg/m^3]$	$\sigma_{max}[MPa]$
AL7075T-6	72	72	27.69	0.3	2800	430
CFUD	135	10	5.00	0.3	1500	1500

The main difference between the two stacking sequences (LAM1 and LAM2) proposed is that the $90°$ oriented ply of Fig. 5.6a is oriented at $0°$ for the Fig. 5.6b.

The sizing is performed on a total of 28 aircraft configuration (4 span x 7

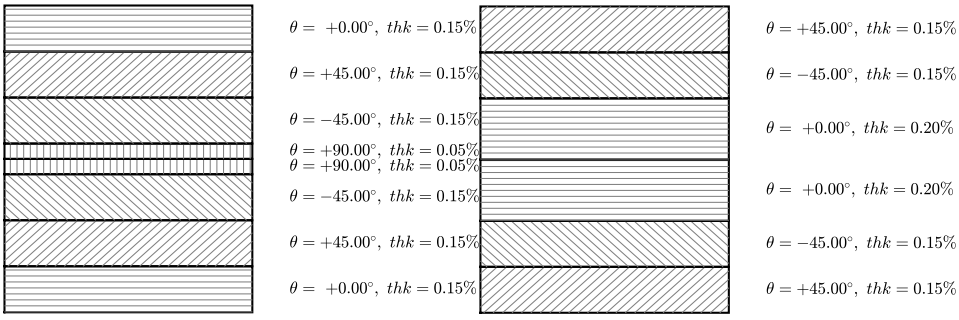

(a) *Stacking sequence 1 (LAM1)* **(b)** *Stacking sequence 2 (LAM2)*

Figure 5.6: *Stacking sequences considered for the TALH family*

section type) and the results are presented in the following.
For each configuration and for each manoeuvre it is available the contour plot of the stresses and failure indexes of the structural components, reporting the images of all the configurations would be dispersive, hence the results of just one case is shown by Fig. 5.7 as an example. It is possible to see how the optimizer produces a structures where it is used the minimum amount of material to withstand the loads, the stress level are close to the yielding for some component and the buckling becomes critical for others. Fig. 5.7 shows the results for a 2.5g pull-up and it is possible to see how the upper skins and stringers are compressed and more critical both for the buckling and failure, which appear when the failure index is negative ($FI < 0$).

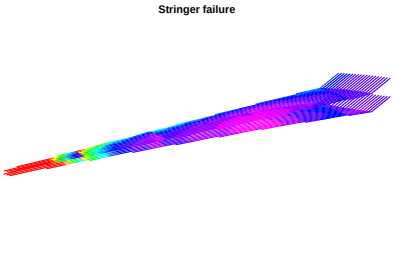

(a) *Stringer failure index*

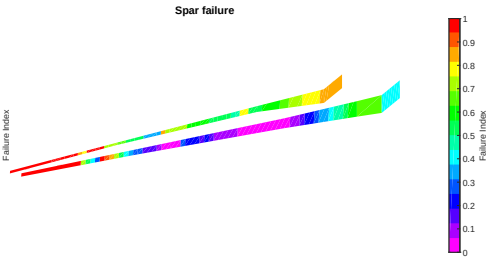

(b) *Spar failure index*

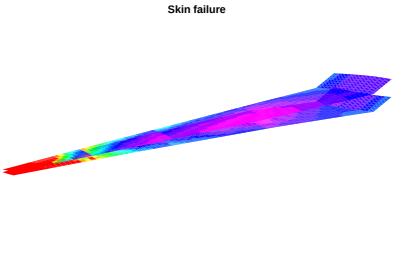

(c) *Skin failure index*

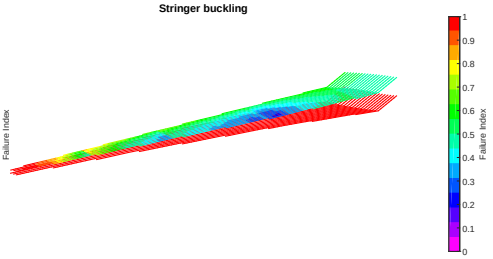

(d) *Stringer buckling index*

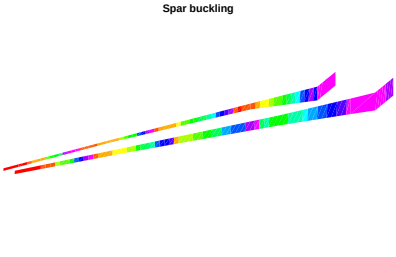

(e) *Spar buckling index*

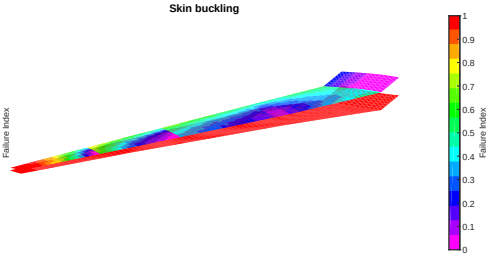

(f) *Skin buckling index*

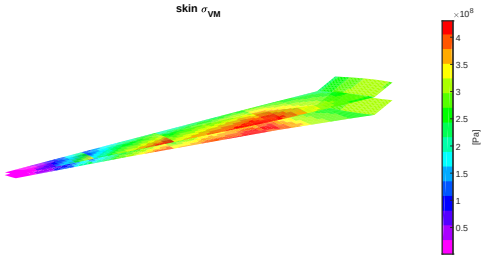

(g) *Skin Von Mises's stress*

Figure 5.7: *Results for TALH ISO7 and AR=9.71, manoeuvre 4*

The wingbox mass of the designed configurations is reported in Tab. 5.6 left. The results obtained are normalized with respect to the relative baseline ($\Lambda = 9.17$) values, in this way it is possible to compare the relative mass

increase for each cross section and material type, as reported in Tab. 5.7. The same results are graphically represented by Fig. 5.8 right.

Table 5.6: *TALH family wingbox mass (kg)*

Section	$\Lambda 9.17$	$\Lambda 10.15$	$\Lambda 11.17$	$\Lambda 12.24$
ISO7	9639.55	10597.44	11700.06	14200.62
ISO10	9553.53	10418.53	11421.95	13594.00
COMP7 LAM1	6957.19	7858.91	8778.49	10141.52
COMP10	6770.72	7696.46	8394.62	9751.75
COMP7 LAM1 ASYM	6815.47	7739.76	8357.02	9340.36
COMP7 LAM2	5352.07	5648.47	6081.51	7318.40

Table 5.7: *TALH family wingbox mass % variation w.r.t.* $\Lambda 9.17$ *mass*

Section	$\Lambda 9.17$	$\Lambda 10.15$	$\Lambda 11.17$	$\Lambda 12.24$
ISO7	-	9.94	21.38	47.32
ISO10	-	9.05	19.56	42.29
COMP7 LAM1	-	12.96	26.18	45.78
COMP10	-	13.67	23.98	44.03
COMP7 LAM1 ASYM	-	13.56	22.62	37.05
COMP7 LAM2	-	5.54	13.63	36.74

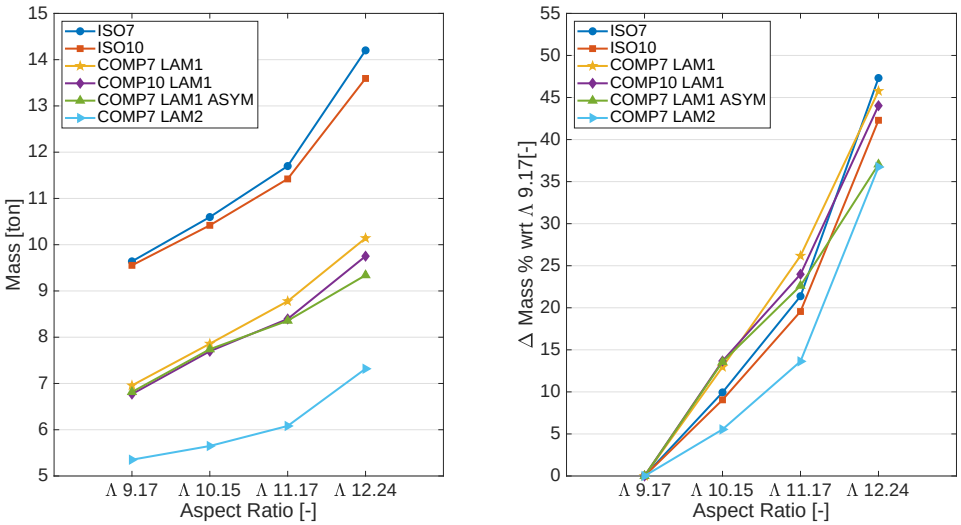

Figure 5.8: *TALH family wingbox mass*

In general, composites materials allows to design lighter wingboxes and the increase of design variables (ISO10 and COMP10) further reduce the structural mass. The introduction of laminate orientation variable (COMP7 LAM1 ASYM) generates a wash-out effect on the wing by orienting the the laminate fibres towards the leading edge and creating a bending-torsion coupling that produces a nose-down effect for an upward wing deflection. This kind of coupling is a well known passive load alleviation strategy [62]. The wash-out effect moves inboard the lift distribution, reducing the loads [20].
Fig. 5.8 shows how the mass evolution of the wingbox is clustered on the material adopted, three different families of curves are obtained for the three different materials. Despite the difference in the mass value obtained, the relative mass variation with respect to the reference condition is more uniform.

The results so far obtained quantify the mass increase due to the wing stretching, which worsen the structural efficiency of the Breguet's equation. From the same equation it is known that an aspect ratio increase improves the aerodynamic efficiency, it becomes a trade-off between the improvement of the aerodynamic term and the structural mass that we have to pay for it. The Breguet's equation is a simple and fast way to understand the trend and obtain qualitative results, it makes many simplification like constant aerodynamic forces and velocity, constant SFC, moreover the lift force is imposed equal to the weight of the aircraft and the drag is computed with linear method. To estimate the exact range detailed analyses should be done to calculate the right aerodynamic forces and a dedicated mission simulator should use these values to compute the exact fuel burn. It is not the intention of this work to provide the exact mission parameters, the range and fuel consumption are estimated with a rough method that can provide trends and comparative analyses, which are the goal in preliminary design phases.
To understand if and how much it is convenient to stretch the wing, the range is qualitatively computed with the Breguet's equation Eq. (5.1). The drag coefficient is decomposed on a constant term C_{D0} and an induced term C_{Di}.

$$R = \frac{V_{TAS}}{g}\left(\frac{C_L}{C_{D0}+C_{Di}}\right)\frac{1}{SFC}ln\frac{W_2+W_{fuel}}{W_2} \tag{5.1}$$

The parameters affected by the TALH family study case are the structural efficiency $ln\frac{W_2+W_{fuel}}{W_2}$, the mean lift coefficient $C_L = \frac{W_2+0.5W_{fuel}}{P_{dyn}S}$ and the aspect ratio Λ. W_2 is the weight of the sized aircraft at the end of the cruise,

during which it is assumed that all the fuel (80000 kg) is burnt. The C_{D0} is kept constant because the wetted surface of the aircraft does not change.
The induced drag term of the isolated wing is obtained with ALIS [113], a panel method which implements Morino's method and computes the induced drag using the Trefftz's plane.
The ranges of the studied configurations are presented in Fig 5.9, where the markers represent the range values for the aspect ratio considered and the dashed lines are a 2nd order fitting of the data obtained. The fittings provides an indication of the range trend increasing the AR.
It is possible to see how the maximization of the range is a trade-off between the aerodynamic efficiency improvement through the wing stretching and the consequent mass increase. The results obtained shows that the range assumes a bell shape that is function of the aspect ratio, the maximum position depends on the materials and the aspect ratio. Aluminium alloys wingboxes show a maximum range of 11576km with an aspect ratio around 12.3, composite materials reach higher values of range for higher aspect ratios, like 12637km with an AR of 12.8 for the LAM 2 case.
Excessive wing span increase leads to a change in the ICAO Aerodrome Reference Code (ARC) of the aircraft, in this case the threshold value is $\Lambda = 11.52$ that corresponds to 65m wingspan. Keeping the same ARC (E), it is possible to see that the span increment is always beneficial to the range and the emissions, further improvement can be reached with higher AR but it implies a change in the ARC code (from E to F) and this aspect must be considered in preliminary design phase.
The effect of aeroelastic tailoring is visible: the curves obtained for *COMP 7 LAM1* and *COMP 7 LAM1 ASYM* show the results obtained for the same stacking sequence but in the second case the asymmetric orientation of the skin panel is a design variable. The optimizer creates a bending-torsion term, known as wash-out, moving inboard the lift distribution and reducing the bending moment.

Results similar to the obtained in this section can be found in the work of Calderon [114], where despite of considering a different aircraft the relation between wing structural mass and aspect ratio is similar to the one illustrated in Fig 5.8 and the range-aspect ratio function has a shape similar to the one in Fig. 5.9.
The Breguet's Eq. 5.1 can be solved in function of the fuel mass for a fixed route (Eq. 5.2).

$$\frac{V_{TAS}}{g}\left(\frac{C_L(W_{fuel})}{C_{D0}+C_{Di}(C_L)}\right)\frac{1}{SFC}ln\frac{W_2+W_{fuel}}{W_2}-Range=0 \qquad (5.2)$$

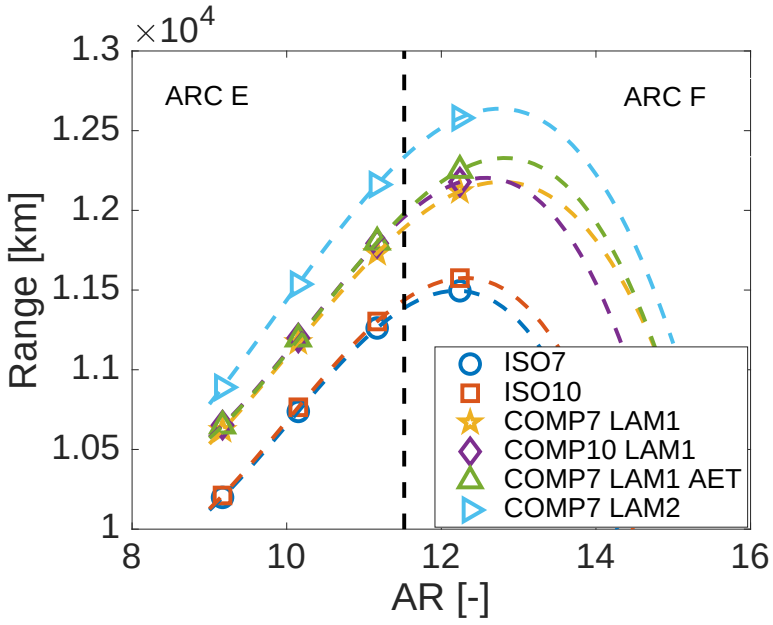

Figure 5.9: *TALH range trend*

Considering a 10000km route, the fuel burn trend for each configuration is reported in Fig. 5.10. Tab. 5.8 shows the fuel burn for the given haul and Tab. 5.9 indicates the fuel burn reduction achieved increasing the span. A reduction of about 7% in fuel burn and hence in the emission is achievable without exceeding the ARC E of the baseline configuration considering the same material, further reduction can be achieved but the class of the aircraft must be modified to ARC F.

The most promising solution is the *COMP7 LAM2* with an AR of 12.24,

Table 5.8: *TALH family fuel burn [ton] for a 10000km haul*

	$\Lambda = 9.17$	$\Lambda = 10.15$	$\Lambda = 11.17$	$\Lambda = 12.24$
ISO7	78.808	75.712	72.909	71.614
ISO10	78.737	75.571	72.706	71.238
COMP7 LAM1	76.431	73.456	70.661	68.735
COMP10 LAM1	76.261	73.324	70.380	68.472
COMP7 LAM1 AET	76.289	73.355	70.344	68.166
COMP7 LAM2	75.012	71.647	68.589	66.683

which has the lowest value of structural mass and fuel burn for the considered haul, the trend indicates that a possible improvement of the fuel consumption can be achieved increasing the AR to 12.8, leading to a 11.35%

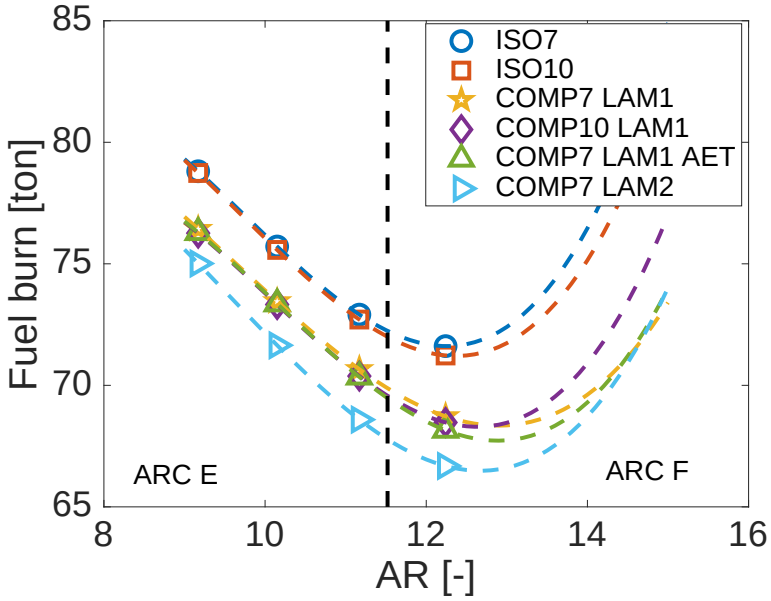

Figure 5.10: *TALH fuel burn trend*

Table 5.9: *TALH family fuel burn variation [%] w.r.t.* $\Lambda = 9.17$ *for a 10000km haul*

	$\Lambda = 9.17$	$\Lambda = 10.15$	$\Lambda = 11.17$	$\Lambda = 12.24$
ISO7	-	-3.928%	-7.485%	-9.129%
ISO10	-	-4.020%	-7.659%	-9.537%
COMP7 LAM1	-	-3.892%	-7.550%	-10.083%
COMP10 LAM1	-	-3.852%	-7.712%	-10.213%
COMP7 LAM1 AET	-	-3.846%	-7.793%	-10.661%
COMP7 LAM2	-	-4.486%	-8.563%	-11.105%

fuel reduction with respect to the baseline configuration sized with the same material. From an economical point of view saving 8530kg of fuel with a fuel cost of 60.7$/bbl (average fuel price for January 2021) corresponds to 4985$ saved for a 10000km route, considering the fully availability of the aircraft during the year and one travel per day, the total year saving is around 1.8 mln$ per year per aircraft.
Considering an emission factor of $9.75 kg CO_2/gall$ [115], the AR increase can avoid the emission of 30 tonnes of CO_2 for each flight, which becomes 10109 tonnes of CO_2 avoided per aircraft per year.
These value must be considered at fleet level e.g. 200 aircraft, considering always the same configuration, the CO_2 avoided in one year would be 2.02 millions of tonnes, which is equivalent to the yearly emission of an thermo-

electric power-plant natural gas fired [116] which supplies 1.8mln families for one year [1].
An article on Forbes Magazine [117] reports the request made by 9 EU governments to the European Commission to introduce additional measures to offset CO_2 emissions of planes. With an estimated carbon dioxide price of $75\$/tonCO_2$ the annual tax saved would be around 758k$ per aircraft.

Table 5.10: *TALH COMP7 LAM2 economical and environmental impact considering a 10000km haul*

Configuration	fuel burn per flight	fuel saving per flight	cost reduction per flight	CO_2 avoided per flight	cost reduction per AC per year	CO_2 avoided per AC per year
Baseline	75.01 ton	-	-	-	-	-
Extrapolation to AR 12.8	66.48 ton	8530 kg	4985$	27.7 ton	1.8mln$	10109 ton

5.2 TALH including gust loads and GLA

In this section one of the configurations studied in Sec. 5.1 is sized considering gust loads in addition to trim loads and flutter constraints. The aim of this section is to understand how the dynamic loads affect the structural sizing and which is the impact of active control technologies.
The configuration chosen for the sizing is the *COMP7 LAM1*.
The gust analyses are performed in two conditions, cruise at z=0m and z=11582m (condition 33 and 34 of Tab. 5.2). For each flight point (FP) 10 gust lengths are considered with positive and negative amplitudes, for a total of 20 gusts for each FP (Fig. 5.11 shows only the positive gusts and Tab. 5.11 reports the complete gust properties). The gust amplitude is computed following CS25.341 regulation and flight profile alleviation factor Fg is kept equal to 1 (conservative assumption), the gust gradients considered are 10 and they are equally spaced between 9m and 107m.
The dynamic loads are summed to the cruise 1g trim loads. For each gust 4 critical time instant are investigated to obtain correlated[2] enveloping loads: 1) maximum bending moment 2) minimum bending moment 3) maximum torsional moment 4) minimum torsional moment. The load set here described generates a total of 160 dynamic loads which are added to the 35 trim cases for structural constraints evaluation.
One of the most severe gust condition for the aircraft is the so called tuned gust, which is a gust with the frequency equal to the wing first bending mode.

[1] Considering a power-plant producing 5tWh and a average yearly consumption of 2700kWh for a 3-4 people
[2] Correlated is here used to identify the 6 internal forces acting at a given instant e.g. the 6 component of the internal forces when the maximum bending moment appears for a given section

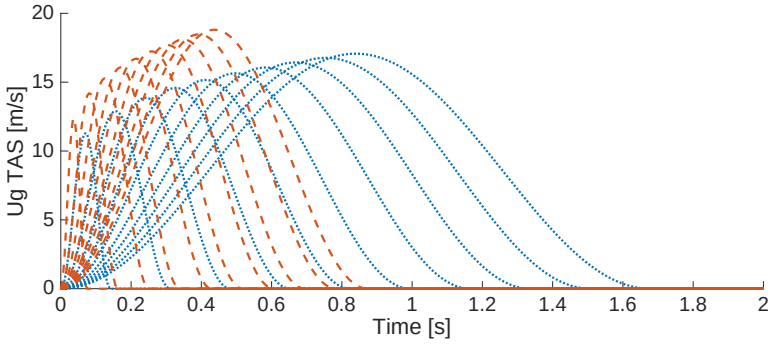

Figure 5.11: *TALH gust shapes: blue dotted lines for condition 33 and red dashed for condition 34*

Table 5.11: *Gust considered, 10 equally spaced gust gradient between H=9m and H=107m, positive and negtive, for two cruise condition*

H[m]	f(z=0m)[Hz]	V_g (z=0m)	f(z=11582m)[Hz]	V_g (z=11582m)
9.0	7.1	$\pm$11.30	3.6	$\pm$12.45
19.9	3.2	$\pm$12.90	6.2	$\pm$14.21
30.8	2.1	$\pm$13.87	4.0	$\pm$15.28
41.7	1.5	$\pm$14.59	2.9	$\pm$16.07
52.6	1.2	$\pm$15.16	2.3	$\pm$16.71
63.4	1.0	$\pm$15.65	1.9	$\pm$17.24
74.3	0.9	$\pm$16.06	1.6	$\pm$17.70
85.2	0.7	$\pm$16.43	1.4	$\pm$18.11
96.1	0.7	$\pm$16.77	1.3	$\pm$18.47
107.0	0.6	$\pm$17.07	1.1	$\pm$18.81

For the TALH family sized with GUESS, the first bending mode frequency is reported in Tab. 5.12 and it is in the range on 1.2-1.6 Hz, which is well covered by the gust at sea level and at cruise altitude.

Table 5.12: *TALH family first bending and torsional modes frequency*

	Span 58	Span 61	Span 64	Span 67
1st wing bending [Hz]	1.354	1.243	1.131	1.035
1st wing torsion [Hz]	3.166	3.090	2.773	2.614

The sizing is performed for all the aspect ratio considered in the previous section and both for open and closed loop configurations.
Starting from the development of Airbus A320, the regulation authority in-

troduced a dedicated appendix to the *Certification Specifications for Large Aeroplanes, CS25*, named *Interaction of system and Structures* [105]. This section states the possibility of considering actively reduced load envelope for the sizing and provides information about how to manage failures.
When the GLA controller is active, it is supposed that the controller and actuation never fails ($P_{fail} \leq 10E-9$) hence no failure condition is considered in the exercise.
The controller used for the GLA is synthesized following the procedure described in Chapter 3. The objective function is a combination of bending and torsional moment in two station spanwise: wing root and engine section.

$$f = \frac{max|WRBM_{CL}|}{max|WRBM_{OL}|} + \frac{max|WRTM_{CL}|}{max|WRTM_{OL}|} + \frac{max|ESBM_{CL}|}{max|ESBM_{OL}|} + \frac{max|ESTM_{CL}|}{max|ESTM_{OL}|} \tag{5.3}$$

To consider the effect of fast and slow gust, the objective function is evaluated for two gust, one at 0.3Hz and one at 5Hz, the objective function becomes $f = f_{0.3Hz} + f_{5Hz}$. This condition are used only to tune the controller, the dynamic load envelope is the one described in Tab. 5.11.
The measures used as feedback for the controller are the vertical acceleration and velocity of wing tips and CoG together with the pitch rate of the CoG.
The control surfaces used for the GLA are the ailerons deflected symmetrically and the elevator. This controller architecture leads to the structure of the gain matrix reported in Tab. 5.13: the command input is symmetrized for the two ailerons, the flexible modes are controlled with the ailerons while the elevator controls the pitch motion.
The constraints used during the controller design are the aero-servo-elastic

Table 5.13: *Gain matrix structure for the TALH GLA controller*

Actuator Input	Acc Wtip Rh	Vel Wtip Rh	Acc Wtip Lh	Vel Wtip Rh	Acc CoG	Vel Cog	Pitch rate
$\delta_{Aileron\ RH}$	x_1	x_2	x_1	x_2	x_3	x_4	x_5
$\delta_{Aileron\ LH}$	$-x_1$	$-x_2$	$-x_1$	$-x_2$	$-x_3$	$-x_4$	$-x_5$
$\delta_{Elevator}$	0	0	0	0	0	0	x_6

stability of the elastic modes and a rate saturation of 100[deg/s] for the control surfaces.
The results of the sizing are illustrated in Fig. 5.12, where it is possible to see that there are not relevant mass increment with respect the trim con-

dition. The open loop configuration has a slight increment of the structural mass ($\leq 1\%$) while the closed loop configuration has the same mass of the sizing performed with trim loads and flutter constraints.

For the aircraft family considered, the trim loads are more critical than the

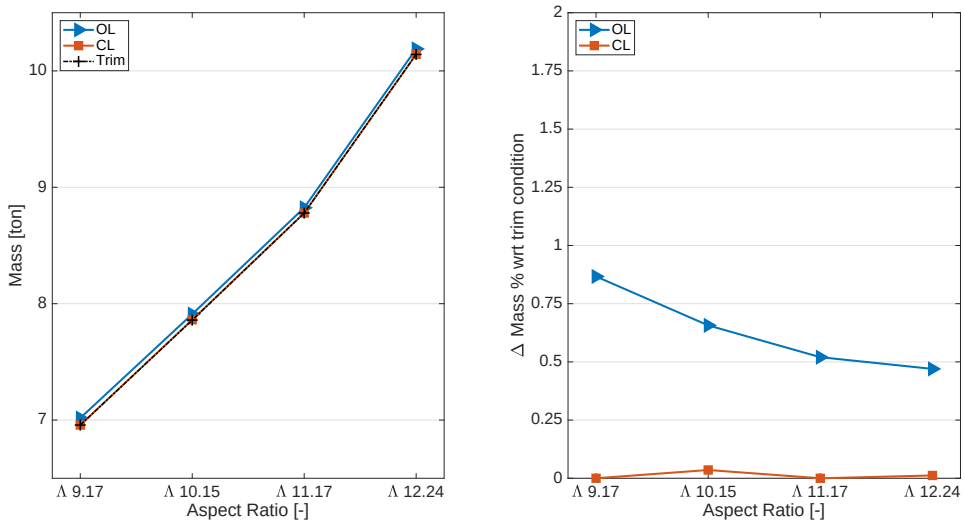

Figure 5.12: *TALH wingbox mass considering gust loads and active control*

dynamic ones, an indication of that is provided by Fig. 5.13 where the bending/torque envelope of the wing root and engine sections are reported. For both the sections the pull-up (top right area) and push-down (bottom left area) manoeuvres are the most critical from the structural point of view.
The effect of the GLA does not affect significantly the root load envelope (Fig. 5.13a), where the trim loads are dominant. The active control effect is more relevant for outboard sections (Fig. 5.13b), where the envelope is reduced by the controller but the sizing cases are still trim loads.

In general the controller reduces both torsional and bending moment dynamic envelopes. This effect is visible in Fig. 5.13, which shows how the loads are reduced when the GLA is active (orange vs. green envelope).
Fig. 5.14 shows the wing root and engine section bending and torsional moment time history for three gust gradient, both for open and closed loop: the controller reduces both bending and torsional loads in an efficient way, without requiring more than $10°$ of deflection and without exceeding the saturation speed of $100°/s$, as Fig. 5.15 shows.

Since the aircraft family considered in the exercise is not sized by gust loads, the GLA controller does not provide mass saving, it is beneficial from other point of view (e.g. fatigue) and it will be discussed in the following.

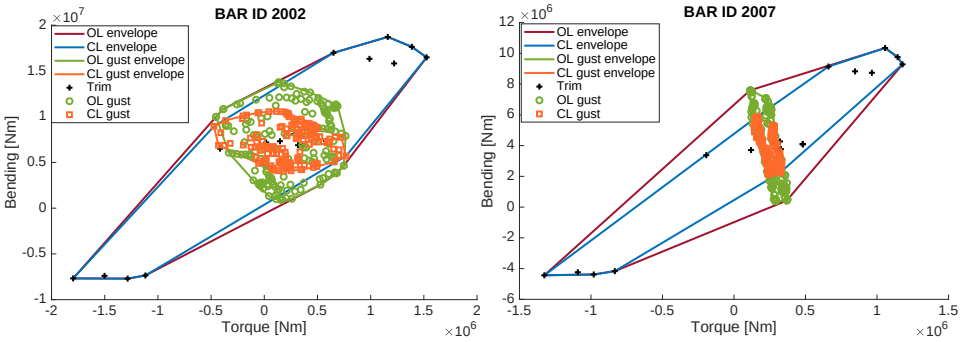

(a) *Wing root BM/TM envelope (nominal loads)* **(b)** *Engine section BM/TM envelope (nominal loads)*

Figure 5.13: *Wing root and engine section BM/TM envelopes*

Since the sizing loads come from manoeuvre condition, an manoeuvre load alleviation (MLA) controller can provide significant mass saving. MLA autotuning for the NeOPT procedure is not yet available (see future works in Chap. 6), but it effect can be considered using different safety factor for the ultimate load computation. Following the assumption made for the GLA controller ($P_{fail} \leq 10E-9$), it is possible to scale the entire load envelope of a provided factor an evaluate the impact of an hypothetical MLA controller on the sizing, in this case two saftey factor lower than 1.5 are used to simulate the MLA, driving to the load envelope reduction reported in Tab. 5.14 For this reason another sizing loop of the baseline COMP7 LAM1 configura-

Table 5.14: *Load reduction considered for the hypothetical MLA*

safety factor	SF=1.5	SF=1.4	SF=1.3
load reduction	0	-6.67%	-13.33%

tion is performed considering SF=1.4 and SF=1.3 for trim loads and 1.5 for gust loads (already reduced by GLA). The failure rates of the actuators and controller is 0 and the exercise aims to discover the theoretical mass saving achievable with a foolproof controller.
Fig. 5.16 shows how the load envelope is modified considering different safety factor, the top-right and bottom-left corners (associated to pull-up and push-down manoeuvres) are squeezed while other corner points of the envelope, mainly due to dynamic gust, have smaller variation.
The results in terms of mass variation, fuel burn and CO_2 emissions are reported in Tab. 5.15. With lower safety factor the designed wingbox is lighter,

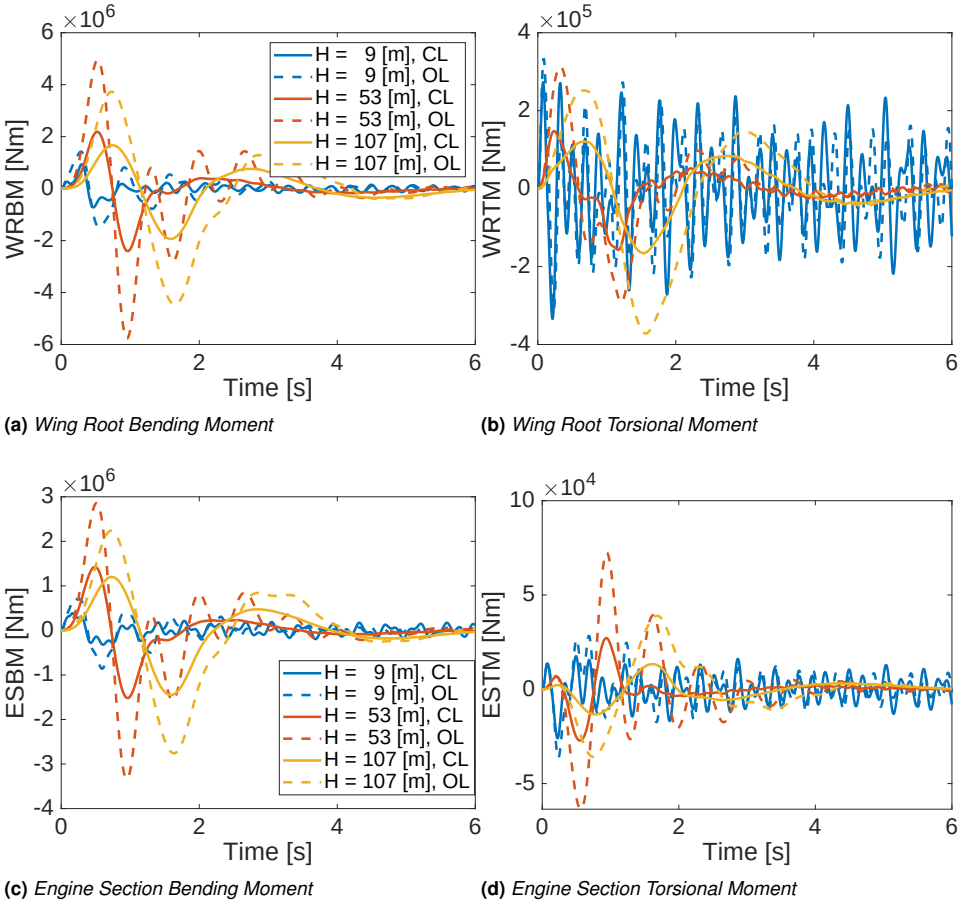

(a) *Wing Root Bending Moment*

(b) *Wing Root Torsional Moment*

(c) *Engine Section Bending Moment*

(d) *Engine Section Torsional Moment*

Figure 5.14: *Control performance comparison in close and open loop*

this translated in a range extension (+ 1% with SF=1.3) and a reduction of fuel burn and CO_2 emission of 0.8%. Despite the improvements obtained seems low, they must always be considered in terms of life-cycle fleet management, with and operative live of 40 years a single aircraft equipped with GLA/MLA could save up to 30000 tonnes of CO_2.

Another benefit introduced by an active controller and not yet considered is its impact on the continuous turbulence response. Turbulence may affect the sizing of the aircraft in terms of fatigue and passenger comfort. If the first aspect is more relevant from a structural point of view, the flight quality is more related to the marketing side of passengers' flight experience and their safety.

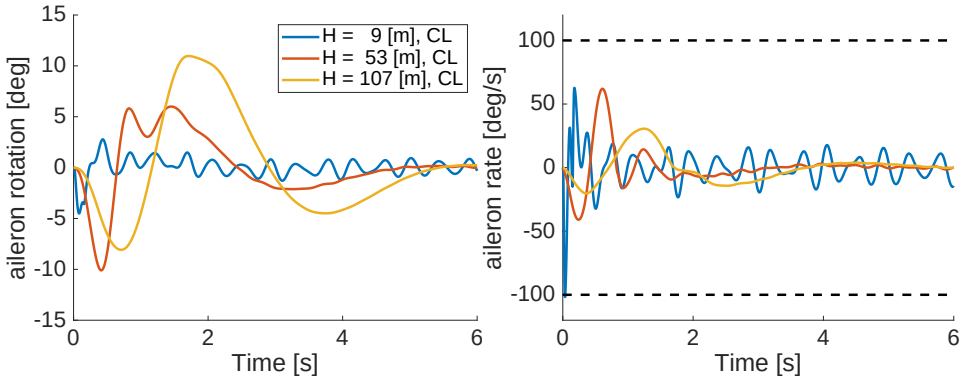

(a) *Aileron deflection* **(b)** *Aileron rotation rate*

Figure 5.15: *Control surface deflection and deflection rate applied by the GLA controller*

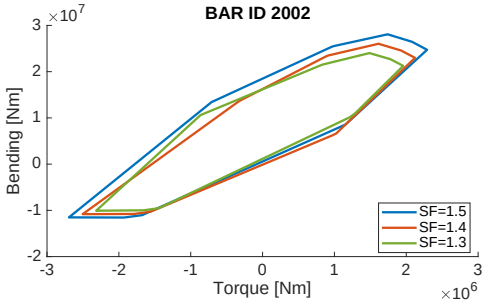

Figure 5.16: *Baseline COMP7 LAM1 ultimate loads envelope reduction due to different safety margin.*

Table 5.15: *Performances variation due to different safety factor for trim loads (reference haul 10000km)*

	SF=1.5	SF=1.4	SF=1.3
Mass[kg]	6957.19	6537.67	6182.52
Δ mass w.r.t. SF 1.5 [%]	-	-6.03%	-11.13%
Range [km]	10625	10693	10751
Δ range w.r.t. SF 1.5 [%]	-	0.63%	1.18%
Fuel burn [ton]	76.409	76.047	75.734
Fuel saved [kg]	-	361.73	674.59
Money saved per flight	-	172.19$	321.81$
Money saved per year per AC	-	62849$	117460$
CO_2 avoided per flight [kg]	-	1163.7	2174.7
CO_2 avoided per year per AC [ton]	-	424.75	793.8

To understand the behaviour of the aircraft when encounters turbulence, the model is excited with a continuous turbulence obtained filtering a normally distributed random signal through a filter which approximates the Dryden turbulence spectrum [118] [119].
Fig. 5.17a shows the comparison of the wing root bending moment power spectral density in open and closed loop and it is possible to see that the controlled aircraft has lower and more damped peaks. Practically, it translates into lower stress spectra extending the life of the wing components and reducing the maintenance, increasing the operability of the aircraft.
The effect of the GLA controller on the centre of gravity acceleration is depicted in Fig. 5.17b, where the acceleration PSD peaks are reduced. From

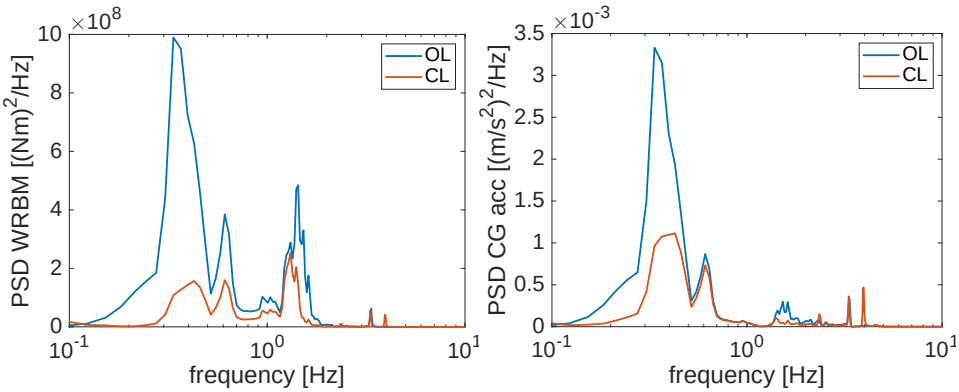

(a) *WRBM PSD comparison* **(b)** *CoG vertical acceleration PSD comparison*

Figure 5.17: *Open and closed loop PSD of CG acceleration and WRBM*

the passengers and cabin crew point of view, the reduction of the acceleration due to the turbulence improves the flight experience and the safety. Moreover GLA controller reduces the effects of discrete gust, mitigating abrupt aircraft movements which could injury the people onboard.
A recent investigative report [120] illustrate that one of the effects of the CO_2 emissions is the increase of clear-air turbulence [121], with a 15% increase in vertical airspeed variation in the North Atlantic jet stream since 1979 [122]. From 1980 through 2008 (28 years), U.S. air carriers had 234 turbulence accidents, resulting in 298 serious injuries (184 involved flight attendants and 114 involved passengers) and three fatalities [123]. The occurrences increased significantly between 2009 and 2018 with 340 injured people in 10 years [124].
Gust load alleviation has a double effect: on one hand it helps to reduce the CO_2 emissions by improving the structural efficiency, on the other hand it

mitigates the effects of clear-air turbulence by alleviating the accelerations. Anyway, the safest way to avoid injuries is to sit down and buckle up, paying attention to the cabin crew recommendations.

CHAPTER 6

Conclusions

The work presented in this thesis covers several disciplines, making a step-forward in the aero-servo-elastic capabilities available at the conceptual design level.

The analytical description of the wingbox through the meta-model allows to create a set of analytical information which can be easily transformed in analysis inputs or can post-process analysis results. Thanks to its pivotal position in the NeOPT framework, the meta-model easily maps each property of the wingbox on the available models (stick, cross section, 3D FEM and CAD) keeping them coherent and update. This means that whichever modification to whichever model is automatically reflected in all the models. This helps the designer avoiding re-meshing and model updating when modification are applied, reducing the pre-processing time and the possible error while transferring the properties among the models.

The fidelity of the structural model used to describe the aircraft in this phases (stick model) is increased by the implementation of a cross-section modeller(NeoANBA) that provides a better description of the mass and stiffness properties of the wingbox. The method is general and can be extended

to whichever hollow section that can be described through a beam, for example to the fuselage. NeoANBA provides a punctual description of the stress state of the section starting from the internal forces distribution of the stick model. The solver allows to to consider multiple spar and composite sections, computing the coupling terms of the stiffness matrix.
The advantage in following this procedure is that results typically obtained with detailed and computationally burdensome 3D FEM model can be reproduced with light stick model suitable for aero-servo-elastic analysis. The better description of the aeroelastic behaviour of the aircraft allows the designer to consider in the proper way high performance materials since early design phases, reducing the uncertainty on the model and exploring new design solution and concepts.

In the last years active control assumed a relevant role in aircraft design, both for stability augmentation and for load reduction. In this thesis the two aspects are considered together since the conceptual design phases exploiting a simple and user friendly control law design approach that allows the conceptual study office to consider the controller effect since the beginning of the project. Often the people involved in this phases are not expert in control theory, hence the user-friendly and sound procedure proposed help them to develop robust controller with simple layout that helps to understand the potential impact of active technology on the structural sizing.

NeOPT considers the improved beam model together with the possibility of performing aero-servo-elastic analyses in the sizing procedure, running an optimization with the three main aeroelastic solver available (trim, dynamic response and flutter). The results is a wingbox compliant with CS25 regulation in terms of load and trim envelopes. The possibility of including GLA/MLA provides the estimation of structural mass saving with active control. Since the optimizer and the solvers are implemented in the same environment, NeOPT can use whichever analysis response as objective function or constraint, making the framework flexible and adaptable to other optimization problems.

The final chapter provides an example of NeOPT's capability, showing how the modification of geometrical parameters and different materials affect the performances of the aircraft.
The preliminary evaluation of fuel burn reduction shows how the adoption of a blend of active (GLA) and passive (AET) technologies could limits the pollutant emission and cut the operative costs of an new generation aircraft

al fleet level.

Future works and recommendation

The work is mainly focused on the aero-servo-elastic optimization of the wingbox, but the procedure is suitable to be extended to all the components that can be represented with a beam elements (fuselage, tail planes). NeOPT can be exploited by other engineering disciplines which requires the optimization of a beam element that represents an hollow section.
Current implementation considers only trim and gust load, a future extension of the tool could consider dynamic landing, control surfaces dynamic manoeuvres, taxi loads and fatigue for the sizing. Moreover, the possibility of analysing multiple mass configuration would allow to size in a more general way the wingbox, which currently is optimized for a single mass configuration.
To provide a more realistic implementation of the control systems (AFS, MLA, GLA) a unified formulation should be proposed to optimize the MLA controller as well as the GLA controller, considering in the proper way the failure using realistic values for the time of occurrence (ToC) and continuation of flight (CoF).
NeoANBA can be improved by enriching its elements library so it can describe whichever kind of section e.g. helicopter or wind turbine blades, extending its analysis ability.
At the moment it is under development the implementation of shell elements in NeoCASS, which could open the possibility of performing the optimization by applying the loads to a full 3D model through the load transfer module.
In the future it could be possible to perform a sizing considering continuous leading and trailing edge morphing device for MLA/GLA, improving the alleviation capability by using bigger distributed surfaces. This kind of effect is achievable using morphing structures which could improve the aircraft performances by substituting the conventional high lift devices with smaller one, addressing the design of the wing in the direction of a fully electric and morphable structure that adapt to each flight condition reducing the fuel burn.
A better estimation of the aerodynamic derivatives, possibly using higher fidelity tool like ALIS for the full aircraft, together with a mission profile optimization and simulation tool could provide a quantitative evaluation of the fuel burn, CO_2 emission and fuel-related operative costs of the aircraft which could be used directly as objective function during the optimization.

Bibliography

[1] E. Mazareanu, "Size of aircraft fleets by region worldwide in 2019 and 2039." https://www.statista.com/statistics/262971/aircraft-fleets-by-region-worldwide, 2019.

[2] H. Tabuchi, "Worse than anyone expected: Air travel emissions vastly outpace predictions." https://www.nytimes.com/2019/09/19/climate/air-travel-emissions.html, 2019.

[3] "Aircraft Technology Roadmap to 2050." https://www.iata.org/contentassets/8d19e716636a47c184e7221c77563c93/technology20roadmap20to20205020no20foreword.pdf.

[4] E. Commision, "Flightpath 2050 europe's vision for aviation." https://ec.europa.eu/transport/sites/transport/files/modes/air/doc/flightpath2050.pdf, 2011.

[5] A. Kharina and D. Rutherford, "Fuel efficiency trends for new commercial jet aircraft: 1960 to 2014," 2015.

[6] A. Jameson, "Re-engineering the design process through computation," *Journal of Aircraft*, vol. 36, no. 1, pp. 36–50, 1999.

[7] W. G. Roeseler, B. Sarh, M. U. Kismarton, J. Quinlivan, J. Sutter, and D. Roberts, "Composite structures: the first 100 years," in *16th International Conference on Composite Materials*, pp. 1–41, Japan Society for Composite Materials Kyoto, Japan, 2007.

[8] R. H. Liebeck, "Design of the blended wing body subsonic transport," *Journal of aircraft*, vol. 41, no. 1, pp. 10–25, 2004.

[9] Z. Lyu and J. R. Martins, "Aerodynamic design optimization studies of a blended-wing-body aircraft," *Journal of Aircraft*, vol. 51, no. 5, pp. 1604–1617, 2014.

[10] W. Su and C. E. Cesnik, "Nonlinear aeroelasticity of a very flexible blended-wing-body aircraft," *Journal of Aircraft*, vol. 47, no. 5, pp. 1539–1553, 2010.

[11] R. Jansen, C. Bowman, A. Jankovsky, R. Dyson, and J. Felder, "Overview of nasa electrified aircraft propulsion (eap) research for large subsonic transports," in *53rd AIAA/SAE/ASEE Joint Propulsion Conference*, p. 4701, 2017.

[12] T. Delft, "Flying v." https://www.tudelft.nl/en/ae/flying-v/.

[13] A. Frediani, V. Cipolla, and E. Rizzo, "The prandtlplane configuration: overview on possible applications to civil aviation," *Variational Analysis and Aerospace Engineering: Mathematical Challenges for Aerospace Design*, pp. 179–210, 2012.

[14] R. Cavallaro, R. Bombardieri, L. Demasi, and A. Iannelli, "Prandtlplane joined wing: Body freedom flutter, limit cycle oscillation and freeplay studies," *Journal of Fluids and Structures*, vol. 59, pp. 57–84, 2015.

[15] G. B. M. of Aviation and G. B. M. of Aviation. Accidents Investigation Branch, *Civil Aircraft Accident: Report on the Accident to B.A.C. One-Eleven G-ASHG at Cratt Hill, Near Chicklade, Wiltshire on 22nd October, 1963*. CAP (Series), H.M. Stationery Office, 1965.

[16] R. Hall, R. Biedron, D. Ball, D. Bogue, J. Chung, B. Green, M. Grismer, G. Brooks, and J. Chambers, "Computational methods for stability and control (comsac): the time has come," in *AIAA Atmospheric Flight Mechanics Conference and Exhibit*, p. 6121, 2005.

[17] E. Livne, "Aircraft active flutter suppression: State of the art and technology maturation needs," *Journal of Aircraft*, vol. 55, no. 1, pp. 410–452, 2018.

[18] D. Raymer, *Aircraft design: a conceptual approach*. American Institute of Aeronautics and Astronautics, Inc., 2012.

[19] E. Torenbeek, *Synthesis of subsonic airplane design: an introduction to the preliminary design of subsonic general aviation and transport aircraft, with emphasis on layout, aerodynamic design, propulsion and performance*. Springer Science & Business Media, 2013.

[20] C. V. Jutte and B. K. Stanford, *Aeroelastic tailoring of transport aircraft wings: state-of-the-art and potential enabling technologies*. National Aeronautics and Space Administration, Langley Research Center, 2014.

[21] L. Cavagna, S. Ricci, and L. Travaglini, "Neocass: an integrated tool for structural sizing, aeroelastic analysis and mdo at conceptual design level," *Progress in Aerospace Sciences*, vol. 47, no. 8, pp. 621–635, 2011.

[22] L. Cavagna, S. Ricci, and L. Travaglini, "Structural sizing and aeroelastic optimization in aircraft conceptual design using neocass suite," in *13th AIAA/ISSMO Multidisciplinary Analysis Optimization Conference*, p. 9076, 2010.

[23] L. Cavagna, S. Ricci, and L. Riccobene, "A fast tool for structural sizing, aeroelastic analysis and optimization in aircraft conceptual design," in *50th AIAA/ASME/ASCE/AHS/ASC Structures, Structural Dynamics, and Materials Conference 17th AIAA/ASME/AHS Adaptive Structures Conference 11th AIAA No*, p. 2571, 2009.

[24] L. Cavagna, S. Ricci, and L. Riccobene, "Structural sizing, aeroelastic analysis, and optimization in aircraft conceptual design," *Journal of Aircraft*, vol. 48, no. 6, pp. 1840–1855, 2011.

[25] N. Werter and R. De Breuker, "A novel dynamic aeroelastic framework for aeroelastic tailoring and structural optimisation," *Composite Structures*, vol. 158, pp. 369–386, 2016.

[26] P. Piperni, A. DeBlois, and R. Henderson, "Development of a multilevel multidisciplinary-optimization capability for an industrial environment," *AIAA journal*, vol. 51, no. 10, pp. 2335–2352, 2013.

[27] B. A. Autry and D. Victorazzo, "Automated top level aircraft structural sizing tool (atlass): A framework for preliminary aircraft design and optimization," in *AIAA Scitech 2019 Forum*, p. 0550, 2019.

[28] A. Elham, "Weight indexing for multidisciplinary design optimization of lifting surfaces," 2013.

[29] W. P. Rodden and E. H. Johnson, *MSC/NASTRAN aeroelastic analysis: user's guide; Version 68*. MacNeal-Schwendler Corporation, 1994.

[30] M. Nastran *et al.*, "Quick reference guide," *MSC. SOFTWARE*, vol. 1, 2004.

[31] T. Melin, "Tornado, a vlm with structural modelling for conceptual aircraft design," in *RAeS Aerodynamics Conference 2010*, RAeS, 2010.

[32] P. Mantegazza and C. Cardani, "Continuation and direct solution of the flutter equation," *Computers & Structures*, pp. 185–192, 1978.

[33] M. Ripepi and P. Mantegazza, "Improved matrix fraction approximation of aerodynamic transfer matrices," *AIAA journal*, vol. 51, no. 5, pp. 1156–1173, 2013.

[34] G. L. Ghiringhelli, P. Masarati, and P. Mantegazza, "Multibody implementation of finite volume c beams," *AIAA journal*, vol. 38, no. 1, pp. 131–138, 2000.

[35] V. Giavotto, *Strutture Aeronautiche*. CLUP, 1977.

[36] G. Bindolino, G. Ghiringhelli, S. Ricci, and M. Terraneo, "Multilevel structural optimization for preliminary wing-box weight estimation," *Journal of Aircraft*, vol. 47, no. 2, pp. 475–489, 2010.

[37] T. Möller, "A fast triangle-triangle intersection test," *Journal of graphics tools*, vol. 2, no. 2, pp. 25–30, 1997.

[38] J. Tuszynski, "Surface intersection." `https://www.mathworks.com/matlabcentral/fileexchange/48613-surface-intersection`, 2020.

[39] L. Piegl and W. Tiller, *The NURBS book*. Springer Science & Business Media, 1996.

[40] T. J. Hughes, J. A. Cottrell, and Y. Bazilevs, "Isogeometric analysis: Cad, finite elements, nurbs, exact geometry and mesh refinement," *Computer methods in applied mechanics and engineering*, vol. 194, no. 39-41, pp. 4135–4195, 2005.

[41] J. A. Cottrell, T. J. Hughes, and Y. Bazilevs, *Isogeometric analysis: toward integration of CAD and FEA*. John Wiley & Sons, 2009.

[42] P. Mantegazza, "Analysis of semimonocoque beam sections by the displacement method," *L'Aerotecnica, missili e spazio*, no. 4, pp. 179–182, 1977.

[43] V. Giavotto, M. Borri, P. Mantegazza, G. Ghiringhelli, V. Carmaschi, G. Maffioli, and F. Mussi, "Anisotropic beam theory and applications," *Computers & Structures*, vol. 16, no. 1-4, pp. 403–413, 1983.

[44] C. D. Regan and C. V. Jutte, "Survey of applications of active control technology for gust alleviation and new challenges for lighter-weight aircraft," 2012.

[45] N. Harpur, "The effect of active control systems on structural design criteria," *AGARD Active Control Systems for Load Alleviation, Flutter Suppression and Ride Control p 11-22(SEE N 74-25550 15-02)*, 1974.

[46] M. Reyes, H. Climent, M. Karpel, F. Arevalo, and C. Maderuelo, "Increased-order aeroservoelastic modeling in practice," in *Proceedings of the International Forum on Aeroelasticity and Structural Dynamics*, pp. 2017–165, 2017.

[47] M. Ripepi, *Model order reduction for computational aeroelasticity*. PhD thesis, Italy, 2014.

[48] V. L. Syrmos, C. T. Abdallah, P. Dorato, and K. Grigoriadis, "Static output feedback-a survey," *Automatica*, vol. 33, no. 2, pp. 125–137, 1997.

[49] S. Boyd, C. Baratt, and S. Norman, "Linear controller design: Limits of performance via convex optimization," *Proceedings of the IEEE*, vol. 78, no. 3, pp. 529–574, 1990.

[50] S. Bingulac, N. Cuk, and M. Calovic, "Calculation of optimum feedback gains for output-constrained regulators," *IEEE Transactions on Automatic Control*, vol. 20, no. 1, pp. 164–166, 1975.

[51] E. G. Collins Jr, W. M. Haddad, and S. S. Ying, "Reduced-order compensation using the hyland-bernstein optimal projection equations," *Journal of guidance, control, and dynamics*, vol. 19, no. 2, pp. 407–417, 1996.

[52] M. Dardel and F. Bakhtiari-Nejad, "Limit cycle oscillation control of wing with static output feedback control method," *Aerospace Science and Technology*, vol. 24, no. 1, pp. 147–160, 2013.

[53] W. Levine and M. Athans, "On the determination of the optimal constant output feedback gains for linear multivariable systems," *IEEE Transactions on Automatic control*, vol. 15, no. 1, pp. 44–48, 1970.

[54] D. Moerder and A. Calise, "Convergence of a numerical algorithm for calculating optimal output feedback gains," *IEEE Transactions on Automatic Control*, vol. 30, no. 9, pp. 900–903, 1985.

[55] F. Fonte, "Active gust alleviation for a regional aircraft through static output feedback," 2013.

[56] F. Fonte, S. Ricci, and P. Mantegazza, "Gust load alleviation for a regional aircraft through a static output feedback," *Journal of Aircraft*, vol. 52, no. 5, pp. 1559–1574, 2015.

[57] E. Union, "Clean sky 2." `https://www.cleansky.eu/`.

[58] F. Fonte, F. Toffol, and S. Ricci, "Design of a wing tip device for active maneuver and gust load alleviation," in *2018 AIAA/ASCE/AHS/ASC Structures, Structural Dynamics, and Materials Conference*, p. 1442, 2018.

[59] E. Vartio, A. Shimko, C. Tilmann, and P. Flick, "Structural modal control and gust load alleviation for a sensorcraft concept," in *46th AIAA/ASME/ASCE/AHS/ASC Structures, Structural Dynamics and Materials Conference*, p. 1946, 2005.

[60] R. T. Whitcomb, "A design approach and selected wind tunnel results at high subsonic speeds for wing-tip mounted winglets," 1976.

[61] S. A. Ning and I. Kroo, "Multidisciplinary considerations in the design of wings and wing tip devices," *Journal of aircraft*, vol. 47, no. 2, pp. 534–543, 2010.

[62] S. Ricci, M. Castellani, and G. Romanelli, "Multi-fidelity design of aeroelastic wing tip devices," *Proceedings of the Institution of Mechanical Engineers, Part G: Journal of Aerospace Engineering*, vol. 227, no. 10, pp. 1596–1607, 2013.

[63] A. Castrichini, V. Hodigere Siddaramaiah, D. Calderon, J. E. Cooper, T. Wilson, and Y. Lemmens, "Nonlinear folding wing tips for gust loads alleviation," *Journal of Aircraft*, vol. 53, no. 5, pp. 1391–1399, 2016.

[64] A. Castrichini, J. E. Cooper, T. Wilson, A. Carrella, and Y. Lemmens, "Nonlinear negative stiffness wingtip spring device for gust loads alleviation," *Journal of Aircraft*, vol. 54, no. 2, pp. 627–641, 2017.

[65] R. C. Cheung, A. Castrichini, D. Rezgui, J. E. Cooper, and T. Wilson, "Testing of wing-tip spring device for gust loads alleviation," in *58th AIAA/ASCE/AHS/ASC Structures, Structural Dynamics, and Materials Conference*, p. 0630, 2017.

[66] S. Vasista, J. Riemenschneider, B. Van De Kamp, H. P. Monner, R. C. Cheung, C. Wales, and J. E. Cooper, "Evaluation of a compliant droop-nose morphing wing tip via experimental tests," *Journal of Aircraft*, vol. 54, no. 2, pp. 519–534, 2017.

[67] A. Wildschek, "Concurrent optimization of a feed-forward gust loads controller and minimization of wing box structural mass on an aircraft with active winglets," in *16th AIAA/ISSMO Multidisciplinary Analysis and Optimization Conference*, p. 2490, 2015.

[68] M. Habib, R. B. Mansour, and M. Nemit-allah, "Modeling of oxygen permeation through a lscf ion transport membrane," *Computers & Fluids*, vol. 76, pp. 1–10, 2013.

[69] M. Nemitallah, M. Habib, and R. B. Mansour, "Investigations of oxy-fuel combustion and oxygen permeation in an itm reactor using a two-step oxy-combustion reaction kinetics model," *Journal of membrane science*, vol. 432, pp. 1–12, 2013.

[70] K.-U. Hahn and C. Schwarz, "Alleviation of atmospheric flow disturbance effects on aircraft response," in *26th Congress of the International Council of the Aeronautical Sciences*, 2008.

[71] Y. MATSUZAKI, T. UEDA, T. MIYAZAWA, and H. MATSUSHITA, "Wind tunnel test and analysis on gust load alleviation of a transport-type wing," in *28th Structures, Structural Dynamics and Materials Conference*, p. 781, 1987.

[72] S. I. Kuzmina, F. Ishmuratov, M. Zichenkov, and V. Chedrik, "Integrated numerical and experimental investigations of the active/passive aeroelastic concepts on the european research aeroelastic model (euram)," *Journal of Aeroelasticity and Structural Dynamics*, vol. 2, no. 2, 2011.

[73] M. Karpel, B. Moulin, V. Feldgun, L. Anguita, F. Rosich, and H. Climent, "Active alleviation of gust loads using special control surfaces," in *47th AIAA/ASME/ASCE/AHS/ASC Structures, Structural Dynamics, and Materials Conference 14th AIAA/ASME/AHS Adaptive Structures Conference 7th*, p. 1833, 2006.

[74] B. Moulin and M. Karpel, "Gust loads alleviation using special control surfaces," *Journal of Aircraft*, vol. 44, no. 1, pp. 17–25, 2007.

[75] Z. Wu, L. Chen, and C. Yang, "Study on gust alleviation control and wind tunnel test," *Science China Technological Sciences*, vol. 56, no. 3, pp. 762–771, 2013.

[76] O. Sensburg, J. Becker, H. Lusebrink, and F. Weiss, "Gust load alleviation on airbus a300," in *ICAS Conference, Seattle*, 1982.

[77] C. Heinen, A. Wildschek, and M. Herring, "Design of a winglet control device for active load alleviation," in *Proceedings of the 2013 International Forum on Aeroelasticity and Structural Dynamics*, 2013.

[78] P. Burris and M. Bender, "Aircraft load alleviation and mode stabilization (lams): B-52 system analysis, synthesis, and design," tech. rep., BOEING WICHITA CO KS, 1969.

[79] F. Toffol, F. Fonte, and S. Ricci, "Design of an innovative wing tip device," in *17th International Forum on Aeroelasticity and Structural Dynamics (IFASD 2017)*, pp. 1–16, 2017.

[80] S. Ricci et. al., "Design and wind tunnel test validation of gust load alleviation systems," in *58th AIAA/ASCE/AHS/ASC Structures, Structural Dynamics, and Materials Conference*, p. 1818, 2017.

[81] F. Fonte, A. De Gaspari, L. Riccobene, F. Toffol, S. Malik, L. Marchetti, S. Ricci, P. Mantegazza, and E. Livne, "Numerical and experimental investigations on active flutter suppression technologies," in *18th International Forum on Aeroelasticity and Structural Dynamics (IFASD 2019)*, pp. 1–10, International Forum on Aeroelasticity and Structural Dynamics (IFASD), 2019.

[82] L. Marchetti, A. De Gaspari, L. Riccobene, F. Toffol, F. Fonte, S. Ricci, P. Mantegazza, E. Livne, and K. A. Hinson, "Active flutter suppression analysis and wind tunnel studies of a commercial transport configuration," in *AIAA Scitech 2020 Forum*, p. 1677, 2020.

[83] S. Ricci, F. Fonte, A. De Gaspari, L. Riccobene, P. Mantegazza, F. Toffol, and E. Livne, "Development of a wind tunnel model for active flutter suppression studies," in *AIAA Scitech 2019 Forum*, p. 2029, 2019.

[84] A. De Gaspari, S. Ricci, L. Riccobene, and A. Scotti, "Active aeroelastic control over a multi-surface wing: Modeling and wind-tunnel testing," *AIAA journal*, vol. 47, no. 9, pp. 1995–2010, 2009.

[85] S. Ricci and A. Scotti, "Wind tunnel testing of an active controlled wing under gust excitation," in *49th AIAA/ASME/ASCE/AHS/ASC Structures, Structural Dynamics, and Materials Conference, 16th AIAA/ASME/AHS Adaptive Structures Conference, 10th AIAA Non-Deterministic Approaches Conference, 9th AIAA Gossamer Spacecraft Forum, 4th AIAA Multidisciplinary Design Optimization Specialists Conference*, p. 1727, 2008.

[86] L. Cavagna, S. Ricci, and A. Scotti, "Active aeroelastic control over a four control surface wing model," *Aerospace Science and Technology*, vol. 13, no. 7, pp. 374–382, 2009.

[87] S. Ricci, A. Scotti, J. Cecrdle, and J. Malecek, "Active control of three-surface aeroelastic model," *Journal of aircraft*, vol. 45, no. 3, pp. 1002–1013, 2008.

[88] R. Knight and J. Wykes, "Progress report on a gust alleviation and structural dynamic stability augmentation system (gasdsas) design study," in *3rd Annual Meeting*, p. 999, 1966.

[89] J. WYKES and A. MORI, "Techniques and results of an analytical investigation into controlling the structural modes of flexible aircraft," in *Symposium on Structural Dynamics and Aeroelasticity*, p. 1140, 1965.

[90] J. Wykes, "Structural dynamic stability augmentation and gust alleviation of flexible aircraft," in *5th Annual Meeting and Technical Display*, p. 1067, 1968.

[91] J. H. Wykes, M. Kelpl, and M. J. Brosnan, "Flight test and analyses of the b-1 structural mode control system at supersonic flight conditions," 1983.

[92] T. P. Krauss, L. Shure, and J. Little, *Signal processing toolbox for use with MATLAB®: user's guide*. The MathWorks, 1994.

[93] J. Nocedal and S. Wright, *Numerical optimization*. Springer Science & Business Media, 2006.

[94] B. Grossman, Z. Gurdal, G. Strauch, W. Eppard, and R. T. Haftka, "Integrated aerodynamic/structural design of a sailplane wing," *Journal of Aircraft*, vol. 25, no. 9, pp. 855–860, 1988.

[95] G. Bindolino, M. Lanz, P. Mantegazza, and S. Ricci, "Integrated structural optimization in the preliminary aircraft design," in *Proceedings of the 17th Congress of the International Council of the Aeronautical Sciences, Stockholm, Sweden*, pp. 1366–1378, 1990.

[96] E. Livne, L. Schmit, and P. Friedmann, "Integrated structure/control/aerodynamic synthesis of actively controlled composite wings," *Journal of Aircraft*, vol. 30, no. 3, pp. 387–394, 1993.

[97] A. Chattopadhyay and N. Pagaldipti, "A multidisciplinary optimization using semi-analytical sensitivity analysis procedure and multilevel decomposition," *Computers & Mathematics with Applications*, vol. 29, no. 7, pp. 55–66, 1995.

[98] M. Baker and J. Giesing, "A practical approach to mdo and its application to an hsct aircraft (multidisciplinary design optimization)," in *Aircraft Engineering, Technology, and Operations Congress*, p. 3885, 1995.

[99] J. Sobieszczanski-Sobieski and R. T. Haftka, "Multidisciplinary aerospace design optimization: survey of recent developments," *Structural optimization*, vol. 14, no. 1, pp. 1–23, 1997.

[100] J. S. Gray, J. T. Hwang, J. R. R. A. Martins, K. T. Moore, and B. A. Naylor, "OpenMDAO: An open-source framework for multidisciplinary design, analysis, and optimization," *Structural and Multidisciplinary Optimization*, vol. 59, pp. 1075–1104, April 2019.

[101] T. R. Brooks, J. R. R. A. Martins, and G. J. Kennedy, "High-fidelity aerostructural optimization of tow-steered composite wings," *Journal of Fluids and Structures*, vol. 88, pp. 122–147, July 2019.

[102] M. Lab, *University of Michigan*.

[103] S. Binder, A. Wildschek, and R. De Breuker, "The interaction between active aeroelastic control and structural tailoring in aeroservoelastic wing design," *Aerospace Science and Technology*, vol. 110, p. 106516, 2021.

[104] T. Mathworks, "Matlab optimization toolbox user's guide," *Math Work*, 2007.

[105] C. Easa, "Certification specifications for large aeroplanes, cs 25," 2009.

[106] P. M. Weaver and M. P. Nemeth, "Bounds on flexural properties and buckling response for symmetrically laminated composite plates," *Journal of engineering mechanics*, vol. 133, no. 11, pp. 1178–1191, 2007.

[107] J. E. Herencia, P. M. Weaver, and M. I. Friswell, "Optimization of long anisotropic laminated fiber composite panels with t-shaped stiffeners," *AIAA journal*, vol. 45, no. 10, pp. 2497–2509, 2007.

[108] T. Melin, "User's guide tornado 1.0 release 2.3 2001-01-31," *KTH report-, Royal Institute of Technology (KTH)*, 2003.

[109] E. Albano and W. P. Rodden, "A doublet-lattice method for calculating lift distributions on oscillating surfaces in subsonic flows.," *AIAA journal*, vol. 7, no. 2, pp. 279–285, 1969.

[110] M. Blair, "A compilation of the mathematics leading to the doublet lattice method," tech. rep., WRIGHT LAB WRIGHT-PATTERSON AFB OH, 1992.

[111] L. Cavagna, "A multi–fidelity approach to computational aeroelasticity for fixed wing aircraft," 2009.

[112] "A330-300 triptych from web." https://airbusa330300swissair.blogspot.com/2020/04/airbus-a330-300-technical-specifications.html.

[113] G. Bindolino, P. Mantegazza, and L. Visintini, "A comparison of panel methods for potential flow calculations," in *VIII Congresso Nazionale AIDAA*, pp. 23–27, 1985.

[114] D. Calderon, J. Cooper, M. Lowenberg, S. Neild, and E. Coetzee, "Sizing high-aspect-ratio wings with a geometrically nonlinear beam model," *Journal of Aircraft*, vol. 56, no. 4, pp. 1455–1470, 2019.

[115] U. E. P. Agency, "Emission factors for greenhouse gas inventories." https://www.epa.gov/sites/production/files/2015-07/documents/emission-factors_2014.pdf, 2014.

[116] Enipower, "Bilancio di sostenibilitÃ ," tech. rep., 2019.

[117] E. Barbiroglio, "There Are Now Nine Countries Asking For An EU Aviation Carbon Tax." https://www.forbes.com/sites/emanuelabarbiroglio, 11 2019.

[118] U. M. H. MIL-HDBK, "Flying qualities of piloted aircraf, 1997," 1797.

[119] S. Gage, "Creating a unified graphical wind turbulence model from multiple specifications," in *AIAA Modeling and simulation technologies conference and exhibit*, p. 5529, 2003.

[120] M. Gabanelli and F. Tortora, "Viaggi in aereo: perché il riscaldamento globale li rende piú pericolosi." https://www.corriere.it/dataroom-milena-gabanelli/, 3 2021.

[121] P. D. Williams, "Increased light, moderate, and severe clear-air turbulence in response to climate change," *Advances in Atmospheric Sciences*, vol. 34, no. 5, pp. 576–586, 2017.

[122] S. H. Lee, P. D. Williams, and T. H. Frame, "Increased shear in the north atlantic upper-level jet stream over the past four decades," *Nature*, vol. 572, no. 7771, pp. 639–642, 2019.

[123] "Turbulence: Staying Safe." https://www.faa.gov/travelers/fly_safe/turbulence/, 8 2017.

[124] "Fact Sheet - Turbulence." https://www.faa.gov/news/fact_sheets/news_story.cfm?newsId=20074, 2 2020.